Dissertation zur Erlangung des Doktorgrades

an der Fakultät für Chemie und Pharmazie

der Ludwig-Maximilians-Universität München

Neocarzilins – natural compounds with diverse molecular targets and biological effects

Adrian Tibor Jauch

aus Scherzingen, Schweiz

2023

Erklärung

Diese Dissertation wurde im Sinne von §7 der Promotionsordnung vom 28. November 2011 von Frau Prof. Dr. Angelika M. Vollmar betreut.

Eidesstattliche Versicherung

Diese Dissertation wurde eigenständig und ohne fremde Hilfe erarbeitet.

München, den 18.11.2023 _____

Adrian Tibor Jauch

Dissertation eingereicht am: 21.11.2023

1. Gutachter: Professorin Dr. Angelika M. Vollmar

2. Gutachter: Professor Dr. Stefan Zahler

Mündliche Prüfung am: 21.12.2023

To my family

Contents

Contents

ABSTRACT

1 Abstract

Natural products have always been a valuable source of bioactive molecules, which have proven to be both chemical tools for the discovery and elucidation of new signaling pathways and therapeutically addressable targets, as well as lead substances for the development of novel therapeutics. However, contrary to the one drug one target paradigm that has long prevailed, so-called multi-target drugs (also known as network therapeutics) have attracted special attention in recent years. They are of particular interest for the treatment of complex diseases or those with pronounced drug-resistance issues with cancer being a prime example in both cases.

Here, we focused on the natural compound class of neocarzilins, a family of short chlorinated polyenones isolated from a *Streptomyces carzinostaticus*. Particular attention was paid to neocarzilin A (NCA), which is the most potent structure among the naturally occurring representatives. In previous work, it has been shown that this class causes both a strong inhibition of cell proliferation and an impressive reduction in cell motility [1]. By using a combined proteomics and cell biology approach, synaptic vesicle membrane protein (VAT-1), the target responsible for the antimigratory effect was recently identified. In the first part of this study, we elucidated the cellular localization of the protein and generated a knockout model in a cancer cell line by using the CRISPR/Cas9 technology for further loss-of-function studies. An initial characterization of the clones showed that VAT-1 depletion neither led to a general reduction in cell proliferation nor to a lower responsiveness to NCA in terms of antiproliferative activity, confirming the assumption that there must be an additional target to explain this phenotype. In contrast to this, the knockout resulted in a significant reduction of the antimigratory effect of the compound, underpinning the hypothesis that this is mediated by VAT-1. Furthermore, we demonstrated that VAT-1 is indispensable for proper cell spreading and the maturation of focal adhesions, which are essential for functional adhesion and migration. A reduction of integrin β1 activation, however, could not be solely attributed to loss of our protein of interest.

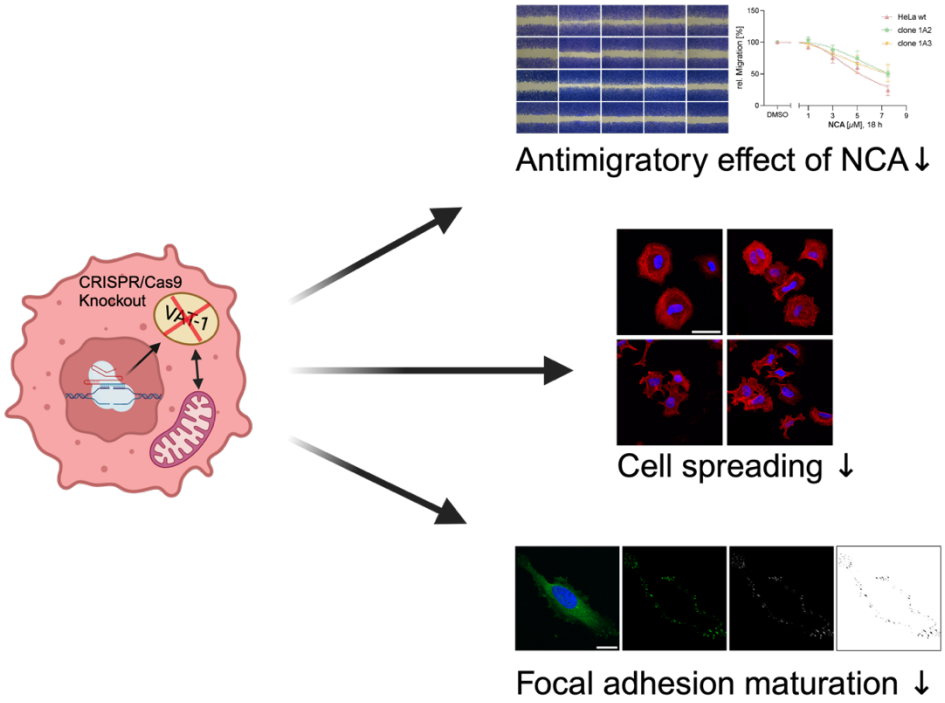

Figure 1 VAT-1 is important for proper cell spreading and focal adhesion dynamics and influences thereby cancer cell migration – the project at a glance.
Created with BioRender.com

In the second part, based on unpublished preliminary data, we focused on the influence of NCA on mitochondrial functions. By this, we were able to show that NCA unbalances mitochondrial network dynamics through increased optic atrohpy protein 1 (Opa1) splicing and changes the ultrastructure of these organelles. We also demonstrated that the compound dissipates the mitochondrial membrane potential and triggers mitochondrial superoxide generation by calcium overload. Moreover, we uncovered an intensive disruption of the electron transfer chain with diminished activity of complexes of the respiratory chain in a cooperation with the group of Prof. Dr. Hans Zischka (Helmholtz Munich, Germany). This perturbation resulted in an impairment of ATP synthesis. In the further course of the investigations, a strong induction of the extrinsic pathway of apoptosis upon NCA treatment was revealed. The discovery that the natural compound triggers a strong cytoplasmic vacuolization led to the completely new insight that NCA also causes endoplasmic reticulum stress and thereby activates the unfolded protein response. By applying activity-based protein profiling (ABPP) in cooperation with the group of Prof. Dr. Stephan Sieber (TU Munich, Germany), we identified reticulon 4 (Rtn4) as promising

novel target responsible for this phenotype, which was confirmed it by immunofluorescence stainings, molecular docking and knockdown studies.

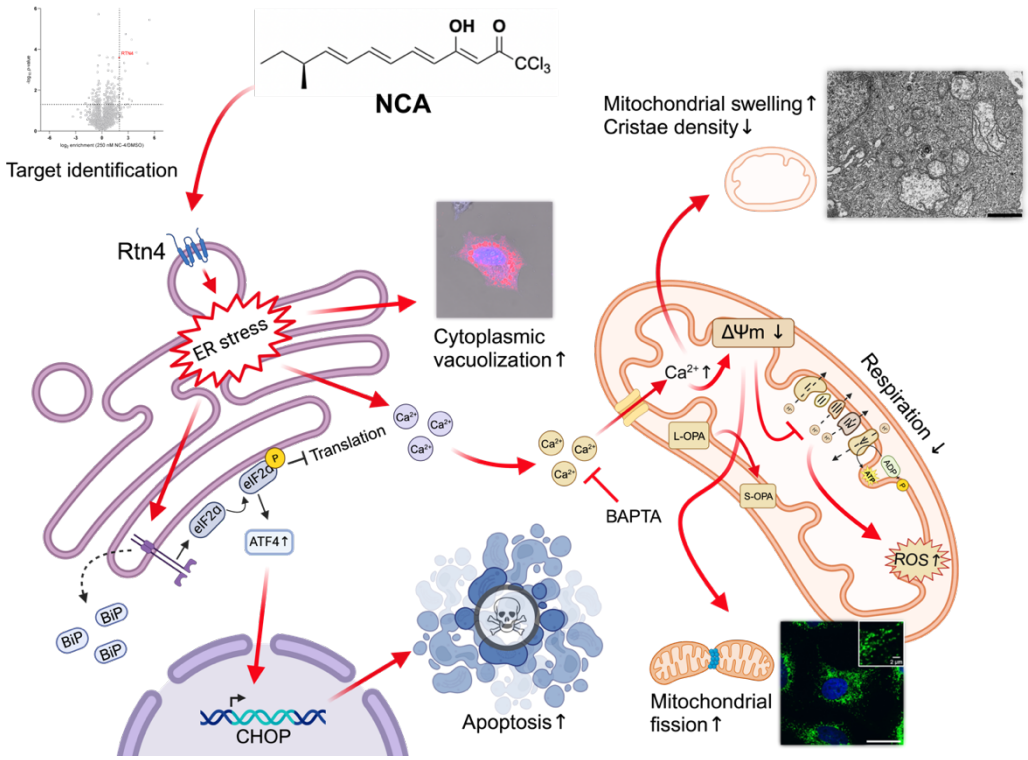

Figure 2 The effects of neocarzilin A on mitochondrial functions – the project at a glance.
Created with BioRender.com

In the final section of this thesis, we characterized a series of neocarzilin derivatives with regard to their antiproliferative and antimigratory potency, thereby gaining deeper insights into structure-activity relations of this interesting natural compound family. Derivative WHY-308 exhibited a lower IC_{50} for the antiproliferative effect than the lead structure NCA. NC-4 the improved neocarzilin target probe with a higher structural similarity to the original compound compared to its predecessor NC-1, showed a similarly high potency as NCA in both respects.

To sum it up, this work could shed more light on the mechanism by which VAT-1 influences cell migration. Additionally, a new phenotype triggered by neocarzilin A was in depth investigated and the responsible target identified. And finally, we revealed insights into structure-activity relationships of the neocarzilins by biological testing of a variety of synthesized derivatives.

INTRODUCTION

2 Introduction

2.1 Natural compounds

As privileged structures, natural substances still represent an extremely important source of new therapeutics, evidenced by the fact that 48% of all antitumor drugs approved by the FDA since 1946 are either biological macromolecules, natural products, botanical drugs or at least derivatives of natural products [2]. Despite technical challenges in isolation, characterization, and structural optimization, they are of indispensable importance for the discovery of innovative drug targets. In the recent years, interest in natural products as drug leads has increased again due to novel technologies that help to overcome the aforementioned difficulties [3]. Streptomycetes are a particularly rich repository of novel structures, especially in the field of anti-infectives. Many antibiotics still in use today, such as streptomycin, clindamycin and fosfomycin, as well as anti-cancer drugs like bleomycin, were originally isolated from streptomycetes [4].

2.2 Multi-target drugs

For a long time, the conventional wisdom was that when developing new drugs, their specificity for their target combined with high potency was of utmost importance according to the paradigm of one drug one target. In the recent decades, multi-target drugs that do not meet this definition have attracted attention as they offer new possibilities for the treatment of complex disease and those with pronounced resistance problems like cancer [5]. And in any case, some long-used therapeutics agents can be attributed to the so-called polypharmacology, i.e. the simultaneous addressing of several targets and a trend in this direction has been observed [6].

2.3 Neocarzilins

The natural compounds neocarzilin A (NCA) and B (NCB), short chlorinated polyenones, were isolated in the early 1990s from the mycelium of the streptomyces strain *Streptomyces carzinostaticus* by Nozoe *et al.* NCA exhibited a high cytotoxic activity against the leukemia cell line K562 [7]. During studies on the biosynthesis of those interesting bioactive molecules through a polyketide synthase, a third naturally occurring representative, neocarzilin C (NCC) was discovered [8]. Several years later, Gleissner *et*

al. started to investigate the neocarzilins in more detail and demonstrated that in addition to a strong inhibition of cell proliferation in a panel of cancer cell lines, cell migration was also severely impaired. Furthermore, NCA was found to be the most active member of the family in terms of both antiproliferative and antimigratory effects [1].

2.4 Cell adhesion and motility

Cell adhesion and migration are crucial processes in development, wound healing, but also implicated in pathological conditions like inflammation and cancer. The latter is evident from the fact that they are important features of the cancer hallmarks neoangiogenesis and metastasis [9]. Cell migration is a sequential process, comprising (1) polarization of the cell and lamellipodia protrusion, (2) attachment of the leading edge through adhesive receptors, (3) myosin contraction and retraction of the rear part of the cell in order to move forward. Targeting cell motility represents a promising strategy, especially to counter invasion and metastasis [10].

2.4.1 Cell spreading

Although they share components like deformation of the plasma membrane and attachment to a surface, cell migration and spreading are distinctly different processes. Migration is purely active and spreading, especially in the beginning, a rather passive event [11], followed by adhesion to the surfaces, flattening [12] and deforming through actin polymerization [13]. Though it is rather an artificial process, spreading can be a good model to study motility and adhesion properties of cells.

2.4.2 Integrins, talin & focal adhesions

Focal adhesions (FA) are highly dynamic structures composed of various proteins like talin, vinculin, paxillin and focal adhesion kinase with integrins at their core. They mechanically link cells to the extracellular matrix (ECM) to transmit forces and exchange signals between the environment and the cell [14]. During the migration process they mature which is accompanied by an increase in size, elongation and changes in protein composition. In order to allow the cell to move forward, FAs in the rear part have to disassemble, which is reported to be facilitated by KN motif and ankyrin repeat domains 2 (Kank2) [15]. Integrins are transmembrane adhesion receptors and connect as one of the

main components of the FAs the cytoskeleton to the ECM. They form heterodimers of an α- and β-subunit, which gives 24 combinations in mammals. The exist in two states with different affinities for the ECM ligands. A bend low affinity and stretched, activated conformation with high affinity. Binding depends on divalent cations, clustering and activation is facilitated by talin (inside-out signaling). Talin is an adaptor protein, consisting of a head and rod domain, featuring three binding sites for the cytoplasmic domain of β-integrin subunits and several actin binding sites. By this linkage, signals from the environment can also be transmitted to the cell (outside-in signaling) [16].

2.5 VAT-1

The synaptic vesicle membrane protein 1 (VAT-1) was first isolated and described by Linial *et al*. in 1989 from the electric lobe of *Torpedo californica*, an electric ray that is frequently used as model organism for studies on neurophysiology. It was reported as a 42 kDa integral membrane protein found in synaptic vesicles and suspected to be involved in transmitter trafficking [17]. In the following years, bioinformatic analysis revealed a high structural similarity to guinea pig lens protein ζ-crystallina and nucleotide binding properties [18] and led to its classification as member of the medium-chain alcohol dehydrogenases [19]. Gradually, further characteristics were postulated, such as the presence of high-mass protein complexes consisting of VAT-1 subunits and an ATPase activity dependent on divalent cations. In 1998, Hayess *et al*. discovered the mammalian homologue of VAT-1 isolated from a murine breast cancer cell line, where a slightly higher molecular weight of 48 kDa was observed [20]. The protein has been linked to various tumor entities, such as hepatocellular carcinoma (HCC), gastric cancer and glioblastoma, where it was reported to be overexpressed and served as prognostic marker correlating with a poor prognosis, which suggested its suitability as therapeutic target [21-24]. Interestingly, an involvement of VAT-1 in cell migration has been identified in the context of glioblastoma, with the upregulation of the protein increasing invasiveness [23]. But VAT-1 also appears to play a role in other pathophysiologies, since it was demonstrated to be a pathogenic factor in benign prostatic hyperplasia connected to cell proliferation [25]. For a long time, not much was known about the cell-physiological function of the protein in mammals. It was then reported to be interact with mitofusin 1 (Mfn1), the master regulator of mitochondrial outer membrane fusion, and postulated to play a role in phospholipid trafficking from the endoplasmic reticulum to mitochondria [26, 27]. In 2019 coworkers of

us demonstrated that VAT-1 is one of the molecular targets of NCA mediating its antimigratory phenotype by influencing its interaction with talin1 (TLN1) [1]. Shortly afterwards, the structure of the protein was determined using X-ray crystallography revealing a homodimer organization, a nucleotide binding pocket and confirming the enzymatic activity shown against several quinone structures [28, 29].

2.6 Mitochondria in the context of cancer

Mitochondria are organelles surrounded by double membrane which, according to the endosymbiont hypothesis, were formed by the engulfment of a prokaryote [30]. This explains why they possess their own genomic material and can only be reproduced by dividing. Due to their immensely important function in restoring the ATP pool of cells by the oxidative phosphorylation (OXPHOS), the generation of reactive oxygen species, buffering of Ca^{2+}, maintaining redox homeostasis, in the fatty acid metabolism and providing building blocks, disturbance of proper functionality leads to severe pathological conditions such as Parkinson's or Alzheimer's disease or can drive cancer progression [31]. They are of highly dynamic nature, being constantly repositioned, undergoing fission and fusion to form higher networks, control their number and size, and adapt to the energy demand of the cell, which is also referred to as mitochondrial dynamics [32]. Given these indispensable catabolic and anabolic functions, mitochondrial alteration displays a hallmark of tumorigenesis [33]. Interestingly, despite their high energy requirements, a large proportion of cancer cells use glycolysis rather than the much more efficient OXPHOS to synthesize ATP, even in the presence of oxygen. This phenomenon was discovered by Otto Warburg and named after him as the Warburg effect and helps tumor cells surviving under varying oxygen supply [34]. Targeting mitochondria in cancer therapies remains challenging, as most of those approaches lack specificity and therefore carry side effects. One strategy here is to manipulate mitochondrial metabolism, since reprogramming of energy metabolism was identified as an emerging hallmark of cancer [35]. A combination treatment of cisplatin and glycolysis inhibition by 2-deoxyglucose has been tested in clinical trials and shown to increase cytotoxicity by enhancing metabolic oxidative stress in cancer cells [36]. Other approaches include the induction of the mitochondrial permeability transition pore (mPTP) or ROS overproduction [37, 38]. Several mitochondria addressing agents are derived from natural products, for example

betulinic acid, which triggers the mitochondrial outer membrane permeabilization (MOMP) to release pro-apoptotic proteins or resveratrol a polyphenolic bioactive molecule from grapes that affects the OXPHOS and mitochondrial biogenesis by modulating the activity of the peroxisome proliferator-activated receptor-γ co-activator (PGC1α) [39]. A more innovative concept, however, is to induce an immune response against mutated mitochondrial proteins [40].

2.6.1 Apoptosis

Since one of the long recognized hallmarks of cancer is evading programmed cell death, apoptosis represents an important starting point for the development of new anti-cancer drugs [9]. Cell death can classically be executed via two pathways, the intrinsic and extrinsic, both of which rely on mitochondria as platform. The intrinsic pathway involves the permeabilization of mitochondrial membrane by Bcl-2 protein Bcl-2 associated X (Bax) and Bcl-2 antagonist/killer (Bak), which leads to the release of cytochrome c. This in turn forms the apoptosome with procaspase 9 and apoptotic peptidase activating factor 1 (Apaf-1) and finally activates downstream caspases that execute apoptosis. The extrinsic pathway, on the other hand, is initially activated by transmembrane receptors of the tumor necrosis factor receptor family bearing a cytoplasmic death domain [41]. Ligand binding induces caspase 8 activation that can directly activate executer caspases [42] or cleave the proapoptotic protein Bid which gets translocated to mitochondria and induces the release of proapoptotic factors, thereby linking the two pathways [43].

2.7 The endoplasmic reticulum, stress response and therapeutic options

Another highly dynamic organelle that is in close contact with mitochondria is the endoplasmic reticulum (ER). It gets constantly remodeled to maintain its network throughout the cell and as continuum of the nuclear envelope considered the largest organelle of cells [44]. Its main tasks include protein synthesis, transport as well as proper folding, steroid and lipid synthesis, modification of carbohydrates and storage of calcium ions [45]. Morphologically, it can be divided into rough, ribosome spiked sheets where protein synthesis takes place and smooth tubular regions. Several proteins are involved in keeping the ER in shape, of which the reticulons are the best known and are discussed in

more detail below [46]. The ER is a highly dynamic organelle, constantly remodeling to maintain its network throughout the cell [44]. A variety of stressors like nutrient deprivation, viral infection, exposure to cytotoxic agents and oxidative stress lead to the accumulation of misfolded proteins and trigger, thereby, endoplasmic reticulum stress [47]. To rebalance this condition and restore proper protein folding capacity, the unfolded protein response (UPR) is activated. This can be accomplished by three branches, the PKR-like ER kinase (PERK), inositol requiring 1 (IRE1) and activating transcription factor 6 (ATF6) pathway, all of which start with the dissociation of the ER chaperon immunoglobulin binding protein (BiP) triggered by the accumulation of unfolded proteins. The exact sequence of all branches is depicted in **Figure 3**. As a result, the expression of chaperons, protein processing enzymes and the ER-associated protein degradation (ERAD) program, as well as autophagy, is upregulated to remove the accumulated proteins [48]. If this counter-regulation fails or under prolonged stress conditions, cell death is induced. One example of how this can be facilitated is, that the activation of the PERK pathway leads to elevated activating transcription factor 4 (ATF4) translation through eukaryotic initiation factor 2α (eIF2α) phosphorylation, which in turn induces gene expression of the proapoptotic factor C/EBP homologous protein (CHOP) that finally modulates death receptor 5 (DR5) and promotes the extrinsic apoptosis pathway [49]. Persisting ER has been demonstrated to be a crucial driver of cancer progression and in some cases, responsible for chemoresistance, but also offers the opportunity to intervene therapeutically [50].

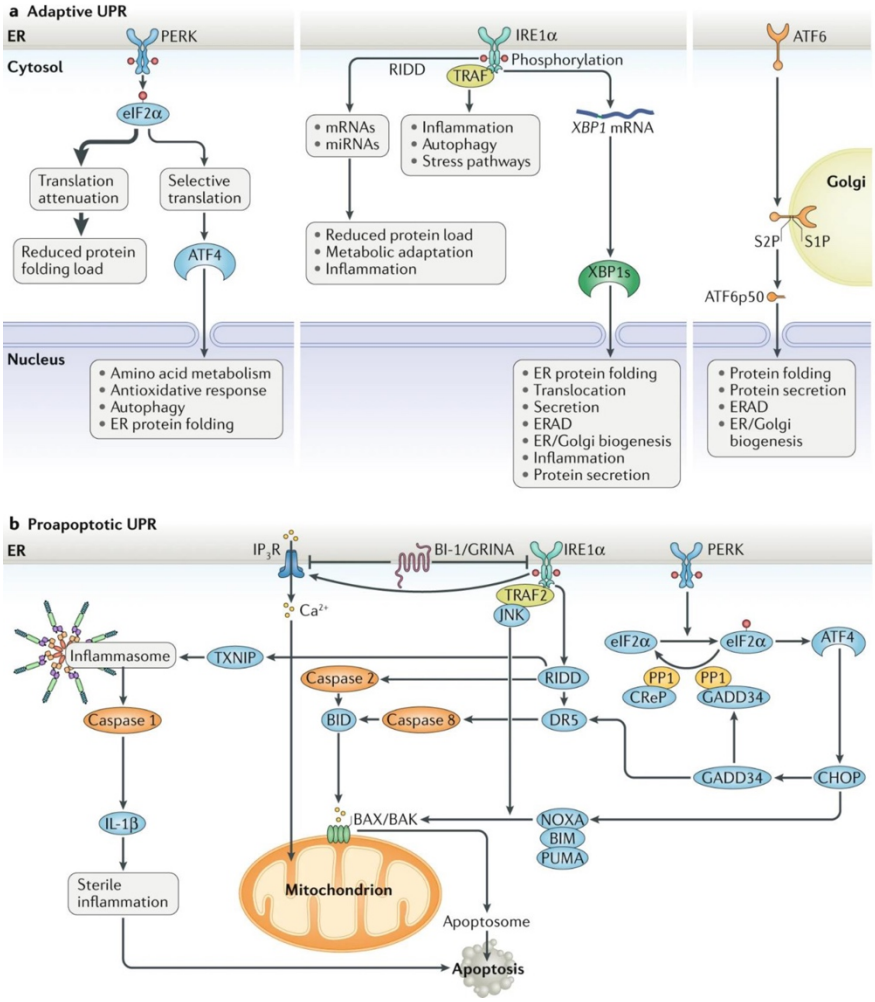

Figure 3 The major UPR pathways initiated in the ER.
a) Adaptive unfolded protein response (UPR), under ER stress three canonical UPR branches are activated: PERK, IRE1α and ATF6 pathway.
b) Proapoptotic UPR, PERK branch induced ATF4 triggers CHOP transcription and modulates DR5, followed by caspase 8 activation, Bid cleavage, cytochrome c release resulting in apoptosis. Adapted from Hetz *et al. [51]*

2.7.1 Reticulons

In mammals, the reticulons are a family comprising four proteins Rtn1, 2, 3 and Rtn4/Nogo that have multiple isoforms generated by alternative splicing. Common to all is the highly conserved C-terminal reticulon homology domain (RHD, consisting of two hydrophobic, membrane-spanning regions separated by a 66 aa long hydrophilic sequence that protrudes into the endoplasmic reticulum (ER lumen, cytoplasm, or extracellular space, respectively. Rtn1, Rtn3 and Rtn4/Nogo show the highest sequence identity in this region (average 73%). In contrast, the N-terminal region shows little to no sequence similarity [52] (**Figure 4).** Their main function is to shape the ER, or more precisely the tubular

proportion of it, by stabilizing high curvature membranes through their hairpin topology in ER membranes [53]. But they are also involved in maintaining calcium homeostasis, in membrane trafficking between the golgi apparatus and the ER and have tightly been connected to apoptosis regulation, accomplished by binding and recruiting anti-apoptotic Bcl-2 proteins from the ER to mitochondria [54-56]. However, there were different findings in this regard. Rtn4/Nogo and Rtn1 were found to have pro-apoptotic and Rtn3 rather anti-apoptotic properties. ER stress appears to have an influence on reticulon expression, in that they increase during stress conditions. There was particular interest in the research of Rtn4, also called neurite outgrowth inhibitor (Nogo), in the context of central nervous system lesions [57, 58]. The protein was shown to be localized in the plasma membrane of oligodendrocytes, with the 66 aa hydrophilic loop (nogo66) protruding into the extracellular space [59]. By binding the Rtn4 receptor NogoR the regeneration of CNS axons gets inhibited through interaction with co-receptors like leucine rich repeat and Ig domain containing 1 (LINGO-1) [60, 61]. It is therefore not surprising that an anti-Nogo antibody for the treatment in acute spinal cord injury has already been successfully been tested in a phase II clinical trial (**N**ogo-A **I**nhibition in acute **S**pinal **C**ord **I**njury – NISCI) [62].

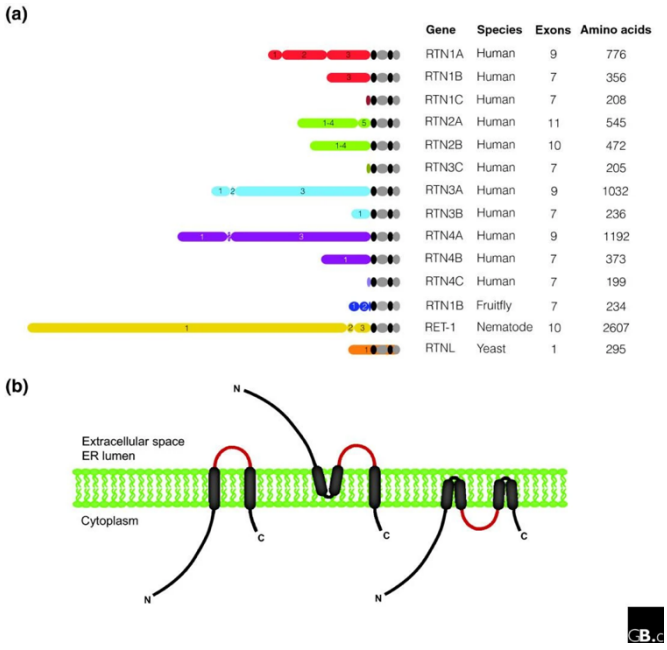

Figure 4 Overview of reticulon protein family members, isoforms, and membrane topology.
a) Mammalian reticulon family comprises 4 proteins with several isoforms generated by alternative splicing. Additionally depicted fruit fly (Rtn1B, nematode (RET-1 and yeast (RtnL reticulons. Number of exons and aa sequence length are listed. Highly conserved C-terminal reticulon homology domain (RHD is presented as two black membrane spanning hydrophobic regions linked by a grey hydrophilic loop (nogo66). **b)** Detected topologies of the RHD in the endoplasmic reticulum membrane or plasma membrane. Adapted from Yang *et al.* [63]

2.8 Aims of the study

The natural compound neocarzilin A (NCA) was shown to exhibit striking anti-proliferative and -migratory activity in various cancer cell lines [1, 7]. For the anti-migratory phenotype, Gleisner *et al.* [1] identified VAT-1 as responsible molecular target, but in-depth studies on the mode of action are still lacking.

On the contrary, the anti-proliferative effect of NCA is still poorly understood. To solve this issue, an improved version of the neocarzilin target probe to identify additional targets was synthesized and characterized in these studies.

Furthermore, preliminary data suggested a strong perturbation of mitochondrial functions upon NCA treatment. In this thesis, we want to investigate this phenotype in more detail and identify the target responsible for it.

Besides their eligibility as chemical tools, the neocarzilins could also serve as anticancer drug leads, especially since they address several targets at the same time. This characteristic is also referred to as multimodal drug and of particular interest for the treatment of diseases with resistance problems like cancer. To further improve activity and find chemical moieties determining the different biological phenotypes, we aimed to examine a variety of neocarzilin derivatives in terms of anti-proliferative and -migratory effects and analyze structure-activity relationships (SAR).

Taken together, the aims of this study can be summarized as follows:

Part I: The role of VAT-1 in cancer cell migration

- Investigation into localization of VAT-1
- Generation of CRISPR/Cas9 mediated VAT-1 knockout (KO) in HeLa cells
- Analysis of several aspects of cell migration comparing KO to wild-type cells

Part II: Effects of NCA on mitochondrial functions

- Examination of important mitochondrial functions upon NCA treatment
- Identification of possible targets by ABPP
- Verification of hit targets

Part III: Structure-activity relationships of the neocarzilins and characterization of NC-4 target probe

- Testing of several neocarzilin derivatives regarding their anti-proliferative and -migratory activity
- Analysis of SAR

MATERIALS AND METHODS

3 Materials and Methods

3.1 Materials

3.1.1 Compounds

Compound	Producer/source
2-Deoxy-D-glucose	Carl Roth GmbH, Karlsruhe, Germany
Antimycin A	Enzo Life Science GmbH, Lörrach, Germany
Carbonyl cyanide m-chlorophenyl hydrazone (CCCP)	Sigma-Aldrich, Taufkirchen, Germany
Neocarzilin A Neocarzilin derivatives	Josef Braun, AK Sieber, TU Munich, Garching, Germany
Oligomycin A	Merck Millipore kGaA, Darmstadt, Germany
Probenecid	Sigma-Aldrich, Taufkirchen, Germany
Rotenon	Enzo Life Science GmbH, Lörrach, Germany
Thapsigargin	Santa Cruz Biotechnology, Dallas, TX, USA

Table 1: Compounds

3.1.2 Consumables

Consumables	Producer/source
BEEM® capsules	Electron Microscopy Sciences, Hatfield, PA, USA
Cell culture flasks: 25 cm^2, 75 cm^2	Sarstedt AG & Co. KG, Nümbrecht, Germany
Cell scraper	Th. Geyer, Renningen, Germany
Coverslip (8 x 8 mm)	H. Saur Laborbedarf, Reutlingen, Germany
Cryovials (1.8 mL)	Th. Geyer, Renningen, Germany
Disposable serological pipettes: 5 mL, 10 mL, 25 mL	Sarstedt AG & Co. KG, Nümbrecht, Germany
Eppendorf tubes (0.5 mL, 1.5 mL, 2 mL)	Eppendorf, Hamburg, Germany
FACS tubes (5 mL)	Sarstedt AG & Co. KG, Nümbrecht, Germany
Falcon tubes: 15 mL, 50 mL	Sarstedt AG & Co. KG, Nümbrecht, Germany
Hypodermic needles 25/27 G	HenrySchein®, Langen, Germany
ibiTreat μ-slides	ibidi GmbH, Munich, Germany
Injekt®-F single-use fine dosage syringes	B. Braun SE, Melsungen, Germany

Consumables	Producer/source
MicroAmp® Fast Optical 96-Well Reaction Plate, 0.1 mL	Applied Biosystems Corporation, Waltham, USA
MicroAmp® Optical Adhesive Film	Applied Biosystems Corporation, Waltham, USA
Nitrile gloves	VWR, Radnor, PA, USA
Nitrocellulose membrane (0.2/0.45 μm)	Amersham Bioscience, Freiburg, Germany
Petri dishes: 100 mm	Sarstedt AG & Co. KG, Nümbrecht, Germany
Pipette tips: 10 μL, 100 μL, 1000 μL, 5 mL	Sarstedt AG & Co. KG, Nümbrecht, Germany
Polycarbonate centrifuge tubes 11 x 34 mm	Beckmann Coulter Inc., Brea, USA
Polyvinylidene difluoride (PVDF) membrane (0.2/0.45 μm)	Amersham Bioscience, Freiburg, Germany
Syringe filter (sterile, 25 mm, 0.20 μm)	Th. Geyer, Renningen, Germany
xCELLigence CIM-plates 16	ACEA Biosciences, San Diego, CA, USA

Table 2: Consumables

3.1.3 Reagents: Biochemicals, kits, dyes, and cell culture reagents

Reagent	Producer
5x siRNA buffer	Dharmacon™, GE Healthcare, Lafayette, USA
2,2,2 Trichlorethanol (TCE)	Merck Millipore kGaA, Darmstadt, Germany
2,6-dichlorophenolindophenol (DCIP)	Sigma Aldrich, Taufkirchen, Germany
Alexa Fluor™ 647 azide triethylammonium salt	Thermo Fisher Scientific Inc., Waltham, USA
Ammonium persulfate (APS)	Merck Millipore kGaA, Darmstadt, Germany
BC assay reagent A	Interchim, Mannheim, Germany
BC assay reagent B	Interchim, Mannheim, Germany
BD™ CompBead Plus anti-mouse Ig, κ/negative control (BSA) compensation plus (7.5 μM)	BD Biosciences, Franklin Lakes, NJ, USA
Bovine serum albumin (BSA)	Merck Millipore kGaA, Darmstadt, Germany
Bradford reagent Roti® Quant	Bio-Rad Laboraties Inc., Hercules, USA
Cal520® AM	AAT Bioquest, Pleasanton, CA, USA
Calcium chloride ($CaCl_2$)	Merck, Darmstadt, Germany
CellTiter-Glo® reagent	Promega Corporation, Fitchburg, USA
Collagen G	Matrix Bioscience GmbH, Mörlenbach, Germany
Complete™	Roche Holding AG, Basel, Switzerland

Reagent	Producer
Coumaric acid	Merck Millipore kGaA, Darmstadt, Germany
Crystal violet	Carl Roth GmbH, Karlsruhe, Germany
DharmaFECT™ 1 transfection reagent	Dharmacon™, GE Healthcare, Lafayette, USA
Dimethylsulfoxide (DMSO)	Merck Millipore kGaA, Darmstadt, Germany
Di-sodium hydrogen phosphate (Na_2HPO_4)	VWR Chemicals, Radnor, PA, USA
Dithiothreitol (DTT)	Merck Millipore kGaA, Darmstadt, Germany
Dulbecco's Modified Eagle Medium (DMEM)	PAN Biotech GmbH, Aidenbach, Germany
Ethylendiaminetetraacetic acid (EDTA)	Merck Millipore kGaA, Darmstadt, Germany
Ethylene glycol tetraacetic acid (EGTA)	Sigma Aldrich, Taufkirchen, Germany
FACS flow	Becton Dickinson GmbH, Heidelberg, Germany
FACS rinse	Becton Dickinson GmbH, Heidelberg, Germany
FACS shutdown solution	Becton Dickinson GmbH, Heidelberg, Germany
Fetal calf serum (FCS)	PAN Biotech GmbH, Aidenbach, Germany
Fibronectin, human plasma (HFN)	Sigma Aldrich, Taufkirchen, Germany
FluorSave® reagent	Merck Millipore kGaA, Darmstadt, Germany
Formaldehyde solution 16% (w/v)	Thermo Fisher Scientific Inc., Waltham, USA
Glutaraldehyde 2.5% in 0.1 M sodium cacodylate buffer, pH 7.4	Electron Microscopy Sciences, Hatfield, PA, USA
Glycerol	Carl Roth GmbH, Karlsruhe, Germany
Glycine	VWR Chemicals, Radnor, PA, USA
High-Capacity cDNA Reverse Transcription Kit	Applied Biosystems Corporation, Waltham, USA
Hoechst 33342	Merck Millipore kGaA, Darmstadt, Germany
Hydroxyethyl-piperazineethane-sulfonic acid buffer (HEPES)	AppliChem, Darmstadt, Germany
JC-1 (Tetraethylbenzimidazolylcarbocyanine iodide)	Thermo Fisher Scientific Inc., Waltham, USA
Lipofectamine™ 3000 transfection reagent	Thermo Scientific, Waltham, MA, USA
Luminol	AppliChem GmbH, Darmstadt, Germany
Magnesium chloride ($MgCl_2$)	Applichem GmbH, Darmstadt, Germany

Reagent	Producer
Magnesium chloride hexahydrate ($MgCl_2$ x 6 H_2O)	Grüssing, Filsum, Germany
Methanol	Thermo Fisher Scientific Inc., Waltham, USA
MitoSOX™ Red mitochondrial superoxide indicator	Thermo Fisher Scientific Inc., Waltham, USA
MitoXpress Xtra reagent	Agilent, Santa Clara, CA, USA
NADH disodium salt	Carl Roth, Karlsruhe, Germany
Non-fat dry milkpowder (Blotto)	Carl Roth, Karlsruhe, Germany
Nonidet P 40	Sigma Aldrich, Taufkirchen, Germany
Page Ruler™ Plus prestained protein ladder	Thermo Fisher Scientific Inc., Waltham, USA
Page Ruler™ prestained protein ladder	Thermo Fisher Scientific Inc., Waltham, USA
Paraformaldehyde (PFA)	Thermo Fisher Scientific Inc., Waltham, USA
Phenylmethylsulfonyl fluoride (PMSF)	Merck Millipore kGaA, Darmstadt, Germany
Piperazine-1,4-bis(2-ethanesulfonic acid) (PIPES)	Sigma Aldrich, Taufkirchen, Germany
Rhod-2 AM	Thermo Fisher Scientific Inc., Waltham, USA
Rhodamine/PhalloidinRed	Thermo Fisher Scientific Inc., Waltham, USA
Pluronic® F-127	Sigma Aldrich, Taufkirchen, Germany
Polyacrylamide	Carl Roth GmbH, Karlsruhe, Germany
Potassium chloride (KCl)	AppliChem, Darmstadt, Germany
Potassium cyanide (KCN)	Sigma Aldrich, Taufkirchen, Germany
Potassium dihydrogen phosphate (KH_2PO_4)	Merck Millipore kGaA, Darmstadt, Germany
Potassium hydroxide (KOH)	Merck Millipore kGaA, Darmstadt, Germany
PowerUp™ SYBR® Green Master Mix	Applied Biosystems Corporation, Waltham, USA
Primers	Metabion GmbH, Planegg, Germany
Propidium iodide (PI)	Merck Millipore kGaA, Darmstadt, Germany
Pyronin Y	Merck Millipore kGaA, Darmstadt, Germany
RNeasy® Mini Kit (250)	QIAGEN GmbH, Hilden, Germany
Rotiphorese Gel 30	Carl Roth GmbH, Karlsruhe, Germany
Sodium borohydride ($NaBH_4$)	ThermoFisher, Waltham, MA, USA
Sodium chloride (NaCl)	Carl Roth GmbH, Karlsruhe, Germany
Sodium deoxycholate	Carl Roth, Karlsruhe, Germany

Reagent	Producer
Sodium dihydrogen phosphate dihydrate (NaH2PO4 x H2O)	Grüssing, Filsum, Germany
Sodiumdodecylsulfate (SDS)	Carl Roth GmbH, Karlsruhe, Germany
Sodium fluoride (NaF)	Merck Millipore kGaA, Darmstadt, Germany
Sodium orthovanadate (Na_3VO_4)	Carl Roth GmbH, Karlsruhe, Germany
Sodium pyrophosphate decahydrate ($Na_4P_2O_7$ x 10 H_2O)	Sigma Aldrich, Taufkirchen, Germany
Tris[(1-benzyl-1H-1,2,3-triazol-4-yl)methyl]amine (TBTA)	Carl Roth GmbH, Karlsruhe, Germany
Tris(2-carboxyethyl)phosphine (TCEP)	TCI Deutschland GmbH, Eschborn, Germany
Tetramethylethylendiamide (TEMED)	VWR International, Radnor, USA
Trichloroethanol (TCE)	Sigma Aldrich, Taufkirchen, Germany
Tris base	Merck Millipore kGaA, Darmstadt, Germany
Tris/HCl	Carl Roth, Karlsruhe, Germany
Triton X-100	Merck Millipore kGaA, Darmstadt, Germany
Trypsin	PAN Biotech GmbH, Aidenbach, Germany
Tween 20	Merck Millipore kGaA, Darmstadt, Germany

Table 3: Reagents

3.1.4 Technical equipment

Device	Producer
ChemiDoc™ Touch Imaging System	Bio-Rad Laboraties Inc., Hercules, USA
Bold Line incubation system	Okolab, Pozuoli, Italy
FACS Canto™ II	Becton Dickinson GmbH, Heidelberg, Germany
HeraCell incubator	Heraeus GmbH & Co. KG, Hanau, Germany
HeraSafe laminar flow	Heraeus, Hanau, Germany
Infinite® F200 pro microplate reader	Tecan, Männedorf, Switzerland
Leica DMi1 microscope	Leica, Wetzlar, Germany
Leica TCS SP8 confocal laser scanning microscope	Leica Microsystems GmbH, Wetzlar, Germany
Megafuge 1.0 RS centrifuge	Heraeus, Hanau, Germany
Micro 22R centrifuge	Hettich, Tuttlingen, Germany
Mini PROTEAN 3 chamber	Bio-Rad Laboraties Inc., Hercules, USA
Mini Trans-Blot® system	Bio-Rad, Munich, Germany
MR 3001 K magnetic stirrer	Heidolph Instruments, Schwabach, Germany
Nikon Eclipse Ti inverted microscope	Nikon, Düsseldorf, Germany
Nanodrop® Spectrophotometer	VWR International, Radnor, USA
Olympus CK30 inverted microscope	Olympus Life and Material Science GmbH, Tokyo, Japan
Optima™ MAX-XP Ultracentrifuge	Beckmann Coulter Inc., Brea, USA
Orion II microplate Luminometer	Berthold Detection Systems GmbH, Pforzheim, Germany
Oxygraph-2k	Oroboros Instruments Corp, Innsbruck, Austria
PowerPac HC, Tank Blotting System	Bio-Rad Laboraties Inc., Hercules, USA
Primus 25 advanced® Thermocycler	VWR International, Radnor, USA
Reax top vortex	Heidolph Instruments, Schwabach, Germany
QuantStudio™ 3 Real-Time PCR System	Thermo Fisher Scientific Inc., Waltham, USA
Tecan InfiniteF200pro plate reader	Tecan, Männedorf, Switzerland
Tecan SpectraFluor Plus™ Microplate Reader	Tecan AG, Männedorf, Switzerland
Tecan Sunrise	Tecan, Männedorf, Switzerland
UW 2200 Ultraschallwandler	Bandelin electronic, Berlin, Germany
Vibrax VRX basic shaker	IKA, Staufen, Germany
Vi-Cell™ XR	Beckmann Coulter Inc., Brea, USA
xCELLigence RTCA DP	Roche Diagnostics, Penzberg, Germany

Table 4: Technical equipment

3.1.5 Software

Software	Producer
Adobe Creative Cloud	Adobe, San José, CA, USA
Biorender	Biorender.com
Datlab 7.4.0.4	Oroboros Instruments Corp, Innsbruck, Austria
FACSDiva™ software	Becton Dickinson GmbH, Heidelberg, Germany
FlowJo 7.6.2	Becton Dickinson GmbH, Heidelberg, Germany
GraphPad Prism 10	GraphPad Software Inc., San Diego, CA, USA
ImageJ	National Institutes of Health, Behtesda, MD, USA
Image Lab 6.0	Bio-Rad Laborities Inc., Hercules, CA, USA
i-control™ Microplate Reader Software	Tecan, Männedorf, Switzerland
Leica LAS core X	Leica Microsystems GmbH, Wetzlar, Germany
Magelan 7.2	Tecan, Männedorf, Switzerland
Microsoft Office 365	Microsoft Corporation, Redmond, WA, USA
RTCA software 2.0	ACEA Biosiences, San Diego, CA, USA

Table 5: Software

3.2 Cell culture

3.2.1 Cell culture buffers and solutions

PBS (pH 7.4)	
NaCl	132.2 mM
Na_2HPO_4	10.4 mM
KH_2PO_4	3.2 mM
H_2O	

Trypsin/EDTA (T/E)	
Trypsin	0.05% (w/v)
EDTA	0.02% (w/v)
PBS	

PBS + Ca^{2+}/Mg^{2+} (pH 7.4)	
NaCl	137 mM
KCl	2.68 mM
Na_2HPO_4	8.10 mM
KH_2PO_4	1.47 mM
$MgCl_2$	0.25 mM
$CaCl_2$	0.5 mM
H_2O	

Growth medium	
DMEM	500 mL
FCS	50 mL

Freezing medium	
DME	70%
FCS	50 mL
DMSO	10%

Collagen G	
Collagen G	0.001%
PBS	

Table 6: Cell culture buffers and solutions

3.2.2 Cell lines

Cell line	Producer
HeLa	DSMZ, Braunschweig, Germany
HeLa VAT-1 KO 1A2, 1A3	Adrian Jauch
HeLa CRISPR control cells	Adrian Jauch

Table 7: Cell lines

HeLa, HeLa VAT-1 knockout cell lines and CRISPR control cells were cultivated in Dulbecco's Modified Eagle Medium (DMEM), supplemented with fetal calf serum (FCS, 10%) and cultured at 37 °C at constant humidity with 5% CO_2. Short tandem repeat (STR) analysis and testing for mycoplasma contamination were performed on a regular basis.

3.2.3 Passaging

When cells nearly reached confluency, they were split 1:5-1:10 and sub-cultured in 75 cm^2 culture flasks or seeded in multiwell plates or dishes for further experimental use. For that, culture medium was removed, cells were washed with pre-warmed PBS and pre-warmed trypsin/ethylenediaminetetraacetic acid (EDTA) (T/E) solution was added for 3-5 min at 37 °C to detach the cells. Trypsinization was stopped by adding culture medium and cells were counted using a ViCell® XR Cell Viability Analyzer.

3.2.4 Freezing and thawing

Before freezing, cells were cultured to reach confluency in a 175 cm^2 flask. Washing and cell detachment were conducted as described in **3.2.3**. After centrifugation (600 g, 5 min, 20 °C), cells were re-suspended in ice-cold freezing medium and transferred into cryovials at a cell density of 3×10^6 cells per 1.5 mL aliquot. Following an initial storage at -20 °C for at least 24 h and additional 24 h at -80 °C, cryovials were transferred into liquid nitrogen tanks (-196 °C) for long-term storage.

For thawing, the cryovial content was mixed with pre-warmed culture medium. After DMSO removal by centrifugation (600 g, 5 min, 20 °C), the cell pellet was re-suspended in culture medium and initially transferred into a 25 cm^2 flask for 24 h before cells were cultured in a 75 cm^2 flask.

3.2.5 Plasmid overexpression

For exogenous overexpression, cells were transfected according to the Lipofectamine™ 3000 manufacturer's instruction. Cells were seeded at a density of 2.5×10^5 cells per well in a 6-well plate the day before transfection. On the next day, the plasmid and Lipofectamine™ 3000 and P3000 reagent were diluted separately in serum-free medium and briefly vortexed. Plasmid solution was added to the Lipofectamine™/P3000 reagent containing tube, mixed by pipetting up and down and incubated for 15 min at room temperature (RT) before applying to the culture plate.

3.2.6 Stimulation with compounds

Cells were seeded the day before treatment to ensure complete attachment. DMSO stock solutions of test compounds were thawed and pre-diluted in complete growth medium. DMSO concentration did not exceed 0.1% (v/v) in any experiment.

3.2.7 Small interfering RNA (siRNA)

For gene silencing, cells were transfected according to the DharmaFECT™ Transfection Reagents siRNA transfection protocol. Cells were seeded the day before transfection. ON-TARGETplus™ siRNA or non-targeting siRNA (final concentration = 5 μM) and DharmaFECT 1 reagent were diluted in serum-free medium separately and incubated for 5 min at RT. The content of the two tubes was gently mixed by carefully pipetting up and down and incubated for 20 min at RT. In the meantime, medium in the culture vessel was replaced and subsequently siRNA lipid mix drop-wise added. Knockdown efficiency was determined after 24, 48 and 72 h by immunoblotting.

3.3 CRISPR/Cas9 knockout

To generate a VAT-1 knockout cell line in HeLa cells, the CRISPR/Cas9 system was used. Therefore, a mixture of three plasmids (sc-405997, Santa Cruz Biotechnology, Dallas, TX, USA) containing different guideRNAs (**Table 8**) and a GFP tag for visualizing successfully transfected cells (**Figure 5**) was purchased. Plasmids were transfected as described in **3.2.5** and cells incubated for 48 h.

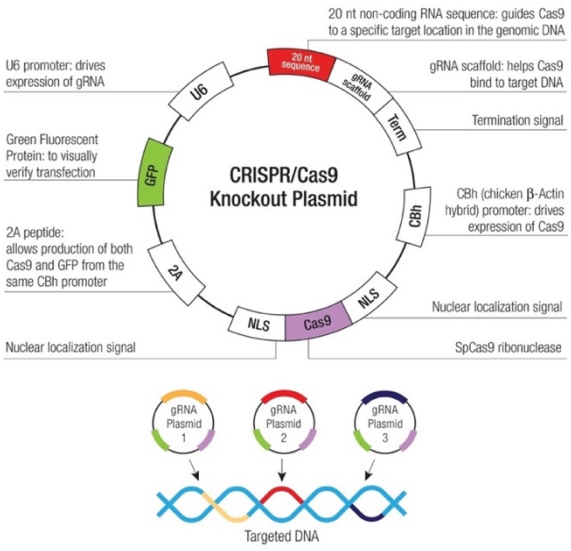

Figure 5 Architecture of CRISPR/Cas9 plasmids

Then, cells were detached, counted and 1 x 10^6 cells resuspended in 2 mL pre-warmed PBS in a sterile FACS tube for sorting (Flow Cytometry Facility, Gene Center LMU) with the following gating strategy (**Figure 6**): gate P1 to exclude cell debris, P2 + P3 to enrich single cells and exclude cell clusters, P4 for living cells (DAPI negative) and P5 for GFP positive cells (= successfully transfected). The sorted cells were directly seeded in collagen G coated 96-well plates as single cells, cultivated as described in **3.2.2** and regularly screened for growing colonies. Colonies were expanded and sequentially transferred to 24-, 6-well plates and finally 25 and 75 cm^2 flask. At this point, protein samples for knockout validation via Western blotting were taken. Further verification of successful VAT-1 deletion was done by whole proteome analysis (Josef Braun, AK Sieber, TU Munich, **3.10.1.2**). Clonal cell lines 1A2, 1A3, 3A5 were expanded, frozen as cryo-stocks and used for further experiments.

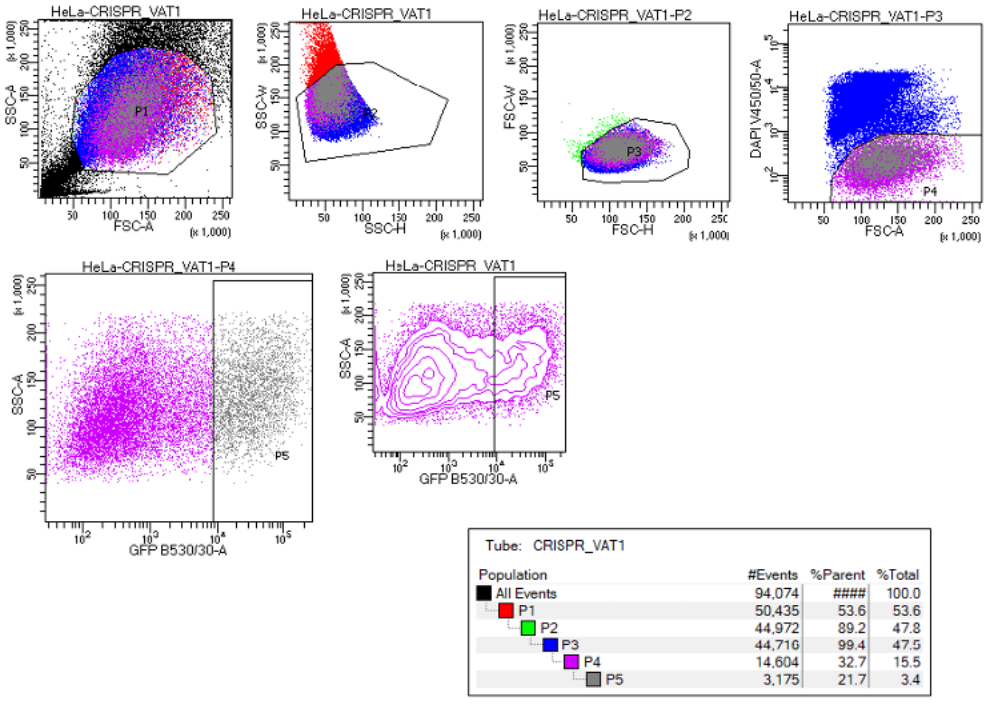

Figure 6 Gating strategy for the sorting of VAT-1 CRISPR/Cas9 plasmid mixture transfected HeLa cells

Plasmid	sgRNA sequence
sc-405997 1	CTATCACACGACTGACTACG
sc-405997 2	CAGGGCCATCAGGTTCCGTT
sc-405997 3	GTGATGGTGTTGAACCGGTC

Table 8: sgRNA sequence of VAT-1 CRISPR plasmid mixture

3.4 Flow Cytometry

Cells were analyzed by flow cytometry using a FACSCanto™ II and FACSDiva™ software. Data evaluation was performed with the flow cytometry analysis software FlowJo version 7.6.2.

3.4.1 Apoptosis assessment

1.2×10^5 HeLa cells per well were seeded in 12-well plates and incubated for 24 h at 37 °C. Treatment was performed with the indicated concentrations of NAC or DMSO for 48 h. Then, cells were washed, detached, and cell suspensions, as well as all supernatants and washing solutions were transferred into pre-cooled FACS tubes. After that, cells were pelletized by centrifugation (5 min, 600 g, 4 °C), washed with an equal volume of ice-cold PBS, centrifuged again (5 min, 600 g, 4 °C), and resuspended in 250 μL ice-cold hypotonic fluorochrome solution (**Table 9**). After incubation overnight at 4 °C in the dark, cells were analyzed. Apoptosis was determined by propidium iodide (PI) staining, as described before [64]. Since apoptosis is characterized by the loss of DNA content, the intensity of the fluorescence triggered by the binding of PI to DNA decreases in apoptotic cells (sub-G1 population).

Hypotonic fluorochrome solution (HFS)	
Propidium iodide	50 μg/mL
Sodium citrate	0.1% (w/v)
Triton X-100	0.1% (v/v)
H_2O	

Table 9: Hypotonic fluorochrome solution

3.4.2 Cytosolic calcium

To investigate changes in intracellular calcium mobilization upon NCA treatment, the cell permeable acetoxymethyl ester of the calcium sensitive dye Cal520 (Cal520-AM) was used. Once it has entered the cytosol, it is cleaved by cellular esterases, which results in a negative charge trapping the dye within the cell. Upon binding of calcium, the fluorescence

is heavily increased. HeLa cells were seeded at a density of 1.2×10^5 cells per well in 12-well plates and incubated for 24 h at 37 °C. Subsequently, cells were loaded with 5 μM Cal520 AM in HHBS (**Table 10**), 0.02% pluronic to enhance the dyes solubility and 1 mM probenicid to inhibit efflux for 2 h at 37 °C. Then, cells were detached, transferred to FACS tubes, centrifuged (5 min, 600 g, 20 °C) washed once with PBS and resuspended in 250 μL PBS supplemented with 1 mM probenicid. 10 μM NCA were added for the indicated times and mean Cal520 fluorescence was analyzed in the FITC channel and normalized to the respective DMSO control.

Hanks' buffer with HEPES (HHBS)	
$CaCl_2$	1.26 mM
D-glucose	5.56 mM
KCl	5.33 mM
KH_2PO_4	0.44 mM
$MgCl_2$ x 6 H_2O	0.49 mM
$MgSO_4$ x 7 H_2O	0.41 mM
NaCl	137.9 mM
$NaHCO_3$	4.17 mM
Na_2HPO_4	0.34 mM
HEPES	20.0 mM
H_2O	

Table 10: Hanks' buffer with HEPES

3.4.3 Mitochondrial calcium

The cell permeable acetoxymethyl ester of the rhodamine based mitochondrial calcium indicator Rhod2 (Rhod2-AM) was used to determine changes in mitochondrial calcium levels upon NCA treatment. Because of its positive charge, it accumulates in mitochondria, driven by the mitochondrial membrane potential. Once it has entered the mitochondria, it is cleaved by esterases, which results in a net negative charge trapping the dye within the organelle. Upon binding of calcium, the fluorescence is heavily increased. HeLa cells were seeded at a density of 1.2×10^5 cells per well in 12-well plates and incubated for 24 h at 37 °C. On the next day, cells were loaded with a final concentration of 5 μM Rhod2-AM in HHBS, 0.02% Pluronic to enhance the dyes solubility and 1 mM probenicid to inhibit efflux for 30 min at 37 °C. Afterwards, cells were washed once with PBS + Ca^{2+}/Mg^{2+} and

fresh medium was added. Cells were treated with NCA or DMSO at the indicated concentrations and times. Subsequently, cells were detached, transferred to pre-cooled FACS tubes, centrifuged (5 min, 600 g, 20 °C), washed once with PBS, and finally resuspended in 250 μL ice-cold PBS. Mitochondrial calcium levels were determined by the mean Rhod2 fluorescence intensity analyzed in the PE channel and normalized to the DMSO control.

3.4.4 Mitochondrial membrane potential

Tetraethylbenzimidazolylcarbocyanine iodide (JC-1) is a cell permeant cationic dye that accumulates in mitochondria driven by the mitochondrial membrane potential ($\Delta\Psi m$). If the $\Delta\Psi m$ is intact, JC-1 tends to form J-aggregates in mitochondria, exhibiting a red fluorescence. Upon loss of $\Delta\Psi m$, the dye predominantly exists in its monomeric form in the cytosol emitting green fluorescence. JC-1 staining was employed to investigate the influence of NCA on the $\Delta\Psi m$.

For this, HeLa cells were seeded at a density of 1.2×10^5 cells per well in 12-well plates and incubated for 24 h at 37 °C. Cells were treated with NCA or DMSO for 6 h at the indicated concentrations. Subsequently, cells were detached, collected, centrifuged (5 min, 600 g, 20 °C), washed once with PBS, carbonyl cyanide m-chlorophenyl hydrazone (CCCP), a protonophoric uncoupler, was added as positive control and all samples were incubated with 250 μL JC-1 (1 μg/mL) in medium for 30 min at 37 °C protected from light. Simultaneously, compensation samples were prepared using Anti-Mouse Ig, κ/Negative Control (BSA) Compensation Particles Set (Becton Dickinson GmbH, Heidelberg, Germany) and a PE Mouse IgG1, κ/ Isotype Control (#555749; Becton Dickinson GmbH, Heidelberg, Germany) and a BD Alexa Fluor™ 488 Mouse IgG1 κ Isotype Control (#557721; Becton Dickinson GmbH, Heidelberg, Germany) as described by the manufacturer. After 30 min, cells were pelletized (5 min, 600 g, 4 °C), dye solution discarded, and cells resuspended in cold PBS. Prior to analysis of cellular samples, compensation of spectral overlap was performed. The percentage of Alexa-Fluor-488-A positive and PE-A positive populations was determined as shown in **Figure 7**.

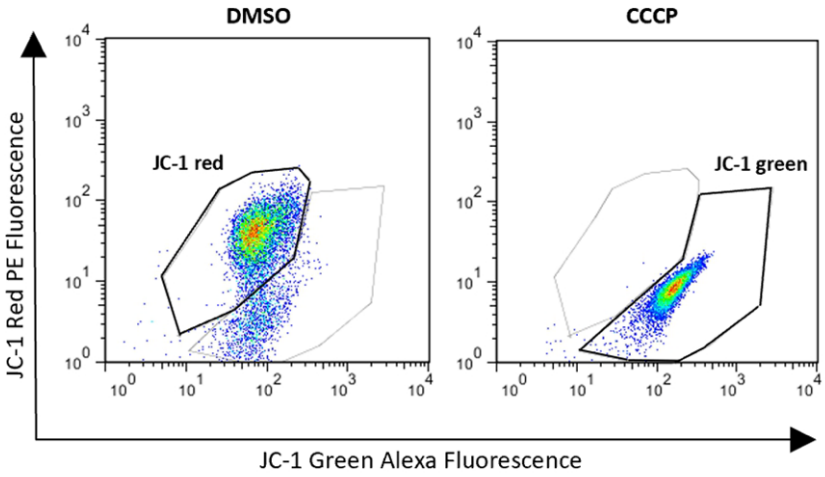

Figure 7 Gating strategy for PE-A positive and Alexa-Fluor-488-A positive populations after staining with JC-1

3.4.5 Mitochondrial superoxide

The mitochondrial superoxide indicator MitoSOX™ was used to assess changes in superoxide levels in mitochondria upon NCA treatment. The dye selectively targets mitochondria, where it rapidly gets oxidized by solely superoxide and becomes highly fluorescent.

HeLa cells were seeded at a density of 1.2×10^5 cells in 12-well plates and incubated for 24 h at 37 °C. Then, cells were treated for 6 h with NCA or DMSO at the indicated concentrations. Antimycin A, a complex III inhibitor, was used as positive control. Subsequently, cells were detached, collected, centrifuged (5 min, 600 g, 20 °C), washed with PBS and incubated with 250 μL MitoSOX™ Red Superoxide Indicator (5 μM) in HHBS for 30 min at 37 °C protected from light. Then, cells were pelletized (5 min, 600 g, 4 °C), dye solution was discarded, cells were washed once with cold PBS, resuspended in 250 μL PBS and analyzed via flow cytometry. Mitochondrial superoxide levels were determined by the mean MitoSOX™ Red fluorescence analyzed in the PE channel and normalized to DMSO control.

3.5 Migration assays

3.5.1 Wound healing assay

To assess collective cell migration, a wound healing migration assay was performed. For this, HeLa wt, VAT-1 KO 1A2, 1A3 and CRISPR control cells were seeded at a density of 3.5 x 10^4 cells/well in 96-well plates and cultured for 24 h before the scratch was applied by using a self-manufactured scratch device (**Figure 8**). Detached cells were washed away with PBS + Ca^{2+}/Mg^{2+} NCA or DMSO supplemented medium at the indicated concentrations was added to the respective wells. Plates were screened and wells with irregular scratches excluded. After 18 h, the plates were stained with crystal violet as described in **3.7.** The area of the remaining gap was calculated using ImageJ, DMSO control wells were set to 100% and -FCS negative control to 0% migration.

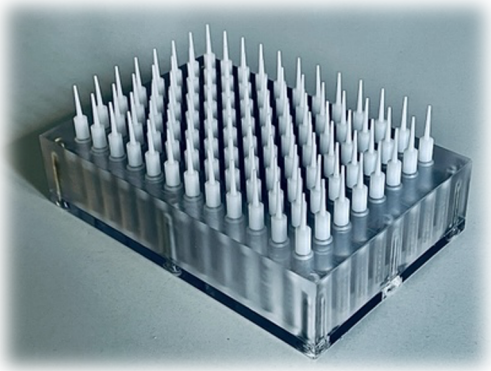

Figure 8 Self-manufactured scratch device

3.5.2 xCELLigence®

For label-free, real-time monitoring of single-cell migration, an Agilent xCELLigence® real-time cell analysis (RTCA) dual purpose (DP) instrument in combination with CIM plates (= cell invasion and migration) was used. The plates consist of an upper and lower chamber separated through a microporous membrane (8 μm pore size). The bottom side of the membrane is coated with gold biosensors that record changes in the impedance when cells migrate through the pores in the direction of a chemoattractant and adhere to their surface.

NCA or DMSO pre-stimulated medium at the indicated concentrations and medium without FCS as negative control were added to the lower chamber of a CIM-plate, which was subsequently assembled and equilibrated according to manufacturer's protocol (ACEA Biosciences, San Diego, CA, USA). HeLa cells were detached from the culture flask, pelletized by centrifugation (5 min, 600 g, 20 °C), and resuspended in medium without FCS. After counting, a cell suspension of 4 x 10^5 cells/mL was prepared, transferred to tubes, and stimulated with NCA or DMSO at the indicated concentrations and 4 x 10^4 cells seeded in the upper chamber of the equilibrated CIM-plate. After cells were allowed to settle onto the microporous membrane for 30 min at RT, the CIM-plate was placed into the xCELLigence® instrument and migration towards growth medium containing 10% FCS as chemoattractant was recorded over 18 h. The xCELLigence® device transforms the impedance into the cell index (CI), a dimensionless parameter, which is proportional to the number of migrated cells. The slope of the CI curves was evaluated as migration rate with the RTCA xCELLigence® software. The results of each biological replicate were normalized to the DMSO control, which was set to 100% migration rate.

3.6 Plate reader assays

3.6.1 CellTiter-Glo ATP assay

The intracellular ATP levels were measured using the CellTiter-Glo® (CTG) Luminescent Cell Viability Assay (Promega, Mannheim, Germany). In this assay, luciferase catalyzes the oxygenation of luciferin to oxyluciferin in the presence of Mg^{2+}, ATP, and O_2, which generates a stable luminescent signal directly proportional to the amount of intracellular ATP. Experiments were carried out according to the manufacturer's protocol (Promega, Mannheim, Germany). CellTiter-Glo® substrate was reconstituted in CellTiter-Glo® Buffer to form CellTiter-Glo® Reagent prior to use.

For this, 1 x 10^4 HeLa cells per well were seeded in a 96-well plate and were allowed to adhere overnight. On the next day, the glycolysis inhibitor 2-desoxy-glucose (2-DG) was added to medium (200 mM) and cells were treated with the indicated concentrations of NCA or DMSO for 6 h. Oligomycin, an inhibitor of the ATP synthase, was added for 1 h at the indicated concentration as positive control. The 96-well plate was equilibrated to

room temperature 30 min before measurement. Then, a volume of 100 μL CellTiter-Glo® Reagent was added to each well. To induce cell lysis, the mixture was incubated for 2 min at RT while gentle shaking. Subsequently, 150 μL of the mixture was transferred to an opaque-walled 96-well plate to reduce background noise and cross-talk between the wells while measuring luminescence. The plate was incubated at RT for 10 min and subsequently, luminescence was measured using the Orion II microplate luminometer. For statistical analysis, the results of each biological replicate were normalized to DMSO control, which was set to 100% ATP production.

3.6.2 Complex I assay

Complex I (NADH-dehydrogenase) of the respiratory chain catalyzes the electron transfer from NADH to ubiquinone.

$$NADH + Ubiquinone \leftrightarrow NAD^+ + Ubiquinol$$

The blue dye 2,6-dichlorophenolindophenol (DCIP) was used to assess the activity of complex I, since it is reduced to its colorless form by ubiquinol, which in turn gets regenerated. Because of its higher water-solubility, the ubiquinone analog decylubiquinone was used as substrate of complex I. Mitochondria from HeLa cells were enriched according to the protocol of Elly *et al*. [65] with minor modification. In brief, HeLa cells were seeded in a 75 cm^2 flask at a density of 4 x 10^6 cells and incubated for 24 h prior to stimulation with 10 μM NCA or DMSO for 6 h. Thereafter, cells were detached, collected, and washed once with PBS. Cell pellet was resuspended in ice-cold SHE buffer (**Table 11**) and immediately frozen in liquid nitrogen, thawed at 37 °C, diluted 1:1 with ice-cold SHE buffer supplemented with 0.2 mg/mL digitonin and incubated for 10 min on ice. The suspension was centrifuged (750 g, 4 °C, 10 min) to remove unpermeabilized cells and debris and the supernatant saved in a fresh tube. The pellet was resuspended in ice-cold SHE buffer supplemented with 0.1 mg/mL digitonin, again incubated for 10 min on ice, and centrifuged (750 g, 4 °C, 10 min). The supernatants were combined and centrifuged (10 000 g, 4 °C,10 min) to obtain the mitochondrial pellet. The pellet was resuspended in ice-cold KPi buffer (**Table 12**) and protein concentration determined as described in **3.10.2.3** to adjust the mitochondria amount of NCA and DMSO treated cells. Mitochondria suspensions were frozen in liquid nitrogen and thawed in a water bath at 37 °C for a

maximum of 2 min. This freeze-thaw cycle was repeated two more times. Tecan InfiniteF200Pro plate reader was pre-warmed to 37 °C and the mitochondria suspensions mixed with KPi buffer, CI premix (**Table 13**), 2 μM rotenone were added to the respective control wells and the plate incubated for 5 min at 37 °C. After that, freshly prepared 6 mM NADH solution was added to the wells and the absorbance at 595 nm was recorded over 15 min. Complex I activity was calculated by determining the slope of the linear sections of the absorption curves. Multiplying the slope by 60 gives the change of the absorption per minute. ΔA/min values were background corrected (subtraction of only buffer wells). According to the Lambert-Beer's Law, the enzymatic activity can be calculated as follows:

$$Enzyme\ activity\ [nmol/min/mg] = \frac{\Delta A/min * 1000}{\varepsilon(DCIP) * V(sample) * c(sample)}$$

$$\varepsilon(DCIP) = 19{,}1\ \frac{1}{\frac{mmol}{L} * cm}$$

To obtain complex I activity, the reaction rate in presence of rotenone was subtracted from the rate in absence of rotenone.

SHE buffer (pH 7.4)	
Sucrose	250 mM
HEPES	10 mM
EDTA	1 mM
H_2O	

Table 11: SHE buffer

KPi buffer (pH 7.4)	
K_2HPO_4	25 mM
H_2O	

Table 12: KPi buffer

CI premix	
BSA	7 g/L
DCIP	120 μM
Decylubiquinone	140 μM
Antimycin A	2 μM
KCN	4 mM
KPi buffer	

Table 13: CI premix

3.6.3 MitoXpress® Xtra Oxygen consumption assay

Oxygen consumption was measured using the MitoXpress® Xtra Oxygen Consumption assay to assess cellular respiration. MitoXpress® Xtra reagent is a cell impermeable dye, which is quenched by O_2. Therefore, the amount of fluorescence signal is inversely proportional to the amount of extracellular oxygen in the medium and can be measured in a real-time, time-resolved fluorescence manner. Experiments were carried out according to the manufacturer's protocol (Agilent, Santa Clara, CA, USA). MitoXpress® Xtra reagent was reconstituted in 1.0 mL deionized H_2O and the unused stock solution was aliquoted á 60 µL and stored at -20 °C for a maximum of one week.

First, 2.5 x 10^4 HeLa cells per well were seeded in a 96-well plate and allowed to adhere overnight. The next day, the spent culture medium was replaced with fresh pre-warmed growth medium directly before measurement. Then, 15 µL of reconstituted MitoXpress reagent and indicated concentrations of NCA, DMSO as vehicle control, and antimycin A as positive control were added to the wells in triplicates. Finally, each well was sealed by adding two drops of pre-warmed HS Mineral Oil to prevent diffusion of oxygen into the medium. Subsequently, the plate was measured kinetically in a pre-warmed (37 °C) Tecan InfiniteF200Pro plate reader for 6 h at excitation/emission 380 nm/670 nm. For statistical analysis, the absorbance of cell-free background wells containing growth medium sealed with HS Mineral Oil was subtracted at each time point. In addition, the slope of each curve between 20 min and 355 min was determined by linear regression and normalized to DMSO control, which was set 1.0-fold OCR.

3.7 Crystal violet proliferation assay

3.0×10^3 HeLa cells per well were seeded in 96-well plates and incubated for 24 h at 37 °C. Treatment was performed with the indicated concentrations for 72 h. Subsequently, cells

were washed once with PBS + Ca^{2+}/Mg^{2+}, stained with crystal violet/methanol solution (**Table 14**) for 10 min, washed with distilled water and dried overnight, before crystal violet was re-dissolved in sodium citrate solution (**Table 15**) for 10 min while gently shaking. Absorbance was measured at 550 nm using the Tecan SpectraFluor Plus™ microplate reader. Proliferation [%] was determined relative to DMSO control. Half-maximal inhibitory concentrations (IC_{50}-values) were calculated by nonlinear regression using GraphPad Prism software.

Crystal violet solution	
Crystal violet	0.5% (w/v)
Methanol	50% (v/v)
H_2O	

Table 14: Crystal violet solution

Sodium citrate solution	
Sodium citrate	0.1 M
Ethanol	50% (v/v)
H_2O	

Table 15: Sodium citrate solution

3.8 High-resolution respirometry

For high resolution respirometry measurements and detailed analysis of the electron transport chain, an Oxygraph-2k instrument was used in a cooperation with Judith Sailer (AG Zischka, TUM). For this, 2.0 x 10^6 HeLa cells were seeded in T-25 culture flasks, allowed to adhere overnight, and subsequently treated with 5.0 μM NCA or DMSO as vehicle control for 6 h for pre-treatment experiments. Then, cells were detached by trypsinization, centrifuged (200 g, 5 min, 20 °C), resuspended in 2.0 mL growth medium and cell number and viability were determined. A total of 1.5 x 10^6 cells were transferred to a new falcon, centrifuged again (200 g, 10 min, 20 °C) and subsequently resuspended in 200 μL MiR05 respiratory medium (**Table 16**). Next, cells were added to an equilibrated measuring chamber containing 2.0 mL MiR05 respiratory medium by replacement method. Cellular respiration was recorded in terms of oxygen flux based on the rate of the change of the O_2 concentration in the chambers according to the SUIT-0078O2 ce-pce D025 protocol (**Figure 9**).

First, cells were permeabilized by the addition of 5 µg/mL digitonin. Afterwards, 5 mM pyruvate and 2 mM malate were added to determine LEAK respiration. For direct titration experiments, chambers were stimulated with NCA or DMSO at the indicated at this point. Then, 2.5 mM ADP was added to determine NADH-linked respiration, followed by 10 μM cytochrome to exclude an injury of the outer mitochondrial membrane. Next, 10 mM glutamate and 10 mM succinate were added to determine the simultaneous action of NADH-linked respiration and succinate-linked respiration. For uncoupler titration, carbonyl cyanide m-chlorophenyl hydrazone (CCCP) was added to the chambers in 0.5 μM steps until cellular respiration was no longer increasing to determine maximum electron transfer capacity. The addition of 0.5 μM rotenone and afterwards 2.5 μM antimycin A was used to determine residual oxygen consumption (ROX). Subsequently, 2 mM ascorbate in combination with 0.5 mM N,N,N',N'-Tetramethyl-p-phenylenediamine dihydrochloride (TMPD) were added to measure complex-IV-linked respiration. Finally, the addition of 200 mM azide inhibited complex IV, and the measurement of chemical ROX due to autooxidation of TMPD and ascorbate was conducted.

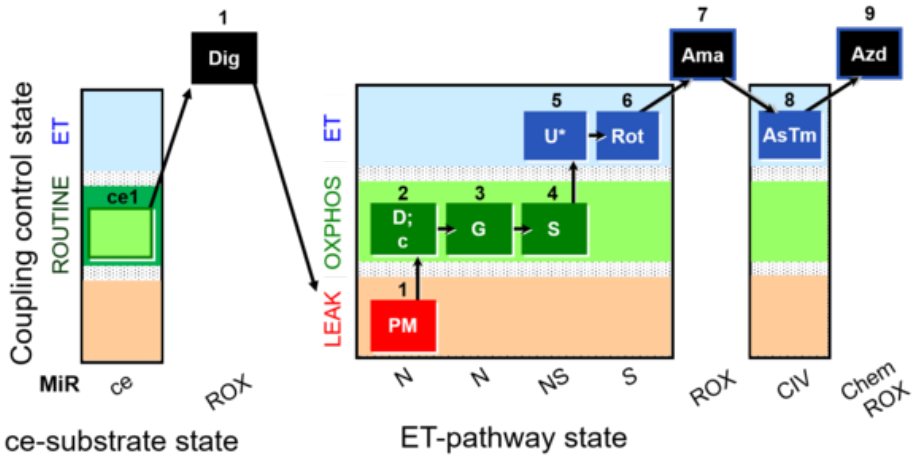

Figure 9 SUIT-0078O2 ce-pce D025 protocol
Sequential addition of substrates, uncouplers and inhibitors and measured respiration states are shown

Data were analyzed with DatLab. For this, oxygen flux was ROX (antimycin) corrected. Flux control efficiencies (**Table 17**), which express the respiratory flux in a given state relative to a reference state, were calculated.

MiR05 respiratory medium pH 7.1	
EGTA	0.5 mM
$MgCl_2$	3 mM
Lactobionic acid	60 mM
Taurine	20 mM
KH_2PO_4	10 mM
HEPES	20 mM
D-Sucrose	110 mM
BSA	1 g/L
H_2O	

Table 16: MiR05 respiratory medium

Flux control effeciencies	
R-L control efficiency	*jR-L = (R-L)/R*
P-L control efficiency	*jP-L = (P-L)/P*
E-R control efficiency	*jE-R = (E-R)/E*

Table 17: Equations of flux control effeciencies

3.9 Microscopy

3.9.1 Confocal Imaging

Confocal images were acquired utilizing a Leica TCS SP8 confocal laser scanning microscope equipped with an HC PL APO CS2 63x/1.4 oil objective and photomultiplier (PMT) or HyD detectors and Las X core software. Following excitation laser lines were applied: 405 nm, 488 nm and 647 nm. Images were further processed with ImageJ.

Antigen	Product nr.	Provider
Hsp60	sc-1052	Santa Cruz Biotechnology, Dallas, TX, USA
Integrin β1	sc-53711	Santa Cruz Biotechnology, Dallas, TX, USA
Integrin β1 active	30394	Abcam, Cambridge, UK
Rtn4/Nogo	sc-271878	Santa Cruz Biotechnology, Dallas, TX, USA
Talin1	MAB1676	Merck Millipore kGaA, Darmstadt, Germany
VAT-1	sc-515705	Santa Cruz Biotechnology, Dallas, TX, USA

Table 18: Primary antibodies for confocal imaging

Antigen	Product nr.	Provider
Donkey anti-goat IgG (H+L) Alexa-Fluor™ 633	A - 21082	Thermo Fisher Scientific Inc., Waltham, USA
Goat anti-mouse IgG (H+L) Alexa-Fluor™ 488	A-11001	Thermo Fisher Scientific Inc., Waltham, USA
Goat anti-rabbit IgG (H+L) Alexa Fluor™ 488	A - 11008	Thermo Fisher Scientific Inc., Waltham, USA
Rabbit anti-mouse IgG (H+L) Alexa Fluor™ 488	A - 11059	Thermo Fisher Scientific Inc., Waltham, USA

Table 19: Secondary antibodies for confocal imaging

3.9.1.1 Focal adhesions

HeLa wt, VAT-1 KO 1A2, 1A3 and CRISPR control cells were seeded in 6-well plates at a density of 3.5 x 10^5 cells per well and incubated overnight. On the next day, cells were starved for 4 h (DMEM w/o FSC). Then, cells were detached, centrifuged (600 g, 5 min, 20 °C), resuspended in starvation medium, counted, and 2 x 10^4 cells were re-seeded in FN coated (5 μg/cm^2, 1 h, 37 °C) ibiTreat 8-well μ-slides. After with 4% PFA in PBS for 15 min, washed once with PBS, permeabilized with 0.1% Triton-X-100 for 10 min, washed again and blocked with 5% BSA for 1 h at RT. Focal adhesions were stained by incubating a primary Talin1 antibody overnight at 4 °C, followed by indirect detection with a suitable Alexa Fluor™ 488 coupled secondary antibody. Focal adhesions were analyzed according to the protocol of Horzum *et al.* [66] with ImageJ.

3.9.1.2 Integrin activation

HeLa wt, VAT-1 KO 1A2, 1A3 and CRISPR control cells were seeded in 6-well plates at a density of 3.5 x 10^5 cells per well and incubated overnight. On the next day, cells were starved for 4 h (DMEM w/o FSC). Then, cells were detached, centrifuged (600 g, 5 min, 20 °C), resuspended in starvation medium, counted, and 2 x 10^4 cells were re-seeded in FN coated ibiTreat 8-well μ-slides and allowed to adhere for 2 h at 37 °C. After that, cells were fixed, permeabilized and blocked as described in **3.9.1.1** One well of each population was stained with an antibody raised against total and one against the active form of integrin β1. The mean grey values were analyzed using ImageJ and activation of integrin β1 calculated by correcting the intensity of the active form with the total expression.

3.9.1.3 Microtubulin staining

For microtubule staining, 3 x 10^4 HeLa cells per well were seeded in an ibiTreat 8-well μ-slide and incubated overnight. On the next day, cells were treated with the indicated concentrations of NCA or DMSO for 6 h. Then they were washed once with PBS + Ca^{2+}/Mg^{2+} and extraction buffer (**Table 20**) was added for 30 sec, before fixing them with 5% (v/v) glutaraldehyde for 10 min. Glutaraldehyde was quenched with 0.1% (w/v) $NaBH_4$ for 7 min and cells washed three times with PBS and blocked with 5% BSA (v/v) for 1 h. The b-tubulin primary antibody was incubated overnight at 4 °C and on the next day, after washing the wells three times with PBS the respective secondary antibody and Hoechst 33342 (2.5 μg/mL) was applied for 1 h at RT. Finally, cells were washed again three times with PBS and sealed with FluorSave™.

Extraction buffer 5x	
EGTA	5 mM
$MgCl_2$	5 mM
PIPES	400 mM
Triton-X-100	0.5% (v/v)
H_2O	

Table 20: Extraction buffer 5x

3.9.1.4 Mitochondrial network analysis

HeLa cells were seeded at a density of 3 × 10^4 cells per well into ibiTreat 8-well μ-slides and incubated for 24 h at 37 °C. After stimulation with the indicated concentrations of NCA for 3 and 6 h, cells were stained for Hsp60 as mitochondrial marker and counter-stained with Hoechst 33342 (2.5 μg/mL). For quantitative analysis of the mitochondrial network, the MiNA analysis plugin in ImageJ was employed. This tool and documentation regarding its usage are available at https://github.com/StuartLab/MiNA. Before running the macro, images were converted to 8-bit. Briefly, the macro MiNA allows pre-processing of the image to enhance image quality prior to analysis to provide more accurate results (median filter: radius = 1, unsharp mask: radius (sigma) = 5, mask weight = 0.5). Then, the tool skeletonizes the mitochondrial network and calculates the mean branch length (length of each single mitochondrion), the mean branches per network (extent of mitochondrial branching per network) and the mean summed branches length (size of each individual network). Furthermore, an image with an overlay of the binarized mitochondria and the

skeletal model is generated. Each pixel of the skeleton is classified, whereby green pixels represent the length of the mitochondria, blue pixels the connection sites between two mitochondria and yellow pixels the end of a network structure, respectively. In addition, before skeletonizing the area of the image occupied by the mitochondrial signal was analyzed, which is depicted as a purple outline.

3.9.1.5 NC-4 labeling

HeLa cells were seeded in ibiTreat 8-well μ-slides at the density of 3.5 x 10^4 cells/well and incubated for 24 h at 37 °C. Cells were then labeled with 20 μM NC-4 or DMSO for 1 h. Afterwards, medium was removed and wells were washed once with PBS + Ca^{2+}/Mg^{2+} and fixed with PFA, followed by permeabilization with 0.1% Triton-X-100 and blocking with 5% BSA. In the meantime, fresh premixed click chemistry mix was prepared (**Table 21**). 200 μL click mix was added per well, and the slide was incubated for 2 h in the dark at RT while vigorously shaking. Then, cells were washed thrice with PBS and incubated with a primary anti-Rtn4 antibody overnight at 4 °C. On the next day, wells were washed thrice with PBS and subsequently incubated with an Alexa Fluor™ 488 labeled anti-mouse secondary antibody and counter-stained with Hoechst 33342 (2.5 μg/mL) for 1 h at RT. After another 3 washing steps with PBS, wells were mounted, covered with a glass slip, and imaged with a Leica TCS SP8 confocal microscope. 50 cells per repetition were analyzed and co-localization of the green and red channel was quantified with the help of the Coloc2 ImageJ plugin and delineated as mean Pearson's r value.

Click chemistry reaction mix	
Alexa Fluor ™ 647 azide	10 μM
$CuSO_4$	1 mM
TBTA	100 μM
TCEP	1 mM
PBS	

Table 21: Click chemistry reaction mix

3.9.1.6 Spreading assay

In a pre-experiment, proper settling time of HeLa wild-type cells was determined for the spreading assay (**3.9.3.2**). HeLa wt, VAT-1 KO 1A2, 1A3 and CRISPR control cells were

seeded in 6-well plates at a density of 3.5 x 10^5 cells per well and incubated overnight. On the next day, cells were starved for 4 h (DMEM w/o FSC). Then, cells were detached, centrifuged (600 g, 5 min, 20 °C), resuspended in starvation medium, counted, and 1 x 10^4 cells were re-seeded in FN coated (5 μg/cm^2, 1 h, 37 °C) ibiTreat 8-well μ-slides and allowed to adhere and spread for 60 min at 37 °C. Afterwards, cells were fixed with 4% PFA, washed once with PBS and actin cytoskeleton and nuclei were stained with rhodamine-phalloidin and Hoechst 33342 (2.5 μg/mL) for 1 h at RT followed by three washing steps with PBS and mounting. Spreading area and shape were analyzed with ImageJ particle analysis.

3.9.2 Live cell imaging

Live cell imaging was performed using a Leica TCS SP8 confocal microscope (**3.9.1**) equipped with a Bold line incubation system.

3.9.2.1 ER vacuole staining

HeLa cells were transfected with DsRed2-ER plasmid which was a gift from Michael Davidson (Addgene plasmid # 55836) as described in **3.2.5** and incubated for 24 h before re-seeding 3 x 10^4 cells per well in an ibiTreat 8-well μ-slide. After additional 24 h, cells were stimulated with 10 μM NCA or DMSO for 6 h. 30 min before imaging Hoechst 33342 (2.5 μg/mL) was added. Then, medium was removed and replaced with fresh one and live cell imaging was performed.

3.9.2.2 Mitochondrial superoxide

For imaging of mitochondrial reactive oxygen species (mROS) production after NCA treatment, the mitochondrial superoxide indicator MitoSOX^{TM} described in **3.4.5** was used in a live cell imaging. HeLa cells at a density of 3 x 10^4 cells per well were seeded in an ibiTreat 8-well μ-slide and icubated for 24 h at 37 °C. On the next day, cells were treated with NCA or DMSO at the indicated concentrations for 3 and 6 h and then loaded with a final concentration of 5 μM MitoSOX^{TM} indicator in HHBS for 30 min at 37 °C. Afterwards, cells were gently washed three times with pre-warmed PBS + Ca^{2+}/Mg^{2+} and counter-stained with Hoechst 33342 (2.5 μg/mL) in PBS + Ca^{2+}/Mg^{2+} for 15 min at 37 °C. Finally, cells were washed twice with PBS + Ca^{2+}/Mg^{2+} and 250 µL of pre-warmed growth medium was added and cells imaged.

3.9.3 Phase contrast microscopy

For phase contrast microscopy, a Leica Dmi1 equipped with a Leica MC120 HD camera was used. Images were further processed with ImageJ.

3.9.3.1 Cytoplasmic vacuolization

1.2 x 10 HeLa cells were seeded in 12-well plates the day before imaging and incubated for 24 h at 37 °C. On the next day, cells were treated with NCA at the indicated concentrations or DMSO and pictures were taken after 1, 2, 3, 4, 5 and 6 h.

3.9.3.2 Pre-experiment spreading assay

In a pre-experiment, proper settling time of HeLa wild-type cells, VAT-1 KO 1A2, 1A3 and CRISPR control cells was determined for the spreading assay (**3.9.1.6**). For this, 1 x 10^4 cells per well were seeded in 96-well plate and picture were taken after 5, 15, 30, 60, 90 and 120 min.

3.9.4 Transmission electron microscopy

For transmission electron microscopy (TEM), 2.5 x 10^6 HeLa cells were seeded in 100 mm dishes 24 h prior to stimulation with NCA at the indicated concentrations for 6 h. Then, cells were detached, counted, and 3.5 x 10^5 cells per condition were transferred to a BEEM® capsule. Cells were pelleted, the supernatant removed, the pellet carefully overlaid with 600 µL 2.5% glutaraldehyde and stored at 4 °C for at least 24 h. Embedding and further preparation of the samples as well as imaging were performed by Carola Eberhagen in the laboratory of Prof. Dr. Hans Zischka (Institute of Molecular Toxicology and Pharmacology, Helmholtz Centre, Munich).

3.10 Proteomics

3.10.1 Mass spectrometry (MS)

All protein mass spectrometry (LC-MS/MS) experiments were conducted by Josef Braun in the laboratory of Prof. Dr. Stephan Sieber (TU Munich, Garching, Germany) using an

UltiMate 3000 nano HPLC system equipped with an Acclaim C18 PepMap100 trap and a 25 cm Aurora Series emitter column coupled to an Orbitrap Fusion in EASY-spray setting.

3.10.1.1 Activity-based protein profiling (ABPP)

NCA target identification was performed by Josef Braun in the laboratory of Prof. Dr. Stephan Sieber (TU Munich, Garching, Germany) using activity-based protein profiling. Briefly, cells were seeded in 6-well plates and grown till they reached 90% confluency. Then, cells were labeled with 250 nM of the neocarzilin target probe NC-4 for 1 h in PBS at 37 °C. For competition experiments, cells were preincubated with 25 μM of the original natural compound NCA. Subsequently, cells were washed with ice-cold PBS, scraped off, transferred to tubes, and pelletized by centrifugation (600 g, 10 min, 4 °C). Cell lysis was performed with PBS supplemented with NP40 1% (v/v) and sodium deoxycholate 1% (w/v) by incubating the pellet on ice for 15 min. Protein amount was determined using BCA assay and adjusted to 1 μg in 1 mL. Then, click chemistry was performed to couple the target probe to biotin-PEG-azide for 1 h at RT. Proteins were precipitated, washed, and enriched on avidin agarose beads. Samples were digested overnight, desalted and either lyophilized and stored at -80 C or reconstituted in formic acid for LC-MS/MS analysis.

3.10.1.2 Whole proteome analysis

HeLa wild-type, VAT-1 KO 1A2 and 1A3 or CRISPR control cells were seeded at a density of 2.5 x 10^5 cells per well in 6-well plates and incubated overnight at 37 °C. On the next day, cells were treated with the indicated concentration of NCA or DMSO for the indicated times. For the CRISPR/Cas9 verification, cells were left untreated. Then, cells were washed once with ice-cold PBS, lysis buffer (1% (v/v) NP40 + 1% (w/v) sodium deoxycholate in PBS) was added, and cells scrapped off. Cell suspensions were briefly vortexed and incubated for 30 min on ice before centrifugation (20 000 g, 15 min, 4 °C) to remove cell debris. Protein concentration was determined using BCA assay and adjusted to 0.5 mg/mL. Further processing and whole proteome analysis was performed by Josef Braun in the laboratory of Prof. Dr. Stephan Sieber (TU Munich, Garching, Germany).
Briefly, samples were precipitated in acetone, pelletized by centrifugation, washed twice with methanol and denaturated. Then, reduction and alkylation were performed, followed by digestion and desalting. Samples were lyophilized and stored at -80 °C before analysis.

3.10.1.2.1 Bioinformatics

MS data were processed using MaxQuant 1.6.2.10 and performed by Josef Braun in the laboratory of Prof. Dr. Stephan Sieber (TU Munich, Garching, Germany).

3.10.1.2.2 Ingenuity pathway analysis (IPA)

Pathway analysis was conducted by Jun.-Prof. Dr. Franziska Traube (University of Stuttgart, Stuttgart, Germany) using the QIAGEN IPA software.

3.10.2 Immunoblotting

3.10.2.1 Cell lysis

Cellular protein levels were analyzed by Western blotting. For lysis, medium was discarded, and cells were washed with ice-cold PBS before adding RIPA lysis buffer (**Table 22**). Subsequently, cells were scraped off, transferred to tubes, briefly vortexed and incubated on ice for at least 30 minutes. In order to remove cell debris, lysates were centrifuged (20 000 g, 15 min, 4 °C), followed by storage at -20 °C, if not immediately processed further.

RIPA lysis buffer	
NaCl	150 mM
Nonidet NP-40	1% (w/v)
Tris/HCl	50 mM
SDS	0.10% (w/v)
Sodium deoxycholate	0.25% (w/v)
H_2O	
added before use:	
Complete®EDTAfree	4 mM
NaF	1 mM
$Na_4P_2O_7$	1 mM
Na_3VO_4	2 mM
PMSF	0.5 mM

Table 22: RIPA lysis buffer

3.10.2.2 Subcellular fractionation

To assess protein localization and enrichment or depletion of proteins from specific cellular compartments, centrifugation based subcellular fractionation was performed according to the abcam protocol with minor modifications. Briefly, 2.0 - 2.5 x 10^6 HeLa cells were seeded in 100 mm dishes and incubated for 24 h at 37 °C prior to stimulation with NCA at the indicated concentrations and times. Then, cells were washed twice with 5 mL ice-cold PBS, 350 μL subcellular fractionation buffer (**Table 23**) was added per dish and cells immediately scraped off with a rubber policeman. The cell suspension was passed 10 x through a 27-gauge needle and incubated for 20 min on ice. To separate the nuclear fraction, the suspension was centrifuged at 720 g and 4 °C for 5 min. The nuclear pellet was washed by adding 500 μL fractionation buffer and resuspended by passing it 10 x through a 25-gauge needle followed by centrifugation under the aforementioned settings. Washing buffer was removed, the pellet dispersed in the nuclear buffer (**Table 24**) and sonicated for 3 sec. The supernatant containing the mitochondrial, cytosolic and membrane fraction was transferred to a fresh tube and centrifuged at 10 000 g and 4 °C for 10 min to obtain the mitochondrial pellet. The mitochondrial pellet was washed as described for the nuclear pellet, re-centrifuged at 10 000 g and 4 °C for 10 min and resuspended in RIPA buffer. The supernatant with the cytosolic and membrane fraction was transferred to a thick-walled polycarbonate tube and ultra-centrifuged at 100 000 g and 4 °C for 1 h. The supernatant representing the cytosolic fraction was transferred to a fresh tube and the membrane pellet washed by resuspending it in 400 μL fractionation buffer as for the nuclear and mitochondrial pellet, re-centrifuged under the same conditions for additional 45 min and resuspended in RIPA buffer.

Subcellular fractionation buffer	
Sucrose	250 mM
HEPES (7.4)	20 mM
KCl	10 mM
MgCl2	1.5 mM
EDTA	1 mM
EGTA	1 mM
H_2O	
added before use:	
Complete®EDTAfree	4 mM
DTT	1 mM

Table 23: Subcellular fractionation buffer

Nuclear buffer	
RIPA	250 mM
Complete®EDTAfree	4 mM
PMSF	0.5 mM
Glycerol	10% (v/v)
SDS	0.1% (m/v)

Table 24: Nuclear buffer

3.10.2.3 Protein quantification and sample preparation

To ensure equal protein loading, protein concentration was determined via Bradford assay as described previously [67] or BCA assay. In detail, 5 μL of cell lysate were diluted in water 1:5 (v/v) and 10 μL of the prepared dilution were transferred to a 96-well plate in triplicates. Concomitantly, bovine serum albumin (BSA) standards (0-500 μg/mL for Bradford and 31.25-2000 μg/mL for BCA) were transferred to the 96-well plate. Bradford reagent was diluted 1:5 (v/v) in water, for BCA 10 mL reagent A and 200 μL reagent B were mixed and added to the samples (Bradford 190 μL/well, BCA 200 μL/well), followed by incubation (Bradford: 5 min at RT under gentle agitation, BCA: 30 min at 37 °C). Bradford assay is an addition of coomassie brilliant blue G-250 to protein solutions. The coomassie blue dye associates with basic and aromatic amino acids, thereby causing a shift in absorbance during protein determination. BCA assay is the addition of bicinchonic acid and copper(II) sulfate to protein solutions. Peptides reduce Cu^{2+} to Cu^{1+} which gets chelated by bicinchonic acid, resulting in a purple complex. Absorbance of each sample at 592 nm (Bradford) or 550 nm (BCA) was determined by photometric measurement using

a Tecan SpectraFluor Plus™ microplate reader and linear regression was conducted with BSA dilutions as protein standards. Subsequently, 5x SDS sample buffer (**Table 25)** was added to the samples and protein concentration was adjusted by adding 1x SDS sample buffer. Afterwards, the samples were heated at 95 °C for 5 min and stored at -20 °C before gel electrophoresis.

SDS sample buffer 5x	
DTT	2% (w/v)
Glycerol	50% (v/v)
Pyronin Y	0.025% (w/v)
SDS	5% (w/v)
Tris/HCl pH 6.8	3.125 M
H_2O	

Table 25: SDS Sample Buffer 5x

3.10.2.4 SDS-PAGE and tank blotting

For separation of proteins, discontinuous SDS- polyacrylamide gel electrophoresis (SDS PAGE) was performed. Equal amounts of protein samples were loaded on discontinuous polyacrylamide gels, consisting of a gradient separation (4 -20%) and a stacking gel.

The Mini Protean 3 system chamber from Bio-Rad was filled with electrophoresis buffer, followed by electrophoresis at a current of 100 V for 21 min and at 200 V for 45 min for protein stacking and separation, respectively. To determine the molecular weight of detected proteins, a pre-stained protein ladder PageRuler Plus™ was subjected to gel electrophoresis in parallel.

Separation Gel (4-20%)	
APS	0.05% (w/v)
Rotiphorese™ Gel 30	40-80% (v/v)
SDS	0.1% (w/v)
TCE	0.5% (w/v)
TEMED	0.1% (v/v)
Tris-HCl (pH 8.8)	375 mM
H_2O	

Stacking Gel	
APS	0.1% (w/v)
Rotiphorese™ Gel 30	17% (v/v)
SDS	0.1% (w/v)
Tris-HCl (pH 6.8)	125 mM
TEMED	0.2% (v/v)
H_2O	

Electrophoresis buffer	
Glycine	38 mM
SDS	0.1% (w/v)
Tris	4.9 mM
H_2O	

Table 26: Composition of buffers and gel mixtures for gel electrophoresis

Prior to tank blotting, protein load was determined by stain free detection of trichloroethanol (TCE) supplemented gels using the ChemiDoc Touch Imaging System. Subsequently, proteins were transferred onto a PVDF or NC membrane by tank blotting. PVDF membranes were equilibrated in methanol for 20 sec, ultra pure water for 20 sec and tank buffer (**Table 27**) for 5 min, NC membranes only in ultra pure water and tank buffer for the same times before a blotting sandwich (fiber pad – blotting paper – separation gel –membrane – blotting paper – fiber pad) was prepared and put into the Mini Trans-Blot® system that was subsequently filled with tank buffer. Proteins were transferred at 4 °C utilizing a constant current of 100 V for 90 min.

Tank buffer	
Glycine	39 mM
Methanol	20% (v/v)
Tris base	48 mM
H_2O	

Table 27: Tank buffer

3.10.2.5 Protein detection

After tank blotting, membranes were blocked with a 5% (w/v) solution of BSA in PBS for 2 h at RT to avoid unspecific binding of primary antibodies. Subsequently, membranes were incubated with primary antibody solution (**Table 28**) at 4 °C under gentle agitation overnight. Primary antibodies were diluted 1:1000 (v/v) in 1% (w/v) BSA in PBS. On the next day, membranes were washed four times with TBS-T (Tris-buffered saline + Tween 20) (**Table 30**) and incubated with an appropriate HRP-linked secondary antibody (**Table 29**) for 2 h at RT. After additional four washing steps with TBS-T, enhanced chemiluminescence (ECL) imaging was used to detect antibody signals on membranes. In detail, proteins were detected by HRP-linked oxidation of luminol and chemiluminescence detection by incubating membranes for 1 min in ECL solution (**Table 31**) and developing membranes directly on the ChemiDoc Touch imaging system. Further data evaluation was performed with Image Lab software.

Antigen	Product nr.	Provider
ATF4	sc-390063	Santa Cruz Biotechnology, Dallas, TX, USA
Bid	2002	Cell Signaling Technology Inc., Danvers, MA USA
BiP/GRP78	610978	BD Biosciences, Franklin Lakes, NJ, USA
Caspase 3	sc-714	Santa Cruz Biotechnology, Dallas, TX, USA
Caspase 8	9746	Cell Signaling Technology Inc., Danvers, MA USA
Caspase 9	9502	Cell Signaling Technology Inc., Danvers, MA USA
Cytochrome c	4272	Cell Signaling Technology Inc., Danvers, MA USA
DRP1	8570	Cell Signaling Technology Inc., Danvers, MA USA
eIF2α	sc-133132	Santa Cruz Biotechnology, Dallas, TX, USA
GAPDH	5174	Cell Signaling Technology Inc., Danvers, MA USA
Hsp60	sc-1052	Santa Cruz Biotechnology, Dallas, TX, USA
LC-3 I & II	4108	Cell Signaling Technology Inc., Danvers, MA USA
Mfn1	14739	Cell Signaling Technology Inc., Danvers, MA USA
OPA1	80471	Cell Signaling Technology Inc., Danvers, MA USA
panCadherin	sc-515872	Santa Cruz Biotechnology, Dallas, TX, USA
PARP	9542	Cell Signaling Technology Inc., Danvers, MA USA
p-eIF2α	9721	Cell Signaling Technology Inc., Danvers, MA USA
Rtn4/Nogo	sc-271878	Santa Cruz Biotechnology, Dallas, TX, USA
Talin1	MAB1676	Merck Millipore kGaA, Darmstadt, Germany
VAT-1	sc-515705	Santa Cruz Biotechnology, Dallas, TX, USA

Table 28: Primary antibodies for Western blot analysis

Antigen	Product nr.	Provider
HRP, donkey-anti-goat IgG	ab97120	Abcam, Cambridge, UK
HRP, goat-anti-mouse IgG_1	ab97240	Abcam, Cambridge, UK
HRP, goat-anti-mouse IgG_{2a}	1080-05	Southern Biotech Assoc., Birmingham, AL, USA
HRP, goat-anti-mouse IgG_{2b}	1090-05	Southern Biotech Assoc., Birmingham, AL, USA
HRP, goat-anti-rabbit IgG (H+L)	172-1019	Bio-Rad Laboratories Inc., Hercules, CA, USA

Table 29: Secondary antibodies for Western blot analysis

TBS-T (pH 7.6)	
Glycin	190 mM
Tris-base (pH 8.0)	24.8 mM
Tween 20	0.1% (v/v)
H_2O	

Table 30: TBS-T washing buffer

ECL solution	
Coumaric acid	1 mM
H_2O_2	17 μM
Luminol	2.5 mM
Tris (pH 8.5)	100 mM
H_2O	

Table 31: ECL solution

3.11 Quantitative real-time PCR analysis

Real-time quantitative PCR analysis was used to monitor changes in gene expression on mRNA level. For the isolation of the mRNA, the RNeasy® Mini Kit (250) was used as described by the manufacturer and mRNA concentration was determined using a Nanodrop® spectrophotometer. Subsequently, reverse transcription was performed with the High-Capacity cDNA Reverse Transcription Kit according to the manufacturer's instructions. For the quantitative real-time polymerase chain reaction (qPCR), a QuantStudio™ 3 Real-Time PCR System was employed. CHOP primer sequences were adopted from Oslowski *et al.* [48] and GAPDH primers were designed using the NCBI database. (**Table 32)**. Primers were purchased from metabion (Planegg, Germany). 100 ng of cDNA (2 μL), 6.25 μL PowerUp™ SYBR® Green Master Mix, 3.75 μL RNase-free water and 0.025 mol of each primer (0.25 μL) were used for each well of the MicroAmp® Fast Optical 96-Well Reaction Plate, 0.1 mL and sealed with an adhesive film. The $\Delta\Delta C_T$ method was used to quantify changes in mRNA levels as described earlier [68] and GAPDH was used as housekeeping gene. Previously, primer efficiency was determined for each primer pair using 500 ng, 50 ng and 5 ng of cDNA per well.

Target Name	FW/RV Primer	Sequence (5'-3')
CHOP	FW	AGA ACC AGG AAA CGG AAA CAG A
CHOP	RV	TCT CCT TCA TGC GCT GCT TT
GAPDH	FW	ACG GGA AGC TTG TCA TCA AT
GAPDH	RV	CAT CGC CCC ACT TGA TTT T

Table 32: Primers with nucleotide codes used for qPCR analysis

3.12 Statistical analyses

All experiments were conducted at least three times unless indicated otherwise in the figure legends. The given data are presented as means ± SD. Statistical differences between groups were assessed with a t-test (with Welch's correction as indicated) or with an ordinary one-way and two-way ANOVA, respectively, and the indicated multiple comparisons test. Statistical analyses were performed with GraphPad Prism software. Statistically significant results are indicated in the figures. If no indication of significance is given, data are not statistically significant.

RESULTS

4 Results

4.1 Part I: VAT-1 is important for proper cell spreading and focal adhesion dynamics and thereby influences cancer cell migration

4.1.1 VAT-1 localizes to mitochondria and membranous fractions

To learn more about a protein's function, one important aspect is their intracellular distribution. Because there are large discrepancies about the localization of VAT-1 in the literature [citation], a centrifugation based subcellular fraction with subsequent Western blot analysis was performed (**Figure 10**). Thereby nuclear, mitochondrial, cytosolic and membrane fractions were obtained, and their quality and purity proven by blotting respective organelle markers. Here, histone H3 for the nuclear, heat shock protein 60 (Hsp60) for the mitochondrial, glyceraldehyde-3-phosphate dehydrogenase (GAPDH) for the cytosolic and pan-cadherin for the membrane fraction were used.

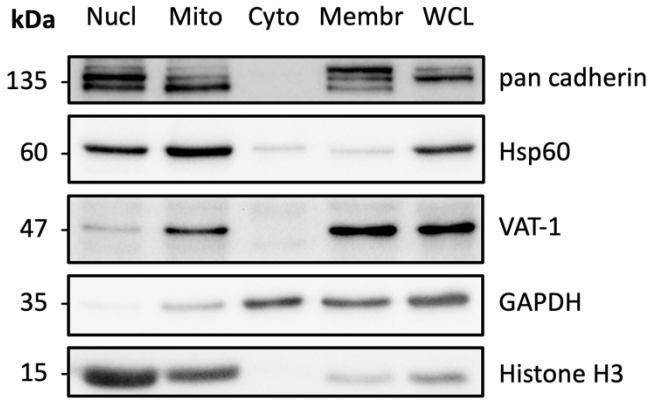

Figure 10: VAT-1 localizes at mitochondrial and membranous fractions.
Representative Western blot of subcellular fractionation of HeLa cells, n=3.
Nucl = nuclear, mito = mitochondrial, cyto = cytoplasmic,
membr = mebranous fraction, WCL = whole cell lysate.

VAT-1 mainly localizes at mitochondrial and membrane containing fractions, which was demonstrated in three independent repetitions.

For further confirmation of those findings, immunocytochemistry/immunofluorescence (ICC/IF) experiments were conducted. First, the VAT-1 primary antibody used for the subcellular fractionation was validated for ICC/IF application by knockdown experiments. For this, HeLa cells were transfected with VAT-1 siRNA, protein levels were determined by immunoblotting (**Figure 11-A**) and VAT-1 expression was found to be reduced to 37% after 24 h and 16% after 48 h, reaching the maximal knockdown efficiency after 72h with only 5% remaining protein expression. Therefore, this transfection period was chosen for further validation of the antibody. In an immunofluorescence experiment (**Figure 11-B**) a pronounced reduction of the VAT-1 signal could be shown after 72 h siRNA incubation, proving the suitability of the antibody for ICC/IF application.

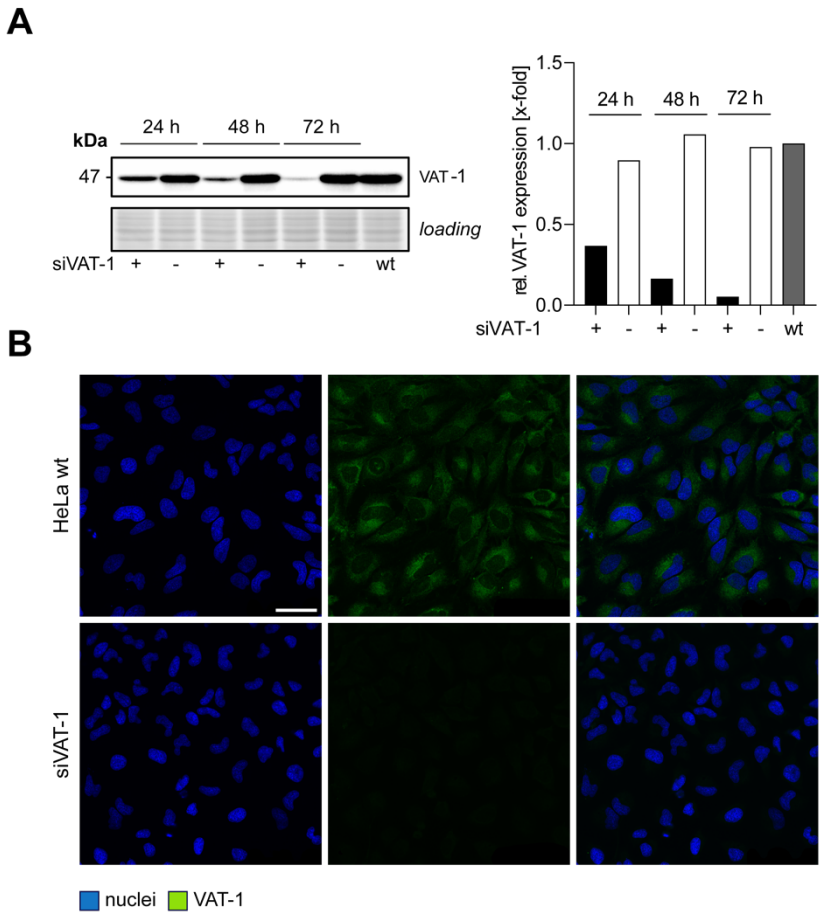

Figure 11 Antibody validation via knockdown experiments.
(**A**) siRNA mediated knockdown of VAT-1 in HeLa cells evaluated via immunoblotting after 24, 48 and 72 h, compared to non-targeting control siRNA and normalized to HeLa wt cells, n=1. (**B**) Representative images of immunofluorescence staining of siVAT-1 transfected HeLa cells (72 h) vs. HeLa wt cells, with nuclei in blue and VAT-1 in green (scale bar 50 μm), n=3.

Next, a co-immunofluorescence staining of VAT-1 and Hsp60 as mitochondrial marker was performed (**Figure 12**). 25 cells per repetition were analyzed with the Coloc2 ImageJ plugin and Pearson's r values evaluated. The results show a strong correlation of the VAT-1 and Hsp60 signal with a mean Pearson's r coefficient of 0.67. This indicates a colocalization of VAT-1 at mitochondria and thereby confirms the results obtained by the subcellular fractionation experiments.

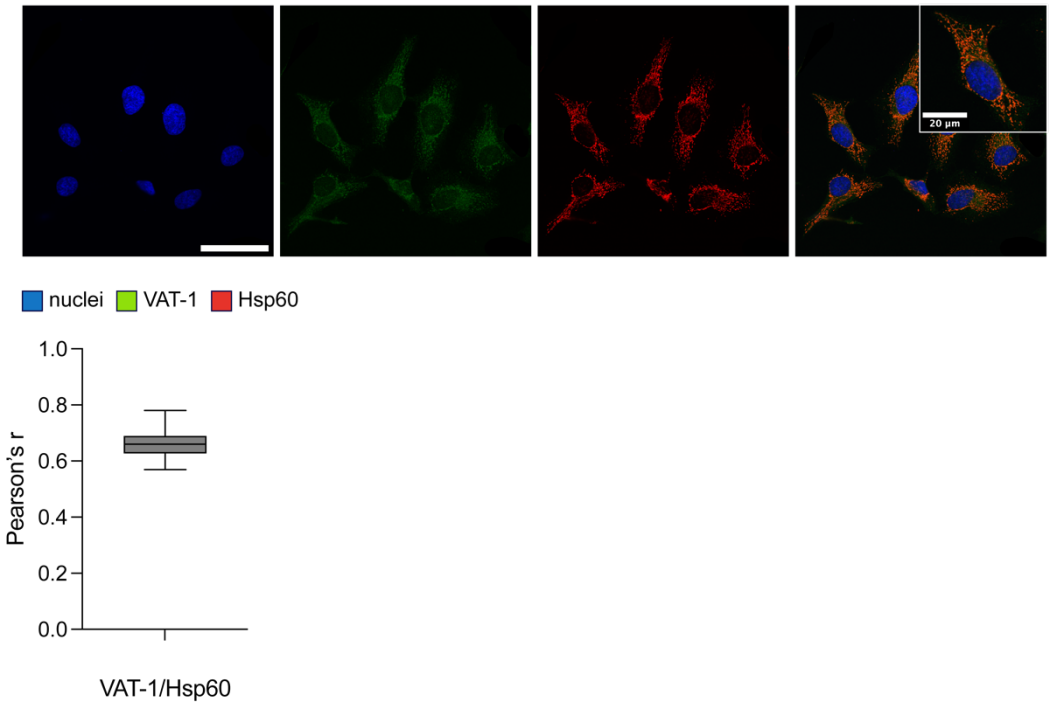

Figure 12 Co-staining of VAT-1 and mitochondrial marker Hsp60 shows strong correlation.
Representative images of immunofluorescence staining in HeLa cells, nuclei shown in blue, VAT-1 in green and Hsp60 in red. Orange area indicate a coincidence of the red and green signal (scale bar 50 μm). 25 cells per repetition were analyzed with the ImageJ Coloc2 plugin and mean Pearson's coefficient calculated. Data are presented as box and whiskers (min to max), n=3.

4.1.2 VAT-1 is dispensable for cell proliferation and does not mediate NCA's anti-proliferative activity

To gain further insights into the function and role of VAT-1 especially in the context of cell migration, a knockout cell line in HeLa cells was generated using the CRISPR/Cas9 technique. Successful deletion of VAT-1 was confirmed by Western blotting (**Figure 13-A**) and whole proteome liquid chromatography-mass spectrometry/mass spectrometry (LC-MS/MS) analysis (**Figure 13-B,C**) conducted by Josef Braun in the laboratory of Prof. Stephan Sieber (TU Munich, Germany).

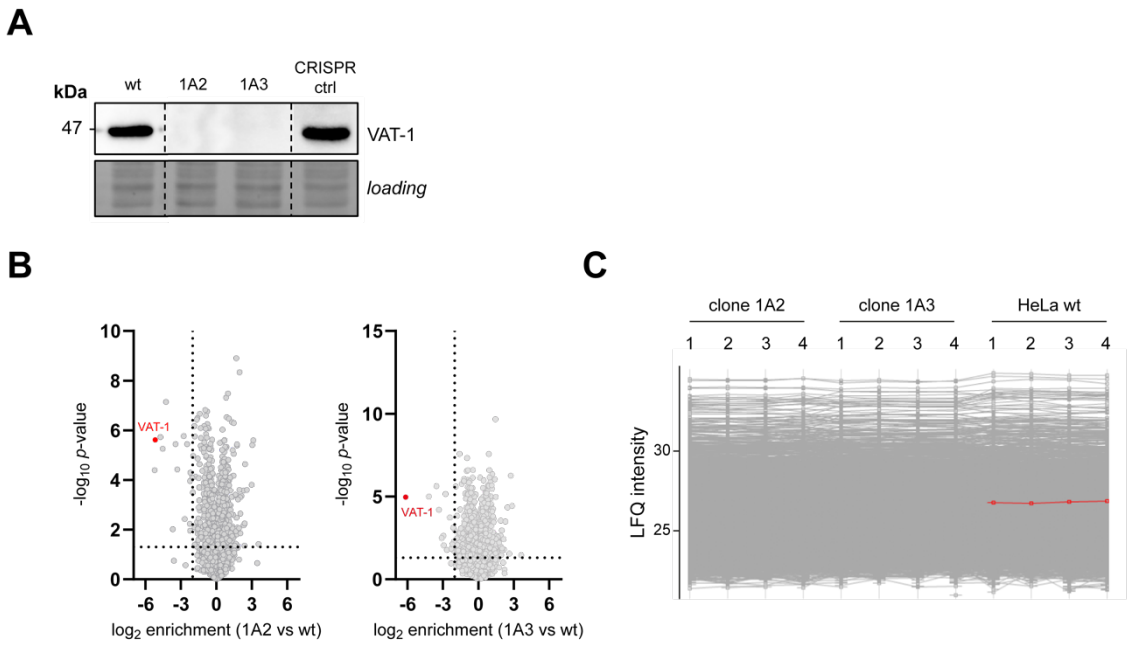

Figure 13 Validation of CRISPR/Cas9 mediated VAT-1 knockout in HeLa cells.
(A) Representative Western blot, (**B**, **C**) MS based whole proteome analysis conducted by Josef B. (TU Munich, Germany). Data presented (**B**) as volcano plot and (**C**) profile plot, (**A**) n=3, (**B,C**) n=4.

The functional characterization of the clones was started by assessing the proliferation rate of the two knockout lines 1A2 and 1A3 and the CRISPR control cells compared to HeLa wt cells by a crystal violet assay over 72 h (**Figure 14-A**). Both clones exhibited only a minor reduction in proliferation rate. However, the CRISPR control clone showed a significantly lower rate compared to HeLa wt cells. To support the hypothesis that VAT-1 is not the molecular target of NCA responsible for its antiproliferative effects, again a crystal violet assay over 72 h with NCA treatment ranging from 0.5 to 3.0 μM was conducted (**Figure 14-B**). The results clearly show that the antiproliferative activity of the

compound does not change upon VAT-1 knockout and confirms the hypothesis that there must be an additional target to explain the antiproliferative phenotype.

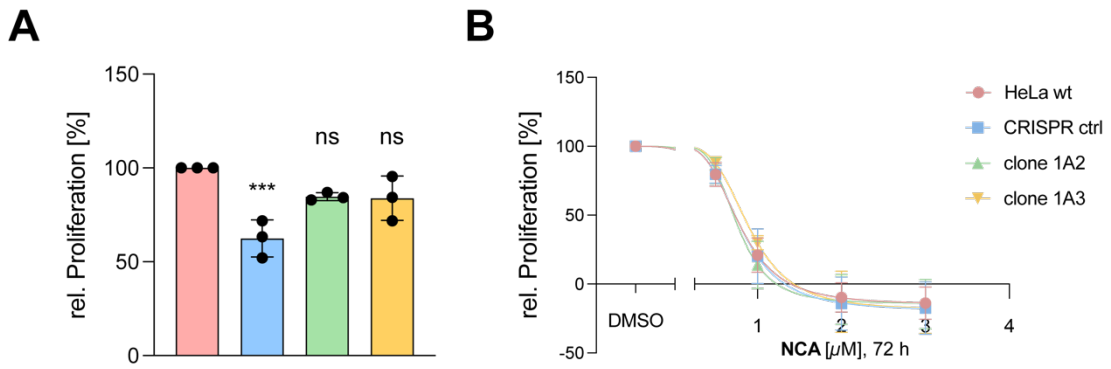

Figure 14 VAT-1 knockout neither effects cell proliferation nor NCA's antiproliferative activity.
Crystal violet assay over 72 h comparing proliferation of HeLa wt, CRISPR control, KO clone 1A2 and 1A3 (**A**) without and (**B**) with 0.5, 1.0, 2.0 and 3.0 μM NCA treatment. Data is presented as mean ± SD, n=3. (**A**) Statistical significance was analyzed by one-way ANOVA with Dunnett's posttest (ns ≙ not significant, ***P<0.001).

4.1.3 VAT-1 depletion desensitizes cells towards NCA's anti-migratory effects

In previous studies VAT-1 was identified as the molecular target of NCA that mediates its antimigratory activity [1]. To strengthen this hypothesis, the KO clones were subjected to two different migration assays. In a wound healing assay, the collective migration of cells was determined after applying a scratch in a confluent cell monolayer. Cells were treated with 1.0, 3.0 and 5.0 μM NCA or DMSO and stained with crystal violet after 18 h (**Figure 15-A**). Pictures were taken, and the size of the remaining gap analyzed by ImageJ. DMSO control was set to 100% and starvation control cells to 0%. The result shows clearly that the response of VAT-1 depleted cells towards NCA in terms of migration inhibition is significantly reduced compared to HeLa wt cells, whereas CRISPR control cells remain comparably sensitive. For analyzing single cell migration, an xCELLigence® impedance-based migration assay was performed. Cells were treated with 1.0, 3.0, 5.0 and 7.5 μM NCA or DMSO and migration through 8 μm pores in the direction of FCS as chemoattractant was monitored in real-time over 18 h (**Figure 15-B**). And again, VAT-1 knockout led to a reduced response compared to HeLa wt cells, obvious by a shift of the IC_{50} from 5.2 μM to 7.57 μM (1A2) and 7.61 μM (1A3). Taken together, those findings strongly underpin the hypothesis that VAT-1 is the antimigratory target of NCA.

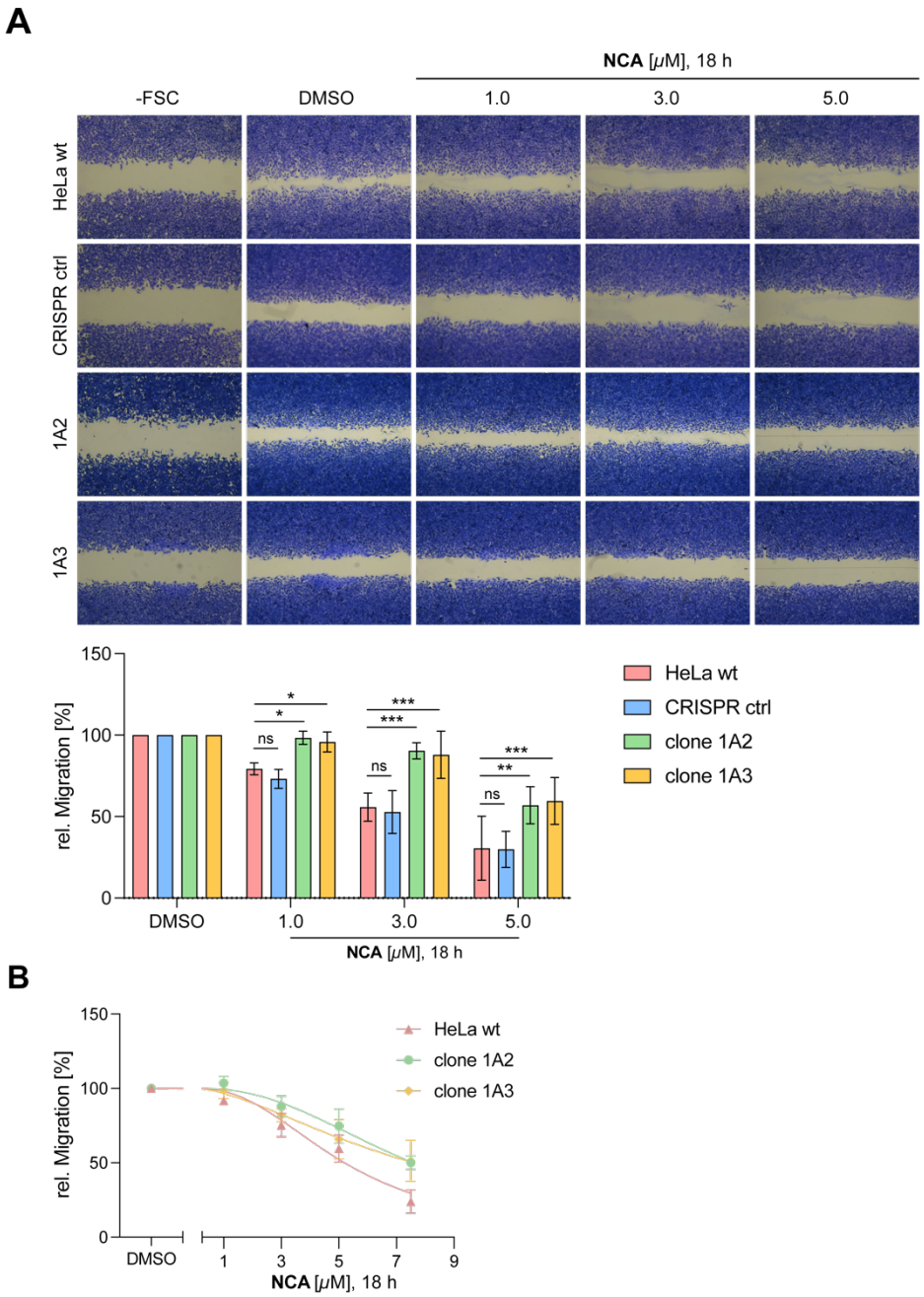

Figure 15 VAT-1 mediates NCA's antimigratory effects.
(**A**) Wound healing assay (**B**) xCELLigence® migration assay of (**A**) CRISPR control, (**A**,**B**) HeLa wt and VAT-1 KO 1A2 and 1A3 cell lines in response to (**A**,**B**) 1.0, 3.0, 5.0 and (**B**)7.5 μM NCA treatment over 18 h. DMSO served as positive, cells without FCS as negative control. (**A**) Representative images of crystal violet stained cells on the top panel. Analysis of migration rate on the bottom panel. Data are presented (**A**) in a bar graph (**B**) as nonlinear regressions of XY graphs as mean ± SD, n=3. (**A**) Statistical significance was analyzed by two-way ANOVA with Fisher's LSD test. (ns ≙ not significant, *P<0.5, **P<0.01, ***P<0.001).

4.1.4 VAT-1 influences cell spreading

Initially, cell spreading as simplified model for adhesion and motility processes was investigated upon loss of VAT-1. Cell spreading starts as a purely passive progress comparable to a drop that falls on a surface followed by active events including adhesive receptors, actin polymerization and myosin contraction. To determine an appropriate incubation time after which most of the cells started to spread, a pre-experiment was conducted in which HeLa wt and VAT-1 KO clone 1A3 were seeded in 96-well plates and phase contrast images were taken after 5, 15, 30, 60, 90 and 120 min (**Figure 16-A**). After 60 min approximately 80% of both cell populations showed a flattened spreading morphology (black arrows), so this time was chosen for further investigations. After 4 h pre-starvation, cells were seeded into fibronectin coated slides and after 60 min settling time fixed and stained with rhodamine-phalloidine to visualize the actin cytoskeleton (**Figure 16-B**). 30 cells per repetition were imaged and analyzed. Spreading morphology was assessed by ImageJ particle analysis, the spreading area and the shape factors circularity and roundness were quantified. VAT-1 knockout reduced the spreading area and led to an uneven spreading morphology characterized by a reduced circularity and roundness.

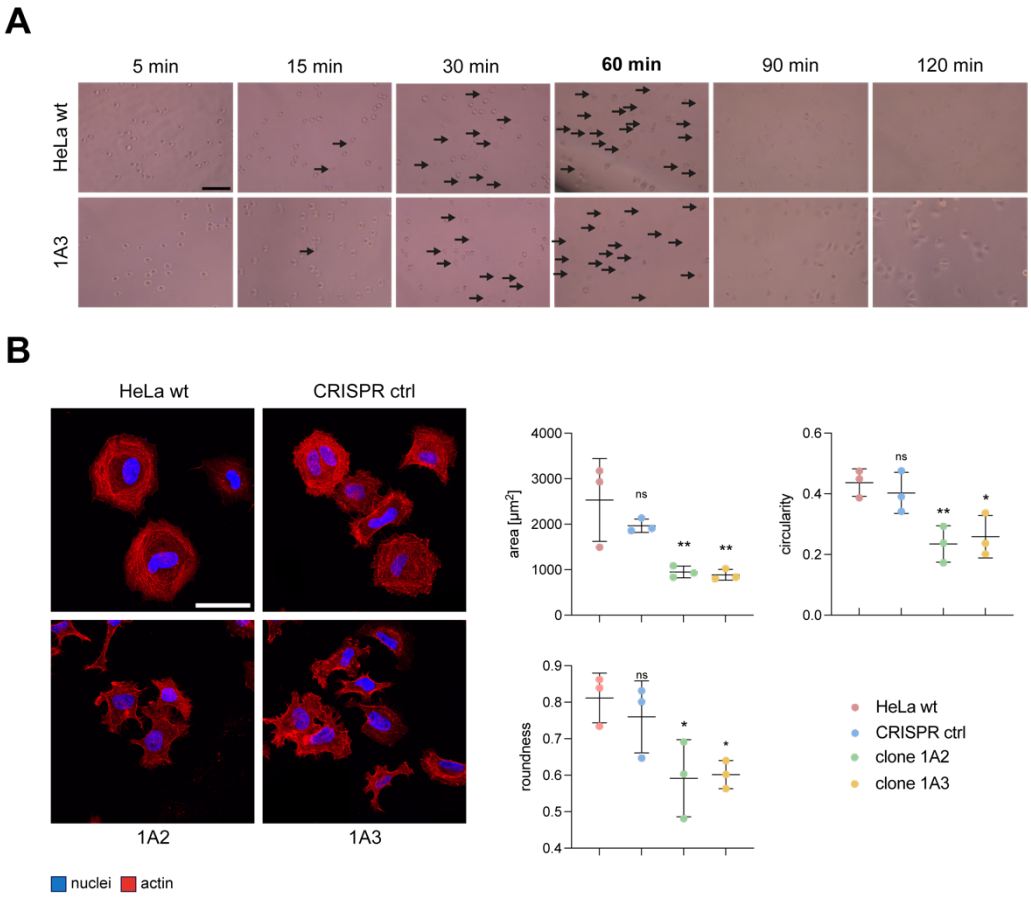

Figure 16 VAT-1 knockout reduces spreading area and alters spreading morphology.
(A) Preexperiment to determine a suitable settling time. HeLa wt and VAT-1 KO clone 1A3 were seeded in a 96-well plate, incubated for 5, 15, 30, 60, 90 and 120 min und phase contrast pictures were taken (scale bar 50 μm). Black arrows indicate spreaded cells, n=1. **(B)** Spreading assay, representative image of immunofluorescence staining of HeLa wt CRISPR control and VAT-1 KO 1A2 and 1A3 cells on the left panel. Nuclei shown in blue, actin in red (scale bar 25 μm). Brightness was adjusted to improve visibility. Analysis of spreading area and shape descriptors circularity and roundness by ImageJ on the right panel. Data are presented in a scatter plot as mean ± SD, n=3. Statistical significance was analyzed by one-way ANOVA with Dunnett's posttest (ns ≙ not significant, *P<0.5, **P<0.01).

4.1.5 VAT-1 is important for proper focal adhesion dynamics

In cell migration, the formation of so-called focal adhesions is of high importance, since those large protein complexes serve as a platform to mechanically and biochemically link cells to their surrounding environment (reviewed in [15]). They consist of numerous proteins, of which TLN1 is a prominent representative, found to be indispensable for the proper function of those foci. Since TLN1 was reported to interact with VAT-1 [1], we wondered whether focal adhesion dynamics are affected by the loss of VAT-1. During processes like adhesion and migration, focal adhesions undergo maturation, characterized by expansion and elongation. Analysis of focal adhesions was done by confocal imaging and subsequent image analysis according to Horzum *et al.* [66] (**Figure 17-A**). HeLa wt, VAT-1 KO and CRISPR control cells were pre-starved for 4 h and seeded on FN coated slides. After 90 min incubation, cells were fixed and stained for talin1 as focal adhesion marker (**Figure 17-B**). Evaluation of 30 cells per repetition revealed a decrease in focal adhesion number, area and perimeter. Shape factors of the focal adhesions like roundness, circularity, and aspect ratio, however, remained largely unchanged (data not shown). This indicates that VAT-1 depletion interferes with the proper maturation of focal adhesions.

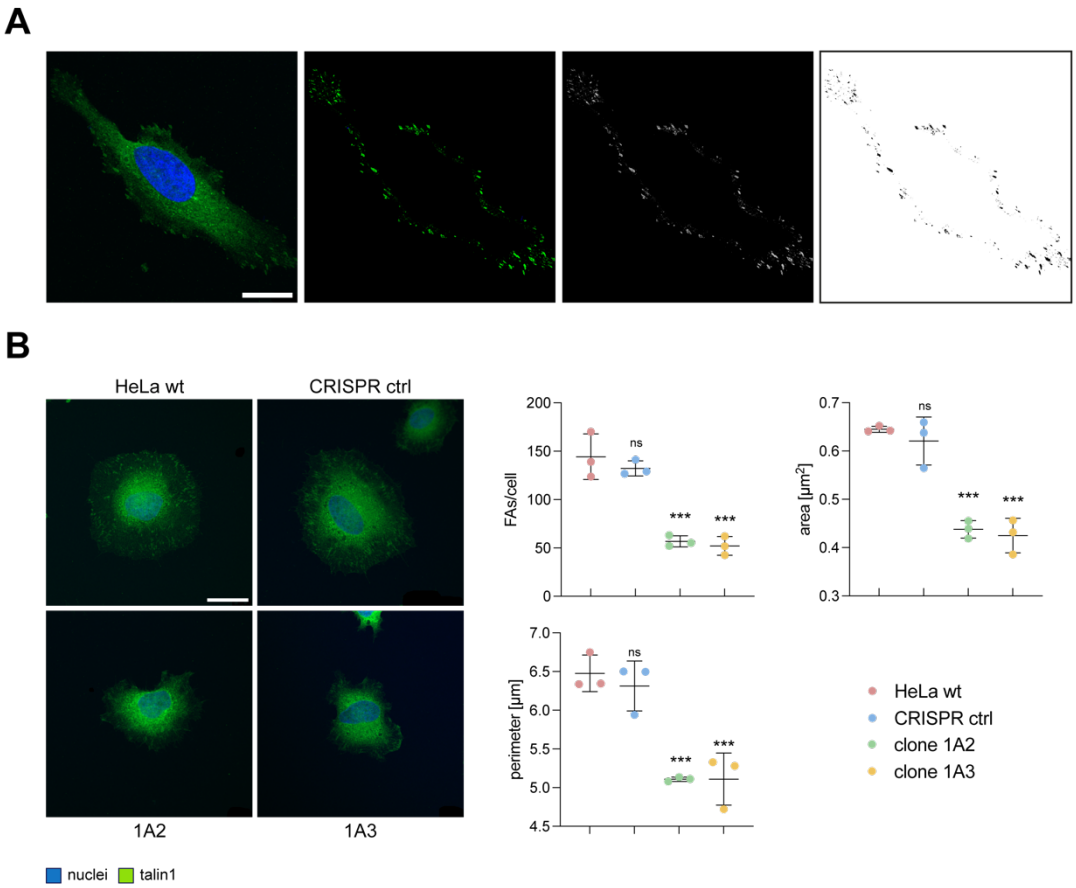

Figure 17 Focal adhesion dynamics are affected by the loss of VAT-1.
(A) Procedure for analyzing focal adhesions. Representative image of immunofluorescence staining of HeLa cells. Nuclei shown in blue, talin1 in green (scale bar 25 μm). Brightness was adjusted to improve visibility. ImageJ analysis: background was subtracted, local contrast enhanced (image **A**-2), transformed into a grey-scale image (image **A**-3), thresholded and particle analyzed (image **A**-4). (**B**) Representative image of immunofluorescence staining of HeLa wt, CRISPR control and VAT-1 KO 1A2 and 1A3 cells on the left panel. Nuclei shown in blue, talin1 in green (scale bar 25 μm). Brightness was adjusted to improve visibility. Analysis of focal adhesion number, area, and perimeter by ImageJ on the right panel. Data are presented in a scatter plot as mean ± SD, n=3. Statistical significance was analyzed by one-way ANOVA with Dunnett's posttest (ns ≙ not significant, ***P<0.001).

4.1.6 VAT-1 seems not to influence integrin β1 activation

Clustering and activation of integrins is mainly facilitated by talin1. To assess the activation status of integrin β1 in the VAT-1 KO compared to HeLa wt and CRISPR control cells, a confocal based assay was performed (**Figure 18**). For this, an antibody raised against an epitope that is only exhibited in the unbend, activated form of integrin β1 was used and at the same time the total expression of integrin β1 was determined by a respective antibody staining for normalization purpose. All cell lines were starved for 4 h, seeded onto FN coated slides, incubated for 2 h and finally fixed and stained. Integrin signal intensities were analyzed by ImageJ. After normalization, a significant reduction in integrin β1 activation was observed for the KO clones, however, the CRISPR control clone showed the same behavior, suggesting that it is an effect of the CRISPR process rather than a direct impact of the loss of VAT-1. Still, the morphology and distribution of active integrin β1 seems to be altered in the KO clones, which need to be further investigated.

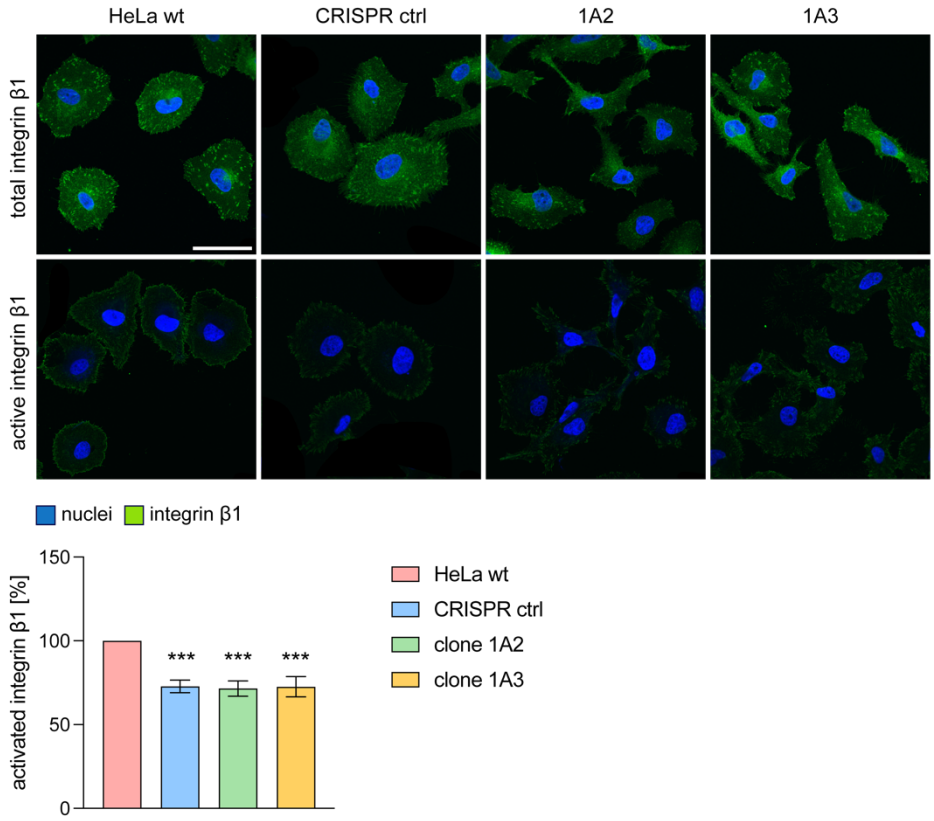

Figure 18 VAT-1 knockout reduces integrin β1 activation, but CRISPR control cells also show this characteristic. Integrin activation assay, representative images of immunofluorescence staining of HeLa wt, CRISPR control and VAT-1 KO 1A2 and 1A3 cells on the top panel. Nuclei shown in blue, total integrin β1 (top row) or active integrin β1 (bottom row) in green (scale bar 50 μm). Brightness was adjusted to improve visibility. Intensities of active integrin β1 were analyzed, corrected with the total expression and data are presented on the bottom panel in a bar graph as mean ± SD, n=3. Statistical significance was analyzed by one-way ANOVA with Dunnett's posttest (ns ≙ not significant, ***P<0.001).

4.1.7 Part I: Summary

We could show that VAT-1 localizes at mitochondria and membrane structures in a centrifugation based subcellular fractionation and were able to confirm the mitochondrial localization by an immunostaining. Next, VAT-1 knockout models in HeLa cells were generated and characterized in the context of cell proliferation and migration with a special focus on manipulation of those cell processes by applying our natural compound NCA. Here, it could be demonstrated that VAT-1 is not the responsible target for the antiproliferative phenotype of this compound and convincingly proved that it is strongly involved in its antimigratory activity, by inhibiting both single and collective cell migration. Furthermore, we assessed the effect of VAT-1 deletion on cell spreading, where we found this process to be disturbed in our knockout cell lines compared to HeLa wt cells. Because VAT-1 was recently shown to interact with TLN1 [1], we investigated focal adhesion dynamics and found an aberrant maturation of them in our KO cells. Although integrin β1 activation also seemed to be reduced, a direct link to our protein of interest could not be drawn, because CRISPR control cells also showed this phenotype.

4.2 Part II: The effects of neocarzilin A on mitochondrial functions, apoptosis induction and ER stress

Inspired by preliminary experiments conducted by Weiting C. that suggested an intensive perturbation of proper mitochondrial functions by our natural compound in form of a fragmented mitochondrial network, reduced oxygen consumption rate, increased ROS generation and diminished ATP production (**Figure S1**), in the second part of these studies, we aimed to shed further light on this phenotype and reveal the responsible target. However, we opted shorter incubation times (3 and 6 h) in higher concentrations (1-20 μM), which are considered subacute in the study of effects on mitochondrial, to examine if the compound directly affects these organelles.

4.2.1 NCA causes mitochondrial network fragmentation by inducing OPA1 splicing

Mitochondria are highly dynamic organelles, undergoing balanced fission and fusion events to control their number, positioning, and proper function. We used the ImageJ MiNA (= mitochondrial network analysis) plugin to assess changes in mitochondrial dynamics. HeLa cells were treated with 3.0, 5.0 and 10.0 μM NCA or DMSO for 3 and 6 h and subsequently stained for the heat shock protein Hsp60 as mitochondrial marker (**Figure 19**). 10 cells per condition and repetition were analyzed in three independent experiments and the mitochondrial footprint, mean branch length, mean branches per network and mean summed branches length quantified by ImageJ. While DMSO control cells exhibited long branched mitochondrial networks, treatment with NCA led to a fragmentation shown by a significant reduction of all analyzed network characteristics. This was accompanied by a clustering of mitochondria in the perinuclear region. The effects were already detectable after 3 h at high concentrations (**Figure S2**), getting even more pronounced after 6 h. Of note, the microtubule network remained unaffected by treatment with the compound under the above-mentioned conditions (**Figure S3**). The main players of mitochondrial fission and fusion, Mfn1, dynamin 1 like (Drp1) and Opa1, members of the dynamin GTPase protein family, were assessed by immunoblotting after 6 h treatment with NCA compared to DMSO treated HeLa cells (**Figure 20**). Interestingly, Mfn1 and Drp1 levels were not affected, while Opa1 splicing from the long

l- to the short s-form was significantly induced upon treatment, most likely accounting for the observed fragmentation phenotype.

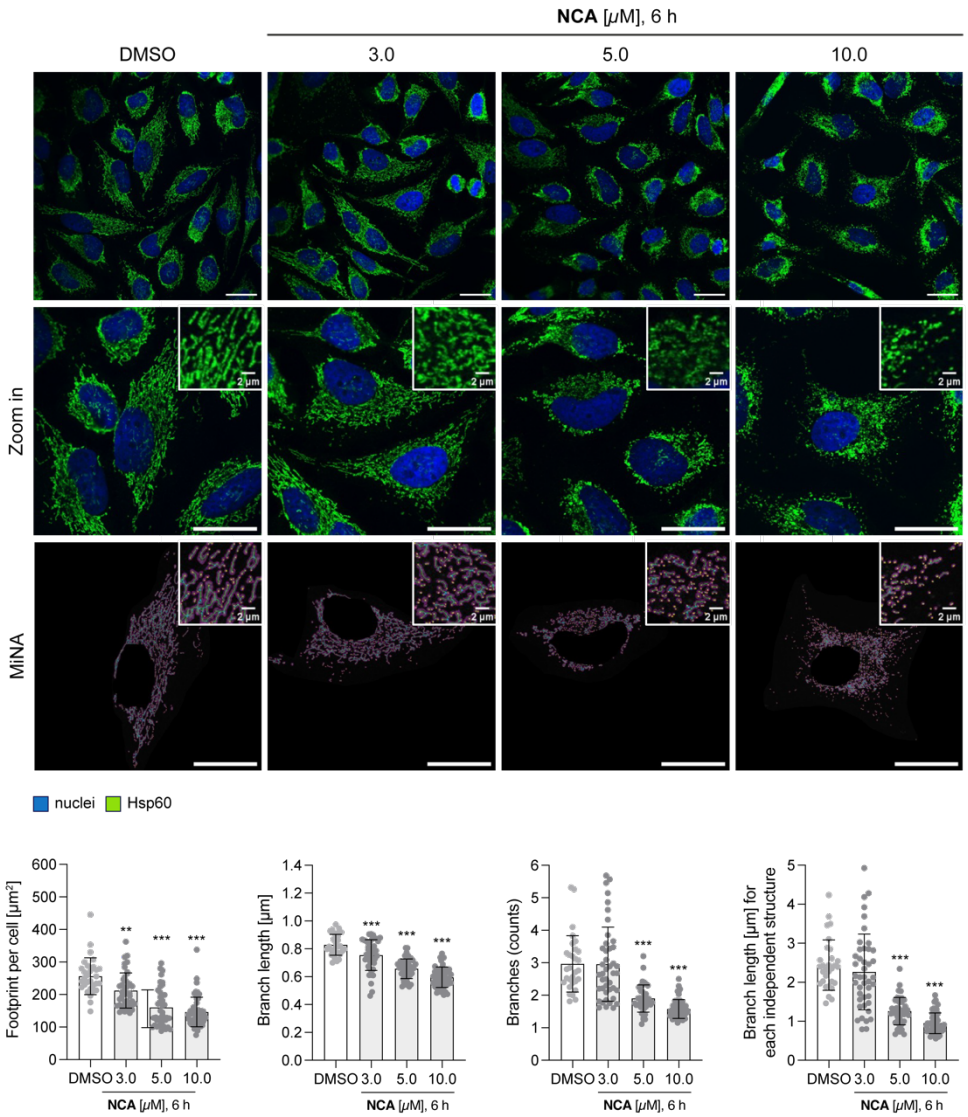

Figure 19 NCA treatment favours mitochondrial network fission and clustering of mitochondria around the nucleus.
Analysis of mitochondrial dynamics in HeLa cells upon NCA treatment at the indicated concentration for 6 h conducted by Elena C.. Representative images of immunofluorescence staining of HeLa wt cells on the top panel, nuclei shown in blue, Hsp60 in green (scale bar 25 μm). Brightness was adjusted to improve visibility. Bottom row shows MiNA analysis, purple area represents mitochondrial footprint, green lines mitochondrial length, blue dots connection sites and yellow dots the end of network structures. Data are presented on the bottom panel in a bar graph as mean ± SD, n=3. Statistical significance was analyzed by one-way ANOVA with Dunnett's posttest. (**P<0.01, ***P<0.001).

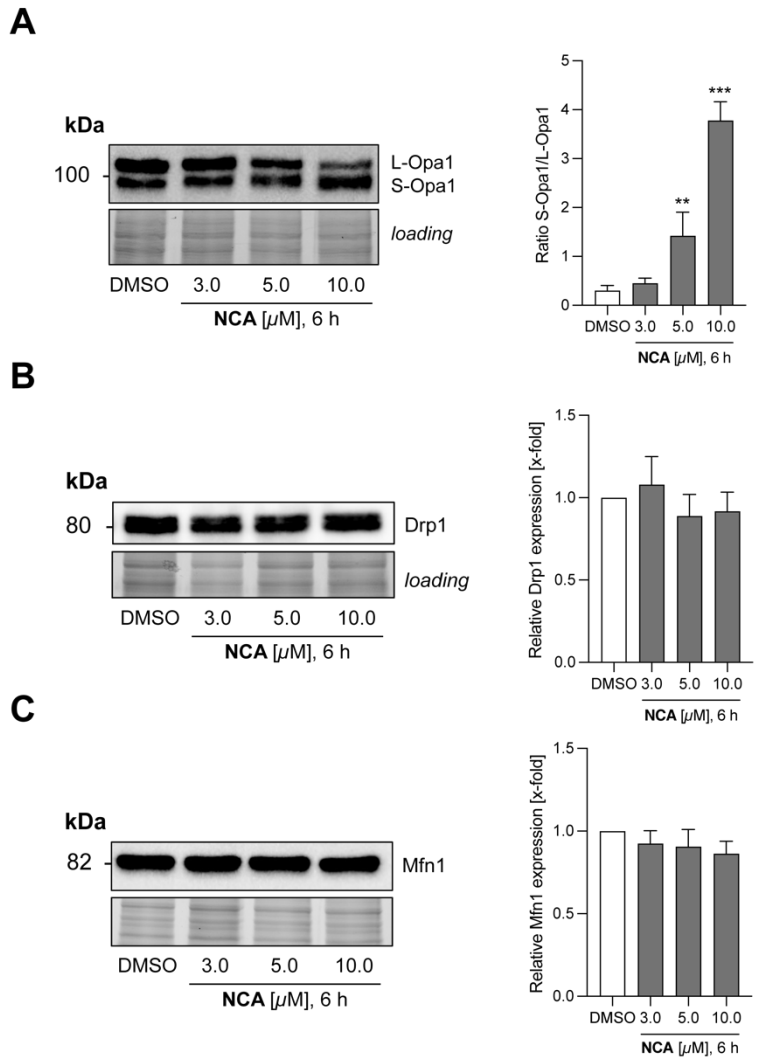

Figure 20 Enhanced Opa1 splicing accounts for NCAs effects on mitochondrial network dynamics.
Main regulators of mitochondrial fission and fusion were analyzed by immunoblotting upon NCA treatment at the indicated concentrations for 6 h conducted by Elena C.. Representative Western blots of (**A**) Opa1, (**B**) Drp1 and (**C**) Mfn1 on the left panel. Normalized expression (**B**,**C**) and ratio of S- over L-Opa1 (**A**) presented in a bar graph on the right panel as mean ± SD, n=3. Statistical significance was analyzed by one-way ANOVA with Dunnett's posttest. (**P<0.01**,** ***P<0.001).

4.2.2 NCA changes mitochondrial ultrastructure

After detecting alteration in mitochondrial dynamics upon NCA treatment, the question raised whether the compound also affects mitochondrial ultrastructure. To investigate this, transmission electron microscopy (TEM) was employed. HeLa cells were treated with 5.0 μM NCA or DMSO and analyzed by Carola Eberhagen in the laboratory of Prof. Hans Zischka (Helmholtz Centre Munich, Germany) (**Figure 21-A**). Mitochondrial morphology of 50 mitochondria in each of the three independent experiments was evaluated by ImageJ. Mean grey value representing the mitochondrial matrix density, size, and cristae density (cristae/size) as well as the shape factors roundness and aspect ratio were calculated (**Figure 21-B**). The results show that upon treatment with the compound, the mitochondrial size increases, whereas matrix and cristae density significantly decrease. In addition, the shape of the mitochondria changed from an elongated to a rounded shape, reflected in a significantly increased circularity and reduced aspect ratio. Taken together, those results indicate that NCA induces mitochondrial swelling through a so far unknown mechanism.

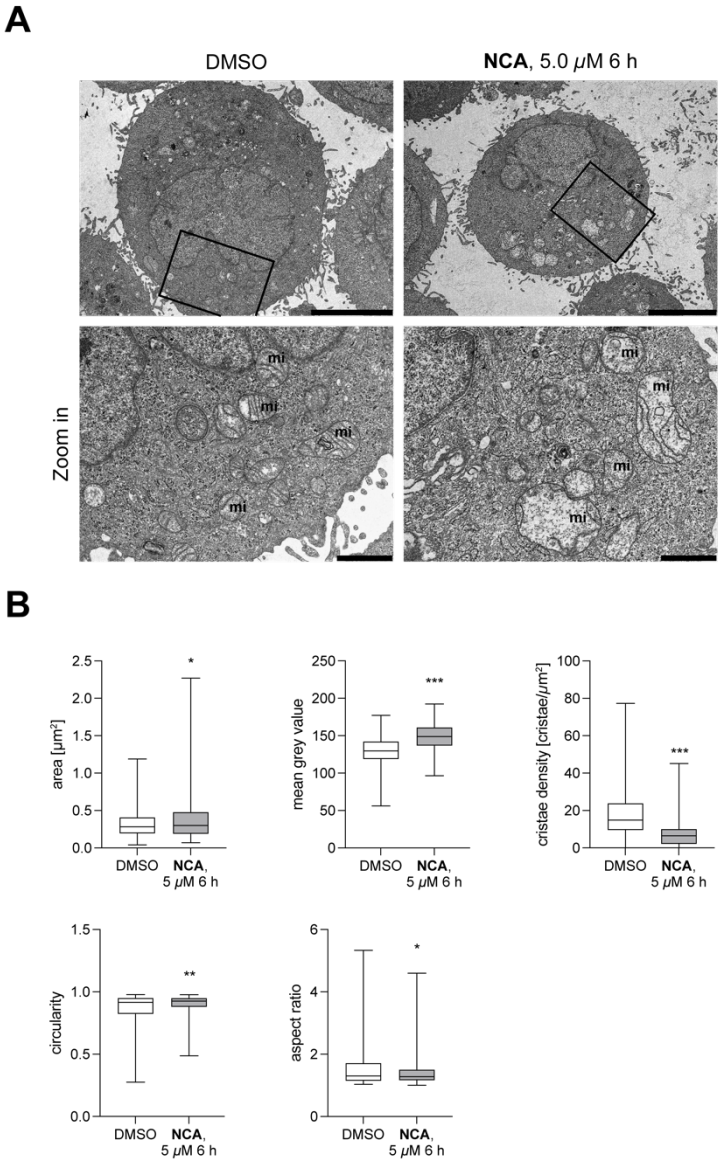

Figure 21 Transmission electron imaging of NCA treated cells reveals changes in mitochondrial ultrastructure. Mitochondrial ultrastructure analysis of HeLa cells treated with 5 μM NCA for 6 h by transmission electron microscopy. (**A**) Representative TEM images of NCA and DMSO treated cells on the top panel (scale bar top row 5000 nm, bottom row 1000 nm, mi = mitochondria). (**B**) Analysis of 50 mitochondria per repetition of mitochondrial size, mean grey value, cristae density and shape factors circularity and aspect ratio on the bottom panel. Data are presented as box and whiskers (min to max), n=3. Statistical significance was analyzed by two-tailed unpaired Student's t-test. (*P<0.5, **P<0.01**,** ***P<0.001).

4.2.3 NCA treatment causes loss of mitochondrial membrane potential and triggers mitochondrial superoxide generation through calcium overload

The functionality of the respiratory chain is strongly dependent on the integrity of the mitochondrial membranes and the membrane potential at the inner mitochondrial membrane. Therefore, in the next step, the mitochondrial membrane potential (ΔΨm) was analyzed using the lipophilic cationic JC-1 dye. HeLa cells were treated with NCA ranging from 3.0 - 15.0 μM or DMSO for 6 h and JC-1 fluorescence was analyzed by flow cytometry (**Figure 22-A**). The uncoupler carbonylcyanid-m-chlorphenylhydrazon (CCCP) was used as positive and DMSO as negative control for proper gating. NCA induced a dose-dependent loss of ΔΨm, which was significant for 10.0 and 15.0 μM almost reaching the same intensity as CCCP. One possible explanation for the mitochondrial swelling, loss of cristae and dissipation of the ΔΨm observed so far could be a mitochondrial overload of calcium since those organelles play an important role in buffering calcium ions. So next, NCA treatment was combined with application of the calcium chelator BAPTA and the ΔΨm again assessed via flow cytometry (**Figure 22-B**). Remarkably, the effect of the compound on the potential could be completely rescued by this, implicating a crucial role of calcium in mediating NCA's effects on mitochondria. Therefore, mitochondrial calcium levels were measured by a Rhod2 AM based flow cytometry assay (**Figure 22-C**). HeLa cells were treated with NCA concentrations ranging from 3.0 to 20.0 μM for 6 h and 10 μM for 2, 4 and 6 h. A clear, dose- and time-dependent significant increase in mitochondrial calcium could be shown.

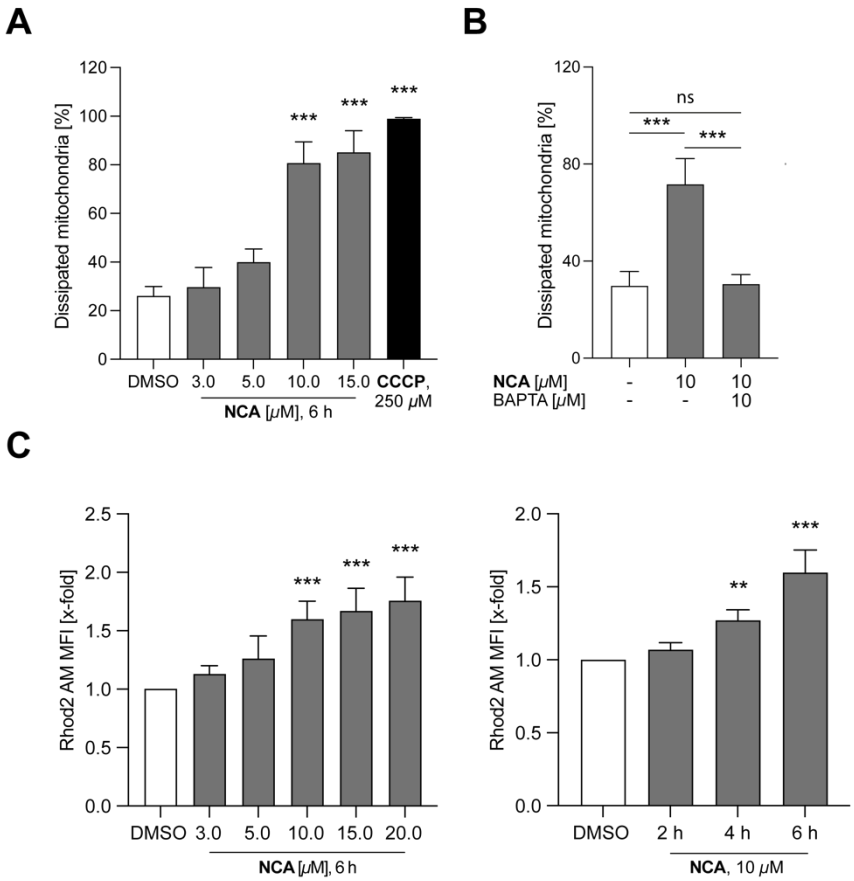

Figure 22 Mitochondrial membrane potential breaks down upon NCA treatment mediated through extensive calcium influx.
(**A**,**B**) Mitochondrial membrane potential analysis with JC-1, (**C**) mitochondrial calcium analysis with Rhod2 AM by flow cytometry. HeLa cells were treated with NCA (**A**,**C**) or NCA + BAPTA (**B**) as indicated for (**A**,**B**,**C** left panel) 6 h or (**C**, right panel) 2, 4 and 6 h. (**A**) CCCP served as positive control. Data are presented in bar graphs as mean ± SD, n=3. Statistical significance was analyzed by one-way ANOVA with Dunnett's posttest (ns ≙ not significant, **P<0.01, ***P<0.001).

Mitochondria are the main source of reactive oxygen species, since electrons that leak out of the respiratory chain can be transferred to oxygen to form unstable superoxide radicals that can react further to other species.

The findings described above led to the assumption that the natural compound causes a disruption of the electron transfer chain and thus could lead to changes in mitochondrial ROS levels. For these reasons, mitochondrial superoxide levels upon NCA treatment were investigated using the MitoSOX^{TM} dye. Cells were treated with NCA in the same concentration range as for the JC-1 $\Delta\Psi m$ assay and analyzed after 3 and 6 h by live cell imaging (**Figure 23-A**) and after 6 h by flow cytometry (**Figure 23-B**), where 100 μM antimycin A served as positive control.

NCA induced a significant increase in superoxide generation already after 3 h at the highest concentration (**A**) and dose-dependently (**A**, **B**) after 6 h. The induction was even more pronounced than in the antimycin treated cells.

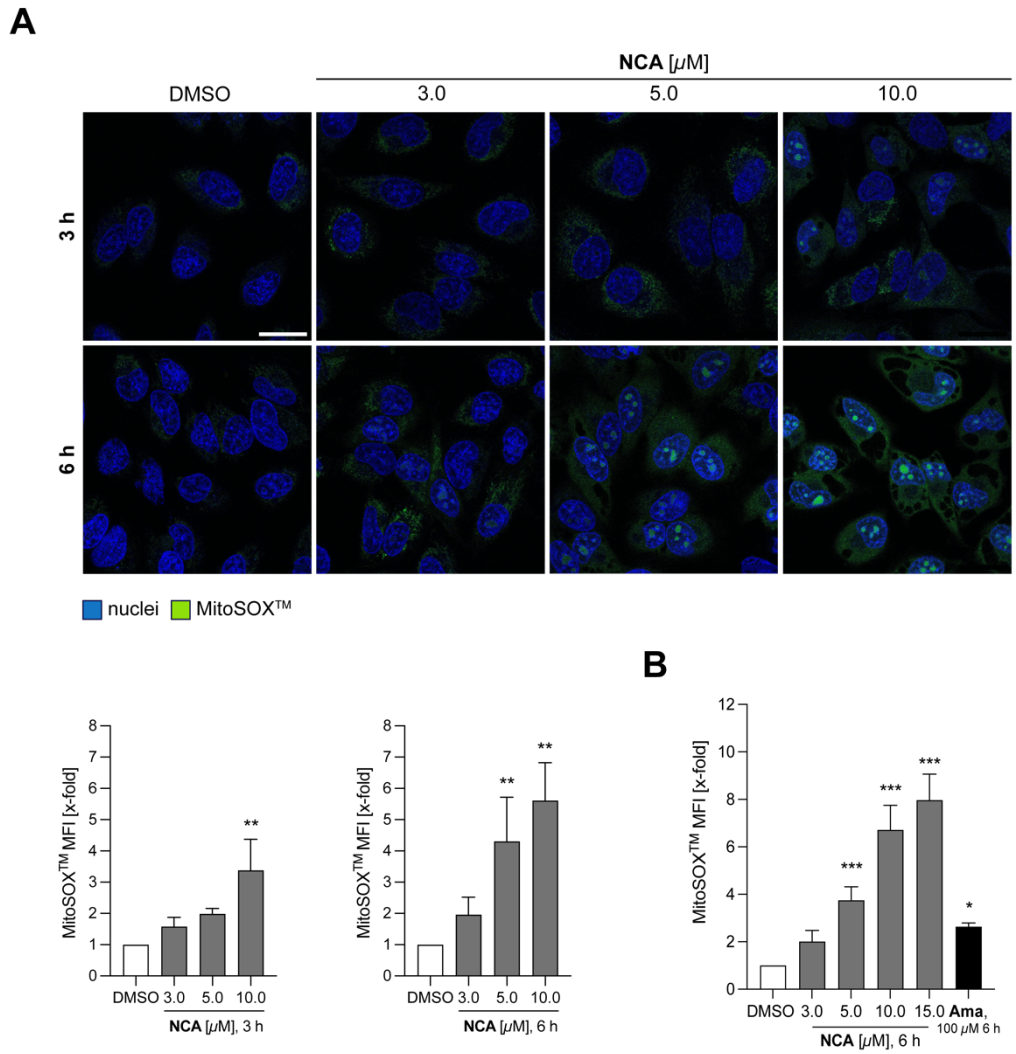

Figure 23 NCA triggers the generation of mitochondrial superoxide.
(**A**,**B**) Mitochondrial superoxide generation analyzed in HeLa cells treated with NCA as indicated for (**A** top row and left graph in left panel) 3 h or (**A** bottom row and right graph in left panel,**B**) 6 h by (**A**) live cell imaging conducted by Elena C. and (**B**) flow cytometry, where antimycin A served as positive control. (**A**) Representative images of HeLa cells, with nuclei in blue and MitoSOX™ in green (scale bar 25 μm). Brightness was adjusted to improve visibility. MitoSOX™ intensity was determined. (**B**) MitoSOX™ mean fluorescence intensity was recorded. Data are presented as mean ± SD, n=3. Statistical significance was analyzed by one-way ANOVA with Dunnett's posttest. (*P<0.5, **P<0.01, ***P<0.001).

4.2.4 Cellular respiration is disturbed by NCA

Since most of the oxygen utilized by cells is consumed by mitochondria, the oxygen consumption rate (OCR) was examined in a plate reader assay based on an oxygen quenchable dye (**Figure 24-A**). HeLa cells were treated with 3.0, 5.0 and 10.0 μM NCA or DMSO and OCR, represented by a decreasing MitoXpress^{TM} fluorescence monitored over 6 h. 1.0 μM antimycin A served as positive control. NCA led to a significantly lowered OCR, which was calculated by the slope of the obtained fluorescence curves. With this first hint that the compound affects the respiratory chain in hands, electron transfer chain function was in-depth investigated by applying high-resolution respirometry with a Oroboros instrument in the laboratory of Prof. Hans Zischka (Helmholtz Centre Munich, Germany) and the kind assistance of Judith Sailer (TU Munich, Munich, Germany) (**Figure 24-B**). Initially, 6 h 5 μM treated HeLa cells were analyzed against DMSO control cells following the SUIT-0078O2 ce-pce D025 protocol. Here, a strong induction of proton leak and a reduced complex I and combined complex I and II respiration could be detected (**Figure 24-C**). For better comparability, the corresponding flux control efficiencies were calculated (**Figure 24-D**). In a following series of experiments, NCA was titrated directly into the measuring chamber. Here, especially a striking rise in the LEAK respiration state could be shown, which was even directly inducible by applying high doses of NCA (**Figure 24-E**).

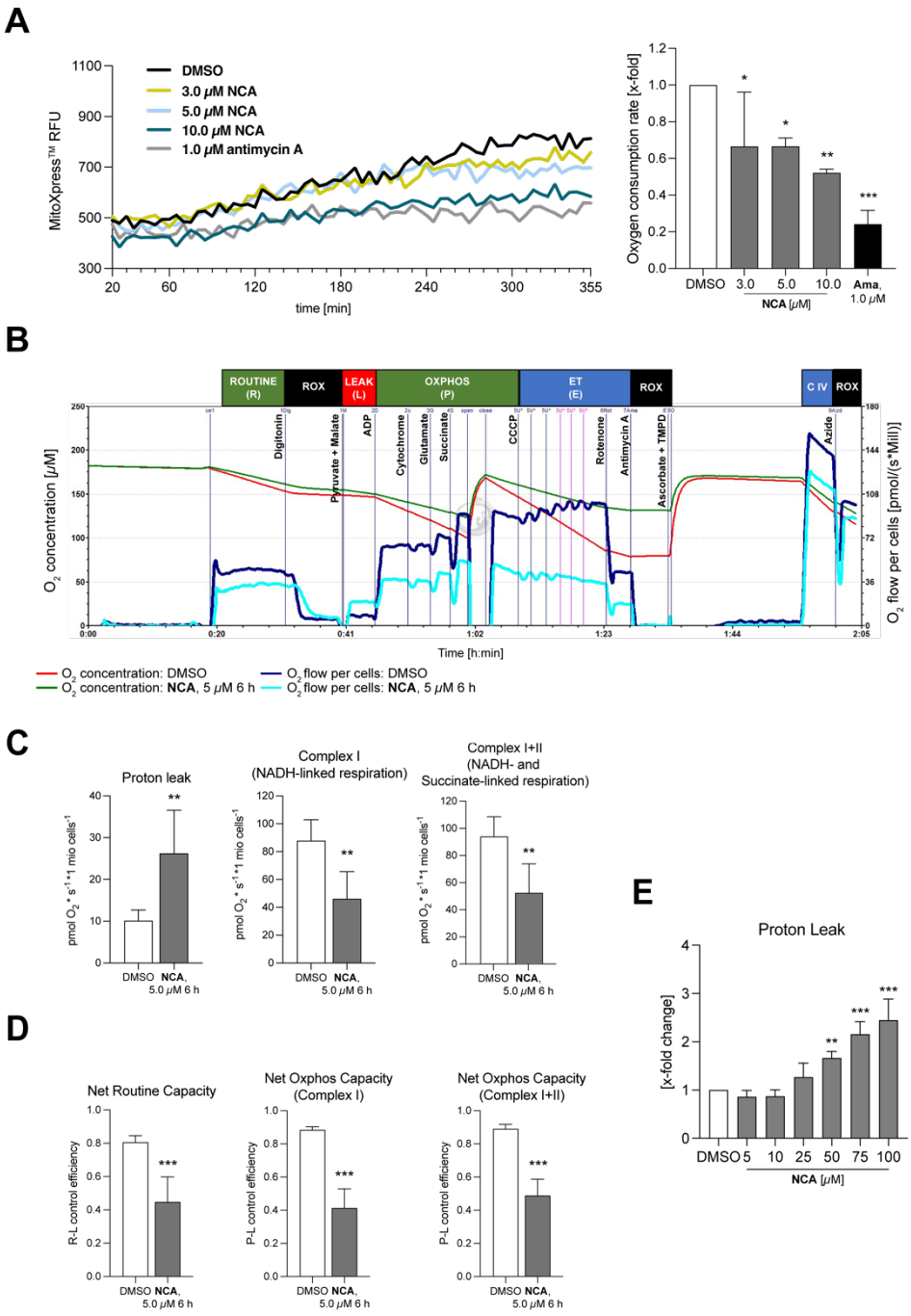

Figure 24 NCA affects cellular respiration, increases proton leak, and impairs complex I and II function.
(**A**) Oxygen consumption rate (OCR) assay of HeLa wt cells treated with NCA as indicated conducted by Elena C.. Antimycin A served as positive control. Fluorescence (Ex 380 nm/Em 670 nm) was recorded over 6 h. Representative curves shown in the left panel. OCR was calculated from the slope of the curves and is presented on the right panel in a bar graph as mean ± SD, n=3. (**B**,**C**,**D**,**E**) High resolution respirometry using Oroboros Oxygraph-2k. HeLa cells were (**B**,**C**,**D**) treated with 5.0 μM NCA for 6 h or (**E**) directly stimulated at the indicated concentrations. (**B**) Representative curves shown. Data are presented in bar graphs as mean ± SD, (**C**,**D**) n=5, (**E**) n=4. Statistical significance was analyzed by (**A**,**E**) one-way ANOVA with Dunnett's posttest or (**C**,**D**) by two-tailed unpaired Student's t-test (*P<0.5, **P<0.01, ***P<0.001).

To confirm those findings, an isolated complex I enzymatic assay based on the conversion of decylubiquinone to decylubiquinol and the resulting decolorization of the dye 2,6-dichlorophenolindophenol (DCIP) was established (**Figure 25-A**). HeLa cells were treated for 6 h with 10 μM NCA and DMSO, respectively, and mitochondria were enriched as described by de Wit and Sluiter [65]. The enzyme activity was recorded over 15 min. NCA treated cells exhibited a significantly reduced complex I activity supporting the data obtained from the Oroboros experiments.
The terminal step of the respiratory chain is the oxidative phosphorylation of ADP to ATP. Since a strong perturbation of the electron transfer chain (ETC) could be shown previously, it was reasonable to assume that NCA also interferes with the ATP synthesis. Therefore, a luminescence-based plate reader assay was performed. In preliminary experiments, no change in ATP levels upon treatment with the natural compound could be detected (**Figure S4**). One explanation for this surprising result was that according to Otto Warburg many cell lines restore their ATP pool by the so-called aerobic glycolysis even in the presence of oxygen rather than by oxidative phosphorylation [34]. To investigate the proportion that is facilitated by the OXPHOS, the assay was repeated in the presence of the glycolysis inhibitor 2-deoxyglucose (**Figure 25-B**). And indeed, with this additional modification, a significant, dose-dependent impairment of ATP synthesis could be demonstrated.

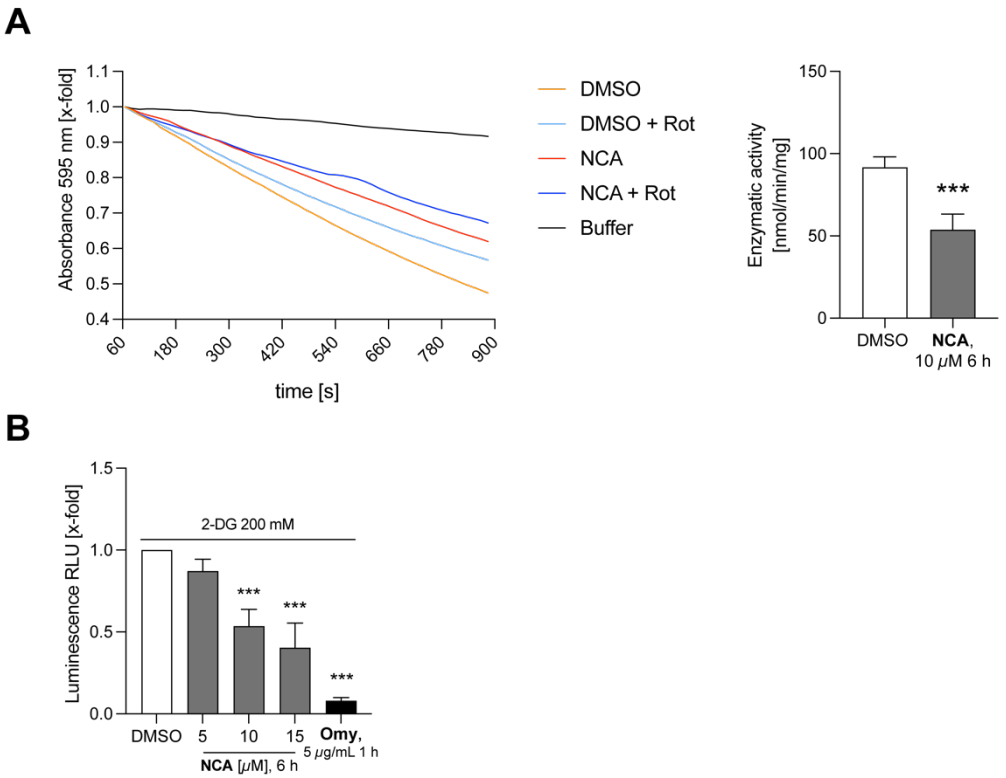

Figure 25 NCA inhibits complex I enzymatic activity and reduces ATP synthesis.
(**A**) Complex I assay in HeLa cells treated with 10 μM NCA for 6 h. Mitochondria were enriched and enzymatic activity measured by indirect reduction of DCIP absorbance at 595 nm over 15 min. Exemplary curves shown on the left panel. Complex I activity was calculated from the slope of the curves. (**B**) CellTiter-Glo ATP assay of HeLa cells treated with NCA as indicated combined with glycolysis inhibition by 200 mM 2-DG for 6 h. Oligomycin served as positive control. ATP levels were determined by analyzing luminescence intensity. (**A** right panel,**B**) Data are presented in a bar graph as mean ± SD, (**A**) n=4, (**B**) n=3. Statistical significance was analyzed by (**A**) two-tailed unpaired Student's t-test or (**B**) one-way ANOVA with Dunnett's posttest (***P<0.001).

4.2.5 NCA activates the caspase 8/Bid/cytochrome c axis of the extrinsic apoptosis pathway

Since mitochondria play a crucial role in mediating programmed cell death processes and striking disturbance of proper functions of those organelles were detected so far, it was suspected that NCA could lead to apoptotic cell death. That's why several characteristics of apoptosis were examined upon stimulation with the natural compound. First, expression of caspase 3,8 and 9, BH3 only protein Bid and poly(ADP-Ribose) polymerase (PARP) were analyzed by immunoblotting **(Figure 26-A,B,C,E,F**). Cells were treated with 2.5, 5.0 and 7.5 μM NCA or DMSO for 24 h. Normalizations of the blots revealed induction of caspase cleavage as evidenced by a decrease in procaspases 3 and 9 levels and an elevated cleaved to total expression ratio of caspase 8, as well as increased cleavage of Bid and PARP. In agreement with the caspase 8/Bid axis, in a subcellular fractionation after 12 h 7.5 μM NCA treatment cytochrome c release from mitochondrial to the cytosol fraction could be shown (**Figure 26-D**). Lastly, in a flow cytometry based propidium iodide staining assay according to Nicoletti *et al.* [64] DNA fragmentation as one of the terminal processes in apoptosis could be demonstrated (**Figure 26-G**). Taken together, it can be concluded that NCA triggers apoptosis via the caspase 8/Bid/cytochrome c axis of the extrinsic pathway.

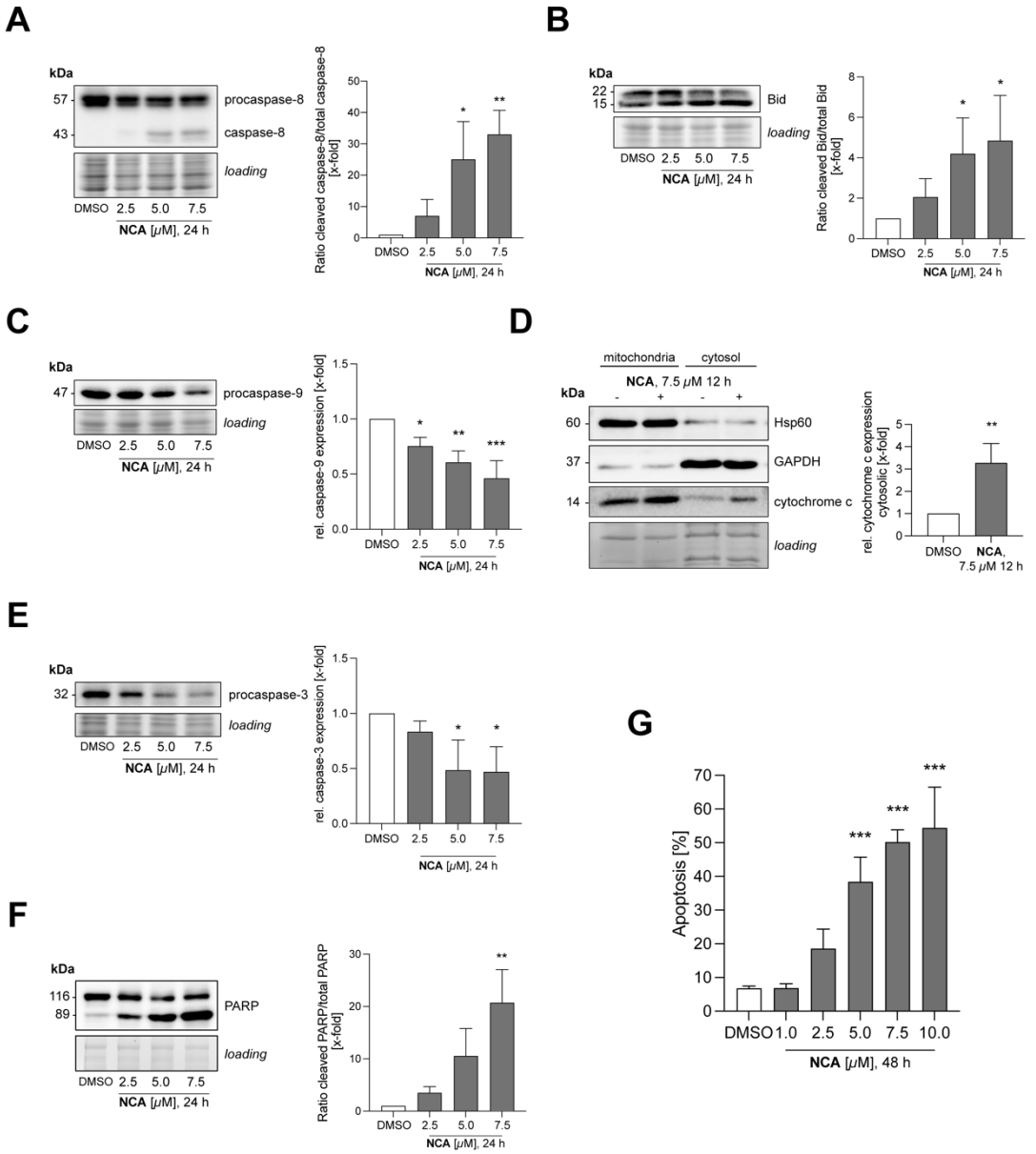

Figure 26 NCA activates extrinsic pathway of apoptosis.
(**A**,**B**,**C**,**D**,**E**,**F**) Analysis of apoptosis markers by immunoblotting . HeLa cells were treated with (**A**,**B**,**C**,**E**,**F**) 2.5, 5.0 and (**A**,**B**,**C**,**D**,**E**,**F**) 7.5 μM NCA for (**A**,**B**,**C**,**E**,**F**) 24 h or (**D**) 12 h and ratio of cleaved to total (**A**) caspase 8, (**B**) Bid, (**F**) PARP or relative expression of (**C**) caspase 9 and (**E**) caspase 3 were determined. (**D**) Cytochrome c release was analyzed by subcellular fractionation and immunoblotting in mitochondrial and cytosolic fractions. (**G**) DNA fragmentation was analyzed by propidium iodide staining and flow cytometry. Data are presented in bar graphs as mean ± SD, n=3. Statistical significance was analyzed by (**A**,**B**,**C**,**E**,**F**,**G**) one-way ANOVA with Dunnett's posttest or (**D**) two-tailed unpaired Student's t-test (*P<0.5, **P<0.01, ***P<0.001).

4.2.6 NCA induces cytoplasmic vacuolization

During routine screening of NCA treated cells, an interesting observation was made. The compound seemed to induce a massive cytoplasmic vacuolization, which was already visible under a light microscope (**Figure 27-A**, white arrows). In order to investigate this unusual phenomenon in more detail, TEM images NCA treated HeLa cells (6 h 10 μM) were taken and compared with DMSO treated cells (**Figure 27-B**). Again, too, the distinctive vacuoles were clearly visible and, interestingly, appeared to bud off from the nuclear membrane (red arrow). This insight led to the assumption that the vacuoles are ER derived. To support this hypothesis, a plasmid coding for the fluorescent dye DsRed2 coupled to an ER localization and retention signal was expressed in HeLa cells before treating them with 10 μM NCA for 6 h followed by a live-cell imaging (**Figure 27-D**). This experiment revealed that the vacuoles must be of ER origin, recognizable by the coincidence of the vacuoles shown in the bright field channel and the ER dye signal. Since previously a calcium overload could be identified as possible trigger for the mitochondrial disturbance, it was speculated that calcium from the ER leaks into the cytosol, which then gets buffered by mitochondria. That's why a flow cytometry based cytosolic calcium assay was carried out, in which HeLa cells were treated with 10 μM NCA and calcium levels measured over 1 h (**Figure 27-C**). Normalization to respective DMSO control values showed clearly elevated cytosolic calcium levels upon treatment. To sum up, it could clearly be shown that the observed vacuoles are of ER origin and that this massive vacuolization and ER disturbance leads to elevated cytosolic calcium levels.

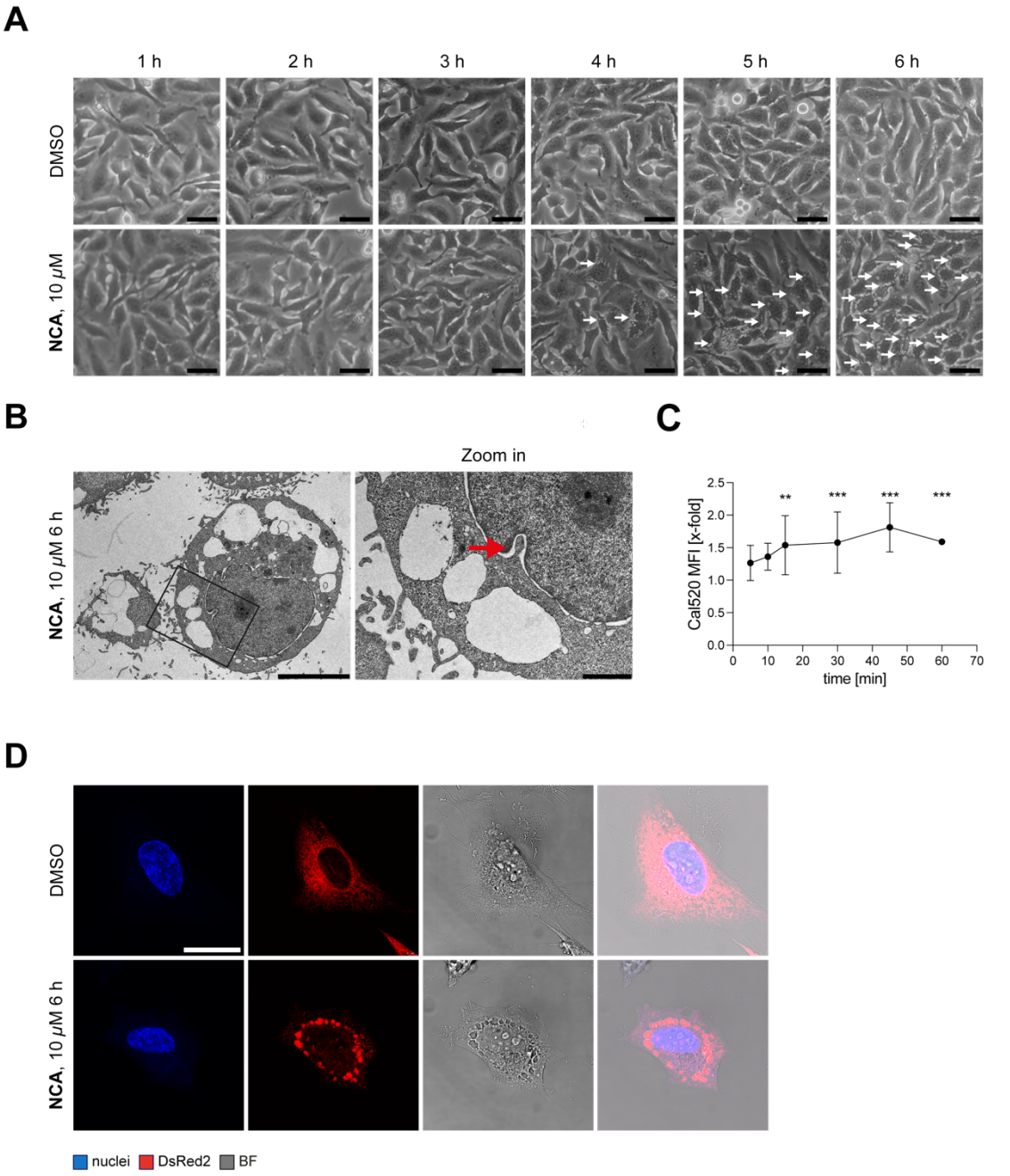

Figure 27 NCA causes massive cytoplasmic vacuolization derived from the endoplasmic reticulum leading to an increase of cytosolic calcium.
(**A**,**B**) Cytoplasmic vacuolization observed (**A**) by phase contrast conducted by Elena C. and (**B**) transmission electron microscopy in HeLa cells treated with 10 μM NCA for (**A**) 1, 2, 3, 4, 5 and (**A**,**B**) 6 h. Representative images shown, (**A**) white arrows indicate vacuoles, (**B**) red arrow indicates vacuoles budding off the nuclear envelope (scale bar (**A**) 25 μm, (**B**) left image 5000 nm, right image 1000 nm). (**C**) Analysis of cytosolic calcium by Cal520 AM flow cytometry assay. HeLa cells were loaded with the dye and treated with 10 μM NCA for the indicated times. Cal520 AM mean fluorescence was recorded. (**D**) Representative images of HeLa cells transfected with DsRed2-ER plasmid to stain the ER, then treated with 10 μM NCA for 6 h and analyzed by live cell imaging. Nuclei shown in blue, ER in red, bright field shown to display the conincidence of the ER dye and the vacuoles (scale bar 25 μm), n=3. (**C**) Data are presented in an XY graph as mean ± SD, n=3. Statistical significance was analyzed by two-way ANOVA with Fisher's LSD test. (ns ≙ not significant, *P<0.5, **P<0.01, ***P<0.001).

4.2.7 NCA causes endoplasmic reticulum stress and activates PERK branch of the unfolded protein response

ER dilatation is a characteristic of endoplasmic reticulum stress. That's why markers of this process were investigated. First, a subcellular fractionation was performed, and protein levels of the ER chaperon BiP determined in the cytosolic and membrane fraction (**Figure 28-A**). Notably, an almost two-fold increase in the cytosol to membrane ratio was demonstrated, indicating stress triggered increase of ER membrane permeability. Next, the phosphorylation status of the alpha subunit of the eIF2α and the expression of the ATF4 were determined by immunoblotting in 12, 18 and 24 h 2.5 μM NCA treated HeLa cells and compared to DMSO control and HeLa wt cells (**Figure 28-B**). Thapsigargin, a known ER stress inducer served as positive control. An increase in eIF2α phosphorylation could be shown at all times examined, however, being only significant after 12 h and then declining slowly again. ATF4 expression on the contrary reached its maximum at 24 h in line with the sequence of the PERK pathway of the UPR. Finally, in a qPCR experiment, CHOP mRNA was quantified after 18 h exposure of 2.5 μM NCA to HeLa cells compared to DMSO, with thapsigargin again serving as positive control (**Figure 28-C**). It turned out that the compound caused an enormous increase in CHOP expression on a transcriptional level, almost as pronounced as in the positive control condition. In summary, it can be stated that NCA induces strong ER stress and thereby activates the PERK branch of the UPR.

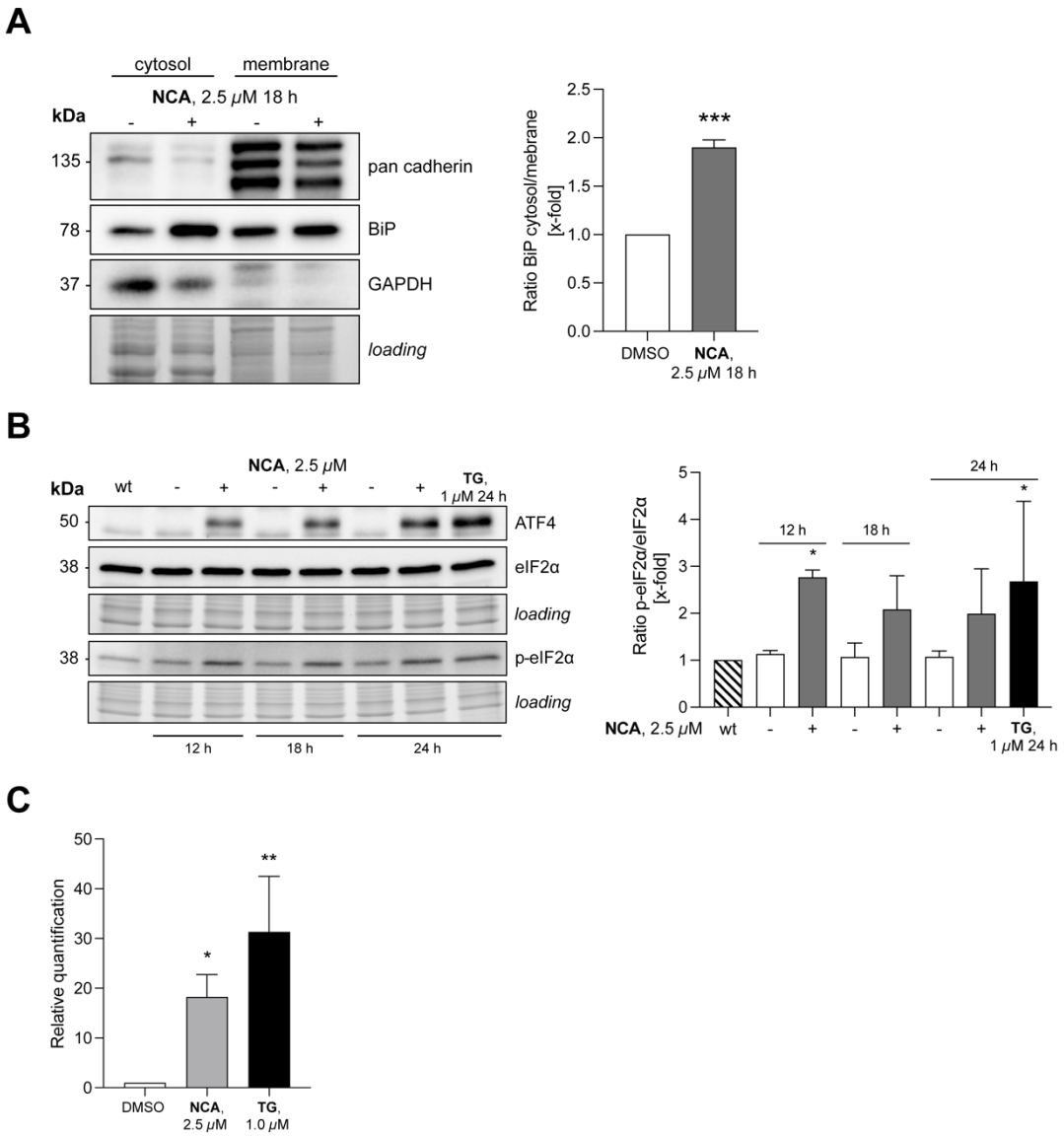

Figure 28 NCA induces ER stress and triggers the activation of the PERK branch of the UPR.
(**A**) Subcellular fractionation of HeLa cells treated with 2.5 μM NCA for 18 h with subsequent immunoblotting for BiP. (**B**) ER stress markers of HeLa cells treated with 2.5 μM NCA for 12, 18 and 24 h were analyzed via immunoblotting, thapsigargin served as positive control. (**A**,**B**) Representative blots shown on the left panel. (**C**) CHOP mRNA levels of HeLa cells treated with 2.5 μM NCA for 18 h were measured by qPCR, thapsigargin served as positive control. (**A**,**B**,**C**) Data are presented (**A**,**B** on the right panel) in bar graphs as mean ± SD, n=3. Statistical significance was analyzed by (**A**) two-tailed unpaired Student's t-test (**B**,**C**) one-way ANOVA with Dunnett's posttest (*P<0.5, **P<0.01, ***P<0.001).

4.2.8 NCA addresses endoplasmic reticulum residing reticulon 4 protein

Knowing that NCA induces ER stress and most likely thereby exhibits its mitochondrial phenotype, we were looking for ER target proteins that could explain the observed effects. ABPP target ID experiments conducted by Josef Braun (TU Munich, Germany) with the neocarzilin target probe NC-4 (full table of hits **Table S1**,**Table S2,Table S3**) revealed one prominently enriched protein that could even been out-competed by NCA, namely reticulon 4 (Rtn4) (**Figure 29-A,B**), which belongs to a family of ER-associated proteins mainly involved in shaping the ER. To confirm this protein as additional target of NCA, a staining was performed, in which HeLa cells were incubated with the NC-4 that was subsequently clicked to an AlexaFluor^{TM} 647 azide and cells were co-stained for Rtn4 (**Figure 29-C**). 50 cells in three independent experiments were analyzed with ImageJ's Coloc2 plugin and a mean Pearson's r coefficient of 0.56 was calculated, again indicating a co-localization of the target probe and the protein and thereby strongly supporting the proteomic data. In the next step, an immunofluorescence staining of Rtn4 after 6 h of NCA treatment with 10 μM of the compound compared to DMSO treated HeLa cells was conducted (**Figure 29-D**). From the exemplary images it is obvious that stimulation leads to alteration of the Rtn4 distribution, from the cell-spanning form to a clustered morphology. Due to their pronounced hydrophobicity, integral membrane proteins are difficult to crystallize to reveal their structure. That's why a complete sequence of Rtn4 is not available. However, in 2000 GrandPr *etal.* [59] identified the 66 aa long luminal domain of Rtn4 connecting the two transmembrane helices of the conserved reticulon homology domain, which is responsible for the inhibition of axonal regeneration. In order to further validate the target, a molecular docking with the nogo-66 structure and NCA was performed with the freely available Chimera UCSF software and Vina Autodock plugin (**Figure 29-E**). The docking resulted in a score of -5.5 and revealed one hydrogen bond (red) between threonine 61 and the carbonyl function of the compound, as well as additional 21 contact sites (yellow) mainly of hydrophobic nature, positioning NCA in a small binding pocket. In summary, these results strongly support the hypothesis that NCA addresses Rtn4 and thereby exerts its effects on the ER.

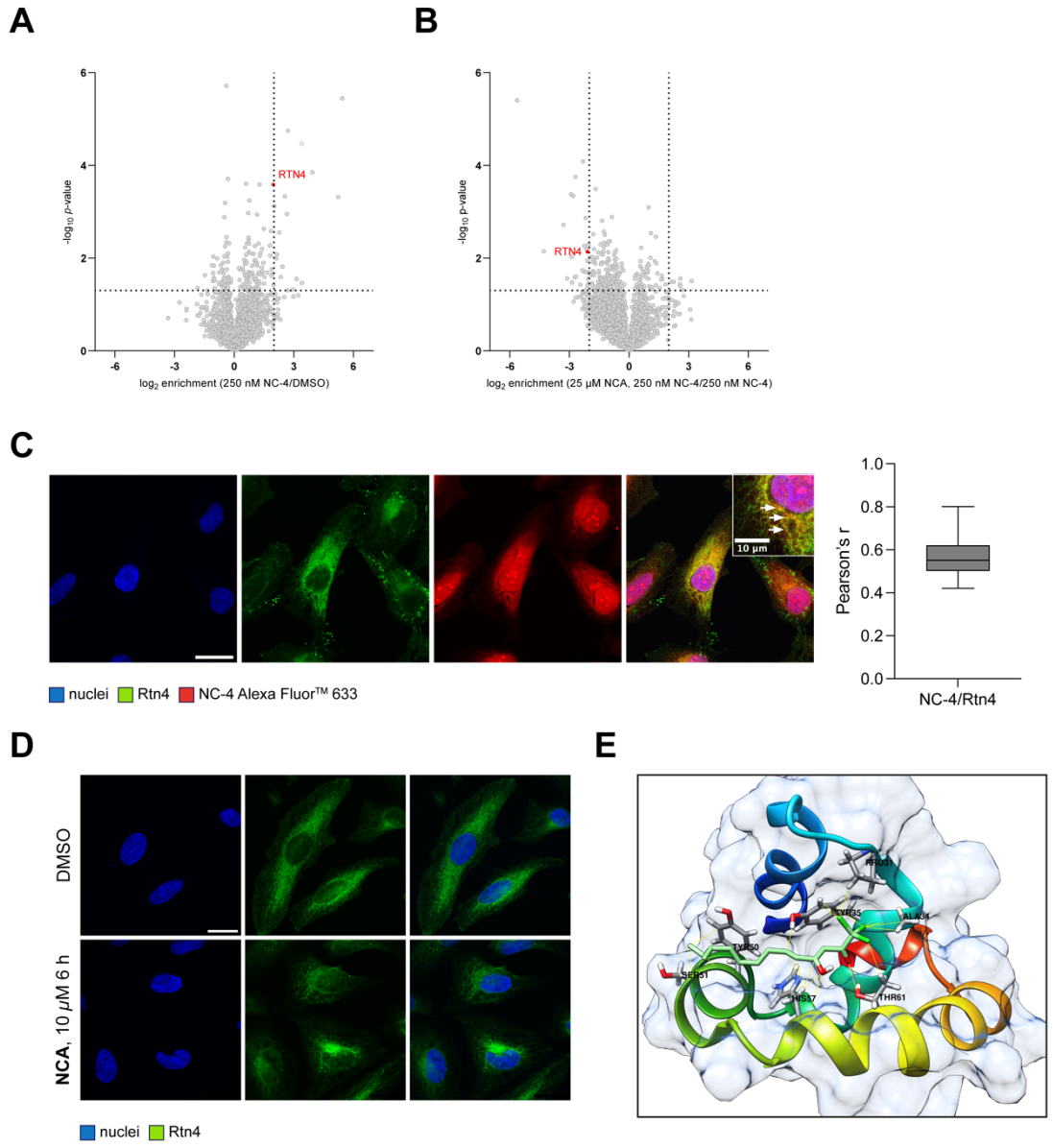

Figure 29 NCA addresses reticulon 4 protein at the ER.
(**A**) Target identification by ABPP with the NC-4 target probe in HeLa cells, (**B**) respective competition experiment both conducted by Josef B. (TU Munich). (**C**,**D**) Representative images of immunofluorescence staining of HeLa cells incubated (**C**, left panel) with the NC-4 target probe clicked to an Alexa Fluor 647 dye, (**D**) with 10 μM NCA for 6 h, n=3. (**C**,**D**) Nuclei shown in blue, Rtn4 in green, (**C**) Alexa Fluor™ 647 coupled NC-4 in red (**C**,**D** scale bar 25 μm). (**E**) Molecular docking of nogo-66 and NCA by UCSF Chimera and AutoDock Vina plugin. Contact sites are marked yellow with interacting residues labeled, hydrogen bond marked red. Data are presented (**A**,**B**) in volcano plots or (**C**, right panel) box and whiskers (min to max), (**A**,**B**) n=4, (**C**) n=3.

4.2.9 Reticulon 4 knockdown diminishes NCA effects on mitochondrial membrane potential, superoxide generation and apoptosis induction

To confirm the hypothesis that NCAs effects on mitochondrial functions and apoptosis induction are mediated by addressing reticulon 4 and provoking ER stress, siRNA mediated knockdown of the protein was performed. In a preliminary experiment, the optimum incubation time for the most effective knockdown was determined, which unfortunately was only around 60% reduction in Rtn4 expression. That's why the knockdown was validated on a regular basis (**Figure 30-D**). Subsequently, flow cytometry experiments to assess the mitochondrial membrane potential, mitochondrial superoxide and apoptosis induction were carried out and knockdown populations compared to non-targeting control cells. For the investigation of mitochondrial superoxide increase, knockdown and nt control cells were treated with 5.0 and 10.0 μM NCA for 6 h, with antimycin A serving as positive control (**Figure 30-A**). Knockdown led to a significant 21% (5 μM) and 13% (10 μM) reduction in the effect on the formation of mitochondrial superoxide, respectively, while antimycin A retained its potency. Next, the effect of 6 h 10 μM NCA treatment on the mitochondrial membrane potential after knocking down Rtn4 was assessed by a JC-1 assay (**Figure 30-B**). An even clearer difference was observed here, with a significant drop of dissipated mitochondria from 48% in the nt group to 32% in the knockdown population (34% absolute reduction). Finally, the Nicoletti apoptosis assay was repeated with Rtn4 knockdown cells after 2.5, 5.0 and 7.5 μM NCA stimulation over 48 h (**Figure 30-C**). Again, resulting in a significantly reduced response to the compound in the form of 6.8% (2.5 μM, absolute 24%), 7.3% (5.0 μM, absolute 12.2%) and 8.9% (7.5 μM, absolute 12.3%) less apoptosis induction. Taken together, these results strongly underpin the hypothesis that NCA effects on mitochondria and apoptosis induction are at least partly mediated via targeting reticulon 4.

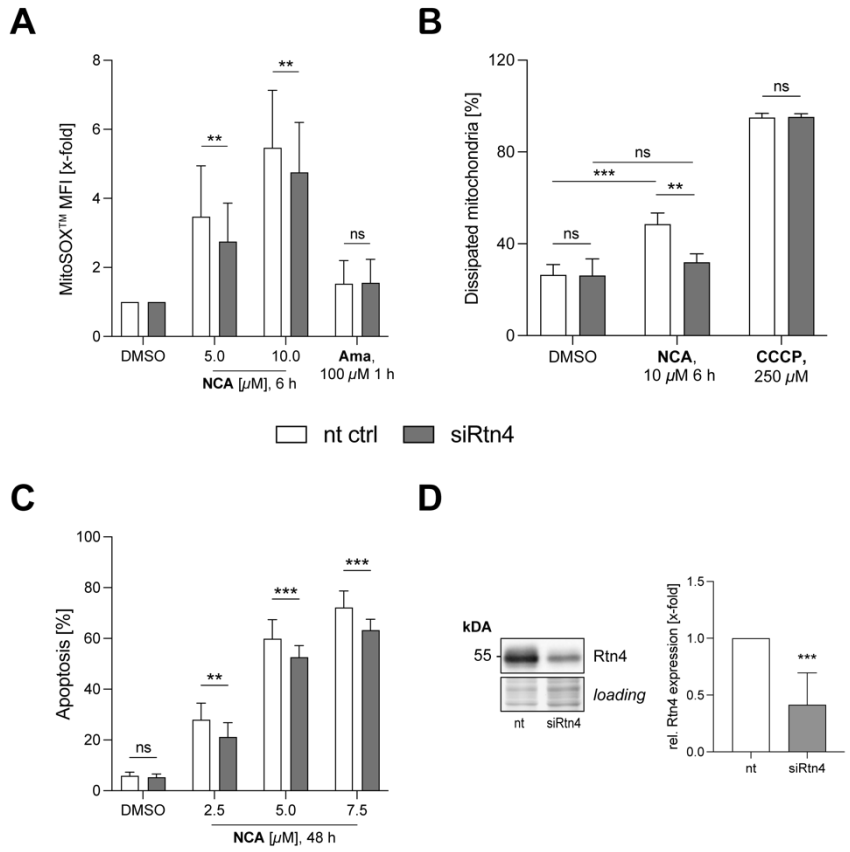

Figure 30 Reticulon 4 knockdown leads to reduced responsiveness to NCA treatment in terms of mitochondrial superoxide formation, mitochondrial membrane potential dissipation and apoptosis induction. (**A**) Mitochondrial superoxide was analyzed by MitoSOX™, (**B**) mitochondrial membrane potential by JC-1 and (**C**) apoptosis induction by propidium iodide measurement via flow cytometry. HeLa cells were transfected with Rtn4 or nt siRNA for 72 h and treated with NCA as indicated for (**A**,**B**) 6 h and (**C**) 48 h. (**A**) antimycin A and (**B**) CCCP served as positive controls. (**A**) MitoSOX™ mean fluorescence intensity, (**B**) Alexa Fluor™ 488 mean fluorescence intensity and (**C**) PE mean fluorescence intensity were recorded. Data are presented in bar graphs as mean ± SD, (**A**) n=4, (**B**,**C**) n=3. Statistical significance was analyzed by two-way ANOVA with Šídák's posttest (ns ≙ not signifikant, **P<0.01, ***P<0.001).

4.2.10 Part II: summary

In this section, we were able to show that NCA disrupts basic mitochondrial functions. Starting with an unbalancing of mitochondrial dynamics in the direction of mitochondrial fission by triggering Opa1 splicing and pronounced changes in the ultrastructure of those organelles in form of increased size, reduced matrix and cristae density and altered shape characteristics. Next, we could show that through an overload of calcium, the mitochondrial membrane potential got dissipated upon treatment with the compound and at the same time it strongly increased the production of mitochondrial superoxide. In addition, an impressive disruption of the electron transfer chain was detected, which was reflected in a reduced oxygen consumption rate, increased LEAK and reduced complex I and II respiration, as well as inhibited ATP synthesis. Moreover, the induction of apoptosis via the caspase 8/Bid/cytochrome c axis by NCA could be demonstrated. In the further progress of the investigation, it became evident that the compound causes ER stress discovered through the massive formation of cytoplasmic vacuoles and finally activates the PERK branch of the unfolded protein response. Proteomic data provided a potential target in the form of Rtn4, which was subsequently verified by immunostainings, molecular docking, and comparative knockdown experiments, in which the reduction of expression led to diminished responsiveness to our compound in terms of mitochondrial superoxide generation, dissipation of mitochondrial membrane potential and apoptosis induction.

4.3 Part III: Analysis of structure-activity relationships by biological testing of various neocarzilin derivatives and characterization of NC-4

It has already been impressively demonstrated that NCA exhibits many interesting effects on cancer cells, thus underlining its suitability as chemical tool [1, 7]. Now, we investigated whether the potency could even be increased by structural variation of the original natural compound or whether specificity for one of the phenotypes presented could be achieved by this. Therefore, a variety of derivates (**Figure 31**) were synthesized in the laboratory of Prof. Stephan Sieber (TU Munich, Garching, Germany) and subsequently tested for their antiproliferative and antimigratory activity in the final part of these studies. A special focus was placed on the target probe NC-4, which is expected to contribute to the elucidation of the antiproliferative target of the neocarzilins due to its higher structural similarity to NCA.

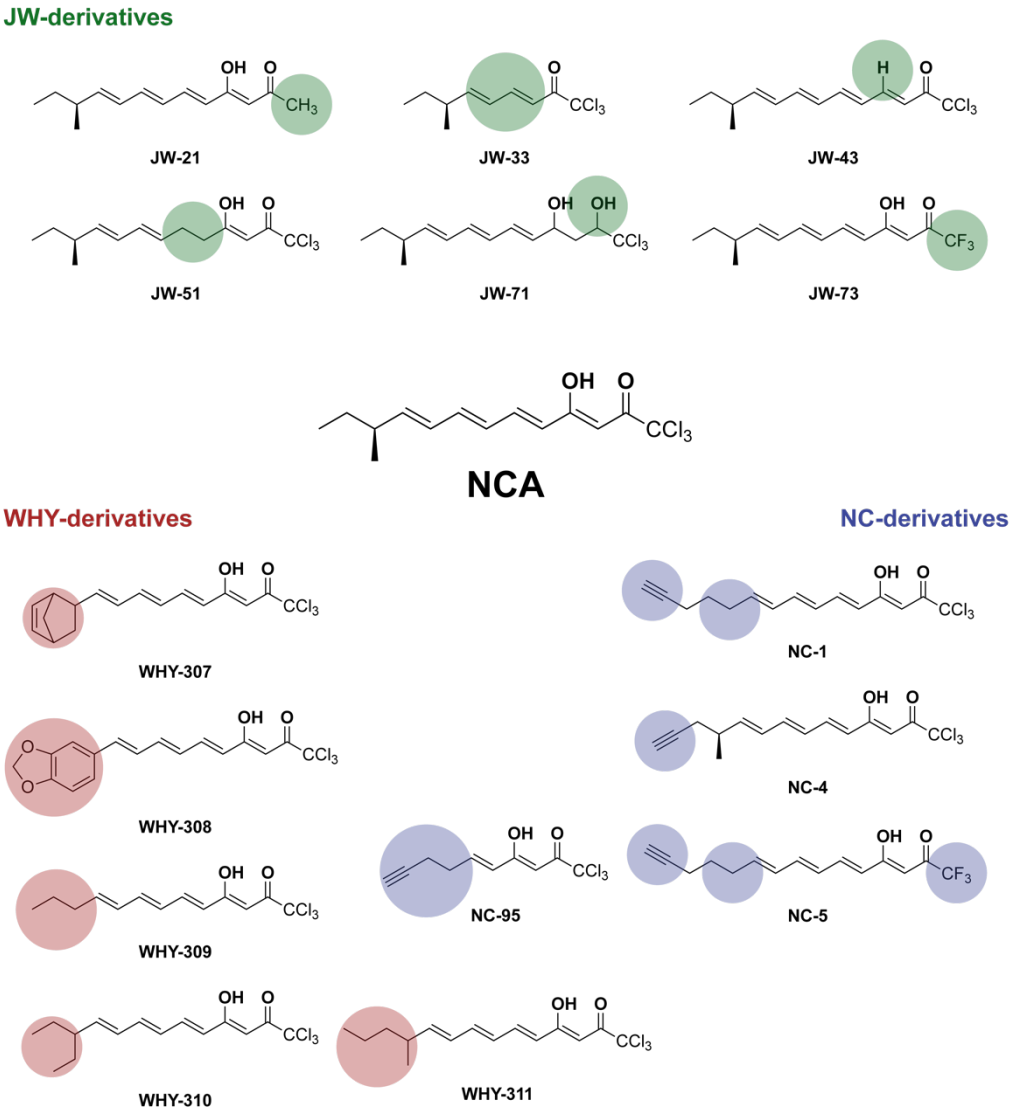

Figure 31 Structural overview of tested neocarzilin derivatives.
Compounds are arranged in groups, green = JW-derivatives, blue = NC target probe derivatives and red = WHY-derivatives. Marked regions deviate from the original structure.

4.3.1 Antiproliferative characterization of neocarzilins derivatives

The mechanism by which neocarzilins influences cell proliferation has hardly been investigated to date. Nevertheless, we started to investigate the panel of derivatives with regard to this property. For this, a crystal violet staining assay over 72 h was conducted in HeLa cells, treated with the compounds at the indicated concentrations (**Figure 32**). The JW- derivative group showed a wide range of potency, with active candidates like JW-51 (IC_{50} 4.69 μM) to very inactive representatives such as JW-21 (IC_{50} 47.2 μM). In the NC group, NC-4 was paid special attention because it was created to identify the proliferation target. Of note, NC-4 showed a comparably low IC_{50}, which was in the range of the original compound NCA (IC_{50} 1.36 μM). Remarkably, all WHY-derivatives were demonstrated to be very active, with WHY-310 exhibiting an even lower IC_{50} than the lead structure (0.92 μM).

A

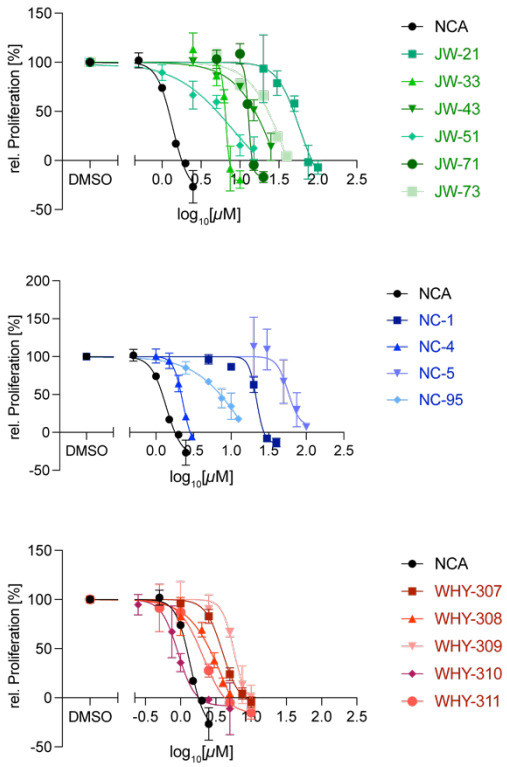

B

Group	Compound	IC_{50} [μM]
	NCA	1.36
JW	JW-21	47.2
	JW-33	6.60
	JW-43	14.5
	JW-51	4.69
	JW-71	13.0
	JW-73	22.0
NC	NC-1	22.3
	NC-4	2.17
	NC-5	57.2
	NC-95	6.79
WHY	WHY-307	3.93
	WHY-308	2.54
	WHY-309	5.73
	WHY-310	0.92
	WHY-311	2.10

Figure 32 Antiproliferative potency of neocarzilin derivatives.
Antiproliferative activity of neocarzilin derivatives was determined by crystal violet staining assay over 72 h in HeLa cells as indicated. (**A**) Data are presented as nonlinear regression curves with mean ± SD, n=3. (**B**) Table of corresponding IC_{50} values of (**A**).

4.3.2 Antimigratory characterization of neocarzilins derivatives

9 structures from the 16 derivatives were selected for further investigations regarding their capacity to inhibit cell migration. For this, an RTCA instrument was employed to monitor single cell migration in a real-time manner (**Figure 33**). HeLa cells were treated with the indicated concentrations and migration recorded for 18 h. DMSO served as positive control and wells without FCS as negative control. In general, a drop of potency from antiproliferative to antimigratory effects could be observed for all compounds. The original compound NCA showed the lowest IC_{50} value (5.20 μM) of the tested structures. Again, NC-4 was found to be in a similar range (IC_{50} 6.97 μM). The least active derivative was JW-73 (IC_{50} 64.9 μM), closely followed by JW-21 (IC_{50} 57.0 μM) and also NC-1 (IC_{50} 41.6 μM) and WHY-308 (IC_{50} 36 μM) showed only minor capacity.

A

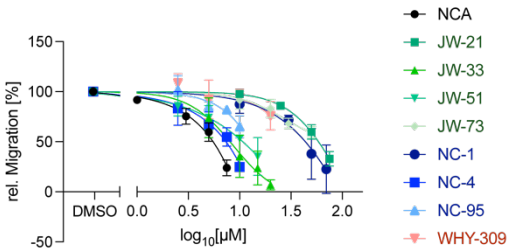

B

Group	Compound	IC_{50} [μM]
NCA		5.20
JW	JW-21	57.0
	JW-33	8.69
	JW-51	10.3
	JW-73	64.9
NC	NC-1	41.6
	NC-4	6.97
	NC-95	13.6
WHY	WHY-309	36.0

Figure 33 Antimigratory potency of neocarzilin derivatives.
(**A**) xCELLigence® migration assay of HeLa cells treated as indicated, migration monitored over 18 h. Data are presented as nonlinear regression of XY graph as mean ± SD, n=3. (**B**) Table of corresponding IC_{50} values of (**A**).

4.3.3 Part III: Summary

In the concluding part of this thesis, a wide range of neocarzilin derivatives were investigated for their antiproliferative and antimigratory potential. Initially, 6 structures of the JW derivative type, 4 neocarzilin target probes of the NC type and 5 WHY derivatives were examined with regard to their inhibition of proliferation by crystal violet staining assays. The WHY structures showed a considerably higher potency than the derivatives of the other two types, whereby WHY-310 (IC_{50} 0.92 μM) was even more active than the original compound (IC_{50} 1.36 μM). Notably, the improved version of the NC-1 target probe NC-4 (IC_{50} 2.17 μM), which was designed to discover the antiproliferative target of the neocarzilins, demonstrated a similar IC_{50} compared to NCA. In the following, 8 derivatives were selected for further investigations on their antimigratory effects. For this, xCELLigence® assays were performed to assess single cell migration. Here, a drop in potency could be observed for all tested structures, however NC-4 (IC_{50} 6.97 μM) stood out again by showing a similarly low IC_{50} value as NCA (IC_{50} 5.2 μM) and thus once again underlining its suitability to elucidate both the antiproliferative and antimigratory molecular target of the neocarzilins.

DISCUSSION

5 Discussion

5.1 Discussion Part I

5.1.1 Intracellular localization of VAT-1

Discrepancies of VAT-1 localization in the literature led us to investigate the intracellular distribution of the protein by a subcellular fractionation (**Figure 10**). Here, strong bands could be detected in the mitochondrial and membrane fraction. The purity of the fraction can be assumed to be good, with only minor contaminations of other markers. Those findings are in line with several publications [26, 27, 69] and confirmed the mitochondrial localization by immunofluorescence stainings (**Figure 12**) and the calculation of the correlation parameter Pearson's coefficient. The obtained value of 0.67 was clearly above the threshold of 0.5, which is considered a strong correlation, indicating a coincidence of the two signals.

5.1.2 Confirmation of VAT-1 as responsible antimigratory target of neocarzilins

By generating a knockout model in a cancer cell line, we were able to prove that VAT-1 is neither important for cell proliferation in general (**Figure 14-A**) nor responsible for the antiproliferative phenotype since the clones showed almost the exactly same IC_{50} value as HeLa wt and the CRISPR control cells (**Figure 14-B**). In contrast, two orthogonal assays to assess the collective as well as the single cell migration (**Figure 15**) convincingly demonstrated that VAT-1 plays a crucial role in the execution of inhibiting effect of NCA on cell migration. This was evidenced by a significant drop of the antimigratory capacity in the VAT-1 knockout cells compared to both HeLa wt and CRISPR control cells.

5.1.3 Investigation of the underlying mechanism of VAT-1's implication in cell migration

To shed further light on this mechanism, we first assessed the effect of the knockout on the process of spreading. Even though this is not actually involved in cell migration, it shares processes of cell adhesion like actin polymerization, adhesive receptor

activation and movement of the cell edges, serving as a simplified system to investigate motility behavior [70]. Under the conditions we chose (fibronectin coating, starvation condition) the so-called isotropical spreading, where the cell edges spread out in a radial manner, is favoured [71]. VAT-1 knockout had a pronounced effect on the spreading morphology of the KO clones, demonstrated by a significantly reduced spreading area and altered shape, which can rather be assigned to the anisotropic spreading (**Figure 16**). Anisotropic spreading can be the result of uneven adhesive receptor distribution [72]. So next, focal adhesions dynamics, the tightly regulated build-up and breakdown of adhesive spots, required for cellular movement was investigated. Therefore, immunofluorescence images of talin1 stained cells on fibronectin coated slides were evaluated by image analysis, focal adhesion counted, and their shape examined (**Figure 17**). And here, too, there were clear differences between VAT-1 KO clones, HeLa wt and CRISPR control cells. VAT-1 knockout reduced the number and size of focal adhesions. This indicates that their maturation which includes an increase in size is impaired by the loss of the protein and might be one explanation for the phenotype observed by NCA stimulation, especially since focal adhesion size was shown to greatly influence cell speed [73]. Finally, we investigated the activation of integrin β1. As integrins are mainly clustered and activated by talin1 [74] the putative interaction partner of VAT-1 [1], we hypothesised that their activation status must be affected by the loss of protein. Indeed, a reduced activation could be detected as reflected by a significantly reduced signal intensity of active integrin β1 in the knockout clones compared to HeLa wt cells (**Figure 18**). However, the CRISPR control showed the same result with almost the identical degree of reduction in integrin β1 activation compared to HeLa wt. Therefore, it cannot be conclusively determined whether the finding in the clones is due to the knockout of VAT-1 or rather an acquired mutation during the propagation of the single cells in the CRISPR process.

Nevertheless, we were able to show convincingly that VAT-1 is very likely engaged in the antimigratory effect of NCA. This is executed by interfering with the dynamics of focal adhesions. In addition, we were able to further characterize the VAT-1 protein by delineating its mitochondrial localization and its implication in the process of cell spreading. To shed more light on the mechanism of action by which VAT-1 mediates its role in cancer cell migration requires further studies.

5.2 Discussion Part II

The neocarzilin natural compound family was introduced more than three decades ago, with NCA showing promising cytotoxic potency against a leukemic cancer cells line. Recently Gleissner, Pyka [1] discovered additional antiproliferative and antimigratory activity, which shed a completely new light on the compound and elevated it to the category of multi-target drugs. By simultaneously addressing different targets, drug candidates like NCA can help to counter complex diseases or those that evade conventional therapies by acquiring resistance.

5.2.1 Mitochondrial phenotype of neocarzilin A

Inspired by preliminary data (**Figure S1**), we investigated the impact of NCA on mitochondrial functions and started with the examination of mitochondrial dynamics, a feature of mitochondria often being altered in cancer cells [75]. Here, we demonstrated a pronounced fragmentation of mitochondrial networks upon treatment in a time and dose-dependent manner (**Figure 19**). At the same time, the isolated mitochondria appeared to cluster around the nucleus. Among the well-known proteins involved in mitochondrial fission and fusion, we identified an alteration in the inner mitochondrial membrane fusion regulator Opa1 upon treatment. Splicing ratios of the soluble S- over the membrane anchored L-form were significantly increased (**Figure 20-A**), which might explain the fragmented network phenotype. It was repeatedly reported that, upon several stress conditions, Oma1 mediated Opa1 cleavage increases, triggering mitochondrial fission [76, 77]. Notably, we also detected a pronounced dissipation of the $\Delta\Psi m$ upon NCA exposure (**Figure 22-A**), which might explain the enhanced proteolytic cleavage of Opa1. At the same time, transmission electron microscopy images of HeLa cells treated with NCA showed a very impressive phenotype, with enlarged mitochondria, a significantly reduced matrix density and markedly decreased number of cristae, which also deviated greatly from the physiological state in the DMSO control (**Figure 21**). It appeared that instead of protruding into the lumen of the mitochondria, the remaining cristae were pressed against the outer mitochondrial membrane. Again, this phenomenon was in agreement with altered Opa1 splicing, since this fusion protein was recently reported to control mitochondrial cristae dynamics [78]. Due to the reduced matrix density,

however, we suspected mitochondrial swelling caused by inflowing water, which is often facilitated by the induction of the mitochondrial permeability transition pore [79], proposed to comprise the voltage-dependent anion channel (VDAC) [80], the proapoptotic Bcl-2 proteins Bak and Bax [81], the translocator protein (TSPO) [82] and the adenine nucleotide translocator (ATN) [83]. We couldn't confirm this hypothesis since application of the known mPTP inhibitor cyclosporin A [84] could hardly attenuate the detrimental effect of NCA on the $\Delta\Psi m$ (data not shown). Another possible mechanism to explain this phenomenon was that an initial calcium overload and osmotically following water trigger the mitochondrial swelling, accompanied by a loss of the membrane potential, as reported [85]. An indeed, concomitant application of the calcium chelator BAPTA and NCA could completely rescue the effect of the compound on the $\Delta\Psi m$ (**Figure 22-B**) underpinning the hypothesis that calcium plays an executive role. So next, we investigated whether NCA treatment changes mitochondrial calcium levels by using the calcium dye Rhod2 AM and demonstrated a dose- and time-dependent increase (**Figure 22-C**), accounting for the so far observed effects. We continued to investigate mitochondrial ROS generation, since mitochondria are the main source of it. ROS has been claimed to be elevated in various cancers, contributing to pro-tumorigenic signaling [86], but when it exceeds a certain level, on the contrary, also inducing tumor cell-death and therefore represents a feasible target for cancer therapy. We showed that already after 3 h in high doses (10 μM, **Figure 23-A**) NCA triggered extensive ROS production. This could also be partially explained by the observed Opa1 splicing, which was reported to contribute to ROS generation previously [87]. Next, we focused on cellular respiration and could show a general reduction in OCR after 6 h treatment (**Figure 24-A**). Thus, we investigated the electron transfer chain in depth by high-resolution respirometry and found a significant reduction of complex I and II respiration (**Figure 24-B,C**), in line with the reduced OCR. Remarkably, an increased respiration in the LEAK state, which can be caused chemical protonophores [88], by manipulating uncoupling proteins [89] or substances that change the permeability of the membrane [90], was observed and could even be provoked instantly by applying high doses of NCA (50 μM, **Figure 24-E**). The perturbation of complex I could separately been proven in an enzymatic assay in enriched HeLa mitochondria upon treatment with the compound (**Figure 25-A**) and also the terminal synthesis of ATP could be demonstrated to be impaired, but only after switching off the proportion provided by glycolysis through 2-DG application

(**Figure 25-B**). This implicates that HeLa cells meet most of their energy demand rather by aerobic glycolysis than by OXPHOS, according to the Warburg effect [34].

All those observations sustained the suspicion that there must be a direct mitochondrial target of NCA, especially as some of the effects seemed to be mediated in a very acute manner (e.g. ROS induction after 3 h and direct LEAK increase). Since we have knockout model cell lines of two well-validated targets of NCA (VAT-1 and BST-2) in hands, of which VAT-1 was moreover reported to be involved in mitochondrial fission and fusion [26], we investigated whether the knockout cells show a different response to the compound or morphology with regard to this phenotype. For VAT-1 and BST-2 KO mitochondrial superoxide (**Figure S5**) and additionally for VAT-1 KO MiNa analysis were repeated comparing knockout clones to HeLa wt and/or CRISPR control cells, respectively (**Figure S6**). Surprisingly, none of the cells showed differences that could completely explain the observed effects and therefore we speculated that both proteins are not the responsible targets.

5.2.2 Induction of apoptosis by neocarzilin A – extrinsic pathway

Given the strong perturbation of mitochondria, apoptosis induction upon NCA treatment was studied. We suspected that rather the intrinsic than the extrinsic pathway would be activated, since highly damaging effects on those organelles were found so far, but the opposite was the case. Activation of the extrinsic pathway could be demonstrated by caspase 8 and Bid cleavage, cytochrome c release from mitochondrial to cytoplasmic fractions and finally caspase 9, caspase 3, PARP cleavage and DNA fragmentation (**Figure 26**). However, this in turn could also be another explanation for the observed morphological changes of the cristae, since this required in order to release cytochrome c from the intermembrane space into the cytosol [91].

5.2.3 Neocarzilin A triggers endoplasmic reticulum stress – a tournaround

Observing cytoplasmic vacuole formation upon NCA treatment (**Figure 27-A**), which is a very rare phenomenon, put us on a new track. At the same time, a significant increase in cytosolic calcium was detected (**Figure 27-C**), most probably because membrane permeability increases as consequence of the dilatation, as reported previously [92] and is a reasonable explanation for the increase in mitochondrial calcium, especially as the time

sequence makes sense (1 h ER to 2-6 h mitochondria). Inspired by the insight that those vacuoles are of ER origin, which was gained by staining them with an ER localizing dye (**Figure 27-B**) induction of ER stress was examined. We could demonstrate stress induction, obvious by the release of the ER luminal cytoplasmic leakage of the BiP into the cytosol (**Figure 28-A**), which was reported to be a consequence of elevated ER membrane permeability triggered by ER stress [93]. Additionally, proteins of the PERK branch of the unfolded protein response (UPR) were assessed upon NCA stimulation. Phosphorylation of the eukaryotic initiation factor 2α (eIF2α) was found to be increased (**Figure 28-B**), which leads to global inhibition of translation to counteract the accumulation of misfolded proteins but favors the translation of proteins involved in the UPR like the activating transcription factor 4 (ATF4). Under physiological conditions, ATF4 is hardly expressed [94], and it could be shown that NCA significantly induced it (**Figure 28-B**). Among other UPR related genes, ATF4 controls C/EBP homologous protein (CHOP) transcription, which we found to be upregulated by measuring mRNA levels via qPCR (**Figure 28-C**). Under prolonged ER stress conditions, if the cell is incapable of restoring proteostasis, CHOP rises sharply and apoptosis is induced. This can be achieved by upregulation of death receptor 4 and 5 (DR4/5) [95] and would explain the activation of the extrinsic apoptosis pathway, described above. Proteomic activity-based protein profiling experiments with the neocarzilin target probe NC-4 conducted by Josef B. (TU Munich, Germany) yielded a promising hit target that matched the observed effects on the ER, namely reticulon 4 (Rtn4) (**Figure 29-A**, **Table S1**). Rtn4 was significantly depleted in competition experiments in which NC-4 was incubated in the presence of NCA (**Figure 29-B**, **Table S2**). We verified the putative target by conducting a staining with the target probe and showing a colocalization with Rtn4 (**Figure 29-C**). Furthermore, a molecular docking of the hydrophilic loop of the reticulon homology domain (RHD) nogo66 and NCA revealed binding of the compound in a small pocket with several interactions stabilizing it (**Figure 29-E**). Finally, knockdown experiments showed a significant reduced effect in KD cells compared to nt control cells (**Figure 30**), even though the decrease was not that pronounced. This indicates that binding of NCA to Rtn4 rather changes its properties than inhibiting it, because decreasing protein levels of the target didn't cause the phenotype observed by the treatment with the compound. We hypothesis that a decrease in Rtn4 presence leads to

NCA being more likely to bind its other targets. Basic tasks such as shaping the ER tubes could be taken over by other reticulon proteins to compensate for the knockdown. On the other hand, the knockdown was not very effective (average 60% reduction, **Figure 29-D**) and other reticulon proteins were also repeatedly found in ABBP experiments, in HeLa wt cell (Rtn1, **Table S1**) as well as VAT-1 KO cells (Rtn3, Rtn4, **Table S3**). So it remains questionable if NCA really specifically targets Rtn4 or rather several family members, especially since they share a high sequence identity in the binding region identified by molecular docking (**Figure 4**,**Figure 29-E**).

Mitochondria and the ER are in close contact (10-100 nm) through so-called mitochondria associated membranes (MAM). Those microdomains serve as a hub for bidirectional crosstalk to control Ca^{2+} homeostasis, mitochondrial lipid production, mitochondrial network dynamics and are a hotspot for passing on stress signals from the ER to mitochondria [96]. Recently Rtn1A was reported to play a crucial role in the architecture of MAM, enhancing ER stress and simultaneously increasing mitochondrial dysfunction [97], which raises the question if NCA's effects on reticulons could also be relayed to mitochondria by a similar dual mechanism.

Moreover, reticulon proteins were shown to be involved in regulating localization and activity of pro-apoptotic Bcl-2 family members [98] and very recently Cater *et. Al* demonstrated that Rtn4 regulates mitochondrial structure, bioenergetics and apoptosis in HeLa cells [99]. Interestingly, in their hands, Rtn4 knockdown led to filamentous mitochondrial network phenotype, reduced respiration and protection against apoptosis induction, supporting our assumption that NCA rather modulates than inhibits Rtn4.

Furthermore, a comparison of whole proteomes from HeLa cells treated with 2.5 μM NCA or 1.0 μM thapsigargin for 24 h performed by Josef B. (TU Munich, Germany) and subsequent pathway analysis conducted by Franziska T. (University of Stuttgart, Germany), revealed a strong mitochondrial dysfunction and disturbance of OXPHOS components (**Figure S8**,**Figure S9**) upon NCA treatment. Correlation analysis (**Figure S7**) with the thapsigargin treated population revealed a R value of 0.7, indicating that both compounds trigger a similar cellular reaction, with thapsigarging slightly more in the direction of ER stress and NCA towards mitochondrial disturbance. This suggests that the mechanism by which NCA triggers this interesting phenotype cannot be explained purely by the classical activation of ER stress.

interesting phenotype cannot be explained purely by the classical activation of ER stress. It should be noted that we have elucidated the mechanism of the effect of NCA on mitochondria by provoking ER stress via a verified new molecular target, which finally induces apoptosis and leads to cancer cell death. It is also very delighting, that, to our knowledge, we have identified the first small molecule that targets reticulon proteins and thus could highlight NCA as a promising tool to further explore the biology of this exciting protein family and as a potential drug lead to target reticulons.

5.2.4 Concluding hypothesis

NCA addresses Rtn4 and thereby changes its conformation and membrane topology. By this, the stabilizing effect of Rtn4 on high-curvature structures of the ER tubules is diminished and leads to dilatation visible by the massive cytoplasmic vacuolization. This, in turn, makes the membrane of those vacuoles permeable and calcium leaks out into the cytosol. Protein disulfid isomerases in the ER lumen require calcium for proper functionality and so misfolded proteins accumulate, resulting in ER stress and the activation of the PERK branch of the unfolded protein response. The cytosolic calcium gets buffered by mitochondria and leads to an overload of those organelles accompanied by a mitochondrial swelling through inrushing water and an aberrant cristae remodelling. By this, the mitochondrial membrane potential breaks down and forces the generation of mitochondrial ROS. Elevated ROS levels in turn trigger the splicing of the L-Opa1 to the S-form, most probably by proteolytic Oma1 cleavage, resulting in the fragmented network phenotype. In addition, the huge ER vacuoles press the isolated mitochondria against the nucleus and thus generate the observed clustering. At the same time, the cellular respiration gets drastically reduced and ATP synthesis comes to a halt. In parallel, the persistent ER stress leads to a strong induction of CHOP transcription, which is widely recognized as promoting apoptosis. And indeed, a strong activation of the caspase 8/Bid/cytochrome c axis of the death receptor pathway takes place, most probably also contributing to the mitochondrial phenotype and eventually leading to cell death.

5.3 Discussion Part III

In the urgent need of developing new drugs to fight cancer as the uprising disease burdens of humankind, natural substances display a rich repertoire of partly unexplored bioactive

compounds. In the third part of these studies, we investigated a panel of structurally modified NCA analogs regarding their effects on cell proliferation and the capability to inhibit cell migration.

5.3.1 Antiproliferative potency – there is even more than NCA

Beginning with the antiproliferative testing, we identified a derivative (WHY-310, 0.92 μM) that was even more potent than the original compound (NCA, 1.36 μM) evident by the lower IC_{50} value. Interestingly, the structural difference of WHY-310 and the lead structure is very minor, in the form of an ethyl instead of a methyl group at the end of the polyene chain. Although this leads to the loss of the only stereocenter in the molecule, it seems rather important that there is some kind of carbon chain at all. This is obvious from the fact, that all derivatives lacking this feature (NC-1, NC-5 and WHY-309) exhibit a considerable loss of activity compared to their counterparts with the methyl group at this position (NC-4 and NCA). Another moiety that appears to have a significant influence on the antiproliferative activity, is the methyl ketone head group, which was hypothesised to react in an electrophilic reaction with its targets. All substances that don't bear the trichloromethyl ketone (JW-21, JW-73 and NC-5) like NCA face a pronounced drop of potency. Simply replacing the halogen chlorine with fluorine (JW-73) appears to have less drastic effects than replacing it with a methyl group (JW-21). Nevertheless, it is astonishing, since in the medicinal chemistry the introduction of a trofluoromethyl group is classically intended to enhance ligand binding to proteins in [100]. The reduced activity might be explained by the fact that chlorine and fluorine differ in their atomic radius and the bond length and strength to carbon, so that the trichloromethyl group simply fits better into the bonding site. Another modification that leads to reduction in activity by a factor of ten, is the exchange of the carbonyl function to a hydroxy group (JW-71) or the removal of the adjacent enolic hydroxy group (JW-43), both of which changes the acidic character of the molecule achieved by an intramolecular hydrogen bond between the two moieties. A general trend that could be observed for the antiproliferative effectiveness, is that introducing a terminal alkyne handle (NC-1, NC-4, NC-5 and NC-95) leads to higher IC_{50} values. This might be explained by their greater reactivity due to a higher electron content or the limited flexibility compared to an alkane group. Noteworthy, the WHY-derivatives in general had a high antiproliferative potency and thus implying that modification in the rear part of the molecule, except for the above-mentioned loss of the carbon side at C-11

have no major effect on the antiproliferative potency of the structures. It also seems the total length of the molecule is not so decisive, since JW-33 and NC-95 do not show such a pronounced loss of potency as other manipulations. In fact, NC-95 has turned out to be even more active than its longer counterpart NC-1, which is difficult with the data available to us. All these assumptions made so far about structure-activity relationships with regard to the antiproliferative effect of neocarzilins can be summarised perfectly in the compound NC-5. It combines all features that lead to a reduced activity, evident by the highest IC_{50} of all tested derivatives: the terminal alkyne handle, the missing alkane group at C-11 and the trifluoro- instead of the trichloromethyl ketone headgroup leading to a drastic drop of potency.

5.3.2 Inhibition of migration through neocarzilins

From the original panel, which contained 16 derivatives, 9 were chosen for further testing with respect to their antimigratory activity. Care was taken to select structures with high (NCA and NC-4), medium (JW-33, JW-51, NC-95 and WHY-309), and low (JW-21, JW-73 and NC-1) antiproliferative effects. The idea behind this was to examine whether there are structural modifications that favour one of the two phenotypes.
In general, the results show that all tested compounds show a loss of potency when moving from the antiproliferative to the antimigratory effect. Of course, it must be mentioned that proliferation assays are carried out over a much longer period than the migration assays (72 h vs. 18 h), therefore IC_{50} values are hard to compare, but ratios of the two values can serve as parameter to compare the compounds among each other.
For migration inhibition, NCA was the most potent tested structure in our hands, with an IC_{50} of 5.20 μM closely followed by NC-4 (6.97 μM) and JW-33 (8.69 μM). Interestingly, the drop from antiproliferation to -migration is more pronounced with NCA ($\sim$ 3.8x) than with NC-4 ($\sim$ 3.2x) and JW-33 displays very similar values for both effects ($\sim$ 1.3x). It therefore appears that shortening of the carbon chain has a greater impact on the antiproliferative effect than on the inhibition of migration. This assumption also holds true for NC-95, which exhibits an IC_{50} of 13.6 μM and a factor of 2.0x. JW-21 (57.0 μM) and JW-73 (64.9 μM) again resulted in high IC_{50}, but the drop for JW-73 ($\sim$ 3.0x) is considerably stronger than with JW-21 ($\sim$ 1.2x), implicating that the exchange of the trichloro- to the trifluoromethyl ketone affects the antimigratory potency more than

replacing it by a methyl ketone. NC-1 showed a high IC50 of of 41.6 µM but a factor of 1.9x comparable to JW-51 (IC_{50} 10.3 μM) with a factor of 2.2x. The most pronounced increase of the IC_{50} was observed for WHY-309 (IC_{50} 36 μM, ~ 6.3x).

In summary, the investigation into the biological activity of these various neocarzilin derivatives has provided interesting insights into structure-activity relationships in regard to their antiproliferative and -migratory activity. In addition, we were able to show that the structurally refined target probe NC-4 is suitable for identifying the antiproliferative target of neocarzilins, as demonstrated by a very similar IC_{50} in terms of inhibition of proliferation compared to the original natural compound NCA.

REFERENCES

6 References

1. Gleissner, C.M., et al., *Neocarzilin A Is a Potent Inhibitor of Cancer Cell Motility Targeting VAT-1 Controlled Pathways.* ACS Cent Sci, 2019. **5**(7): p. 1170-1178.
2. Newman, D.J. and G.M. Cragg, *Natural Products as Sources of New Drugs over the Nearly Four Decades from 01/1981 to 09/2019.* Journal of Natural Products, 2020. **83**(3): p. 770-803.
3. Atanasov, A.G., et al., *Natural products in drug discovery: advances and opportunities.* Nature Reviews Drug Discovery, 2021. **20**(3): p. 200-216.
4. Quinn, G.A., et al., *Streptomyces from traditional medicine: sources of new innovations in antibiotic discovery.* Journal of Medical Microbiology, 2020. **69**(8): p. 1040-1048.
5. Talevi, A., *Multi-target pharmacology: possibilities and limitations of the "skeleton key approach" from a medicinal chemist perspective.* Frontiers in Pharmacology, 2015. **6**.
6. Yıldırım, M.A., et al., *Drug—target network.* Nature Biotechnology, 2007. **25**(10): p. 1119-1126.
7. Nozoe, S., et al., *Neocarzilins A and B, Novel Polyenones from Streptomyces Carzinostaticus.* Tetrahedron Letters, 1992. **33**(49): p. 7547-7550.
8. Otsuka, M., et al., *Cloning, sequencing, and functional analysis of an iterative type I polyketide synthase gene cluster for biosynthesis of the antitumor chlorinated polyenone neocarzilin in "Streptomyces carzinostaticus".* Antimicrob Agents Chemother, 2004. **48**(9): p. 3468-76.
9. Hanahan, D. and R.A. Weinberg, *The hallmarks of cancer.* Cell, 2000. **100**(1): p. 57-70.
10. Wells, A., et al., *Targeting tumor cell motility as a strategy against invasion and metastasis.* Trends Pharmacol Sci, 2013. **34**(5): p. 283-9.
11. McGrath, J.L., *Cell spreading: the power to simplify.* Curr Biol, 2007. **17**(10): p. R357-8.
12. Cuvelier, D., et al., *The universal dynamics of cell spreading.* Curr Biol, 2007. **17**(8): p. 694-9.
13. Chamaraux, F., et al., *Kinetics of cell spreading.* Phys Rev Lett, 2005. **94**(15): p. 158102.
14. Mishra, Y.G. and B. Manavathi, *Focal adhesion dynamics in cellular function and disease.* Cellular Signalling, 2021. **85**: p. 110046.
15. Pascalis, C.D. and S. Etienne-Manneville, *Single and collective cell migration: the mechanics of adhesions.* Molecular Biology of the Cell, 2017. **28**(14): p. 1833-1846.
16. Ziegler, W.H., et al., *Integrin connections to the cytoskeleton through talin and vinculin.* Biochem Soc Trans, 2008. **36**(Pt 2): p. 235-9.
17. Linial, M., K. Miller, and R.H. Scheller, *VAT 1: An abundant membrane protein from torpedo cholinergic synaptic vesicles.* Neuron, 1989. **2**(3): p. 1265-1273.
18. Linial, M. and O. Levius, *VAT-1 from Torpedo is a membranous homologue of zeta crystallin.* FEBS Lett, 1993. **315**(1): p. 91-4.

19. Persson, B., J.S. Zigler, Jr., and H. Jörnvall, *A super-family of medium-chain dehydrogenases/reductases (MDR). Sub-lines including zeta-crystallin, alcohol and polyol dehydrogenases, quinone oxidoreductase enoyl reductases, VAT-1 and other proteins.* Eur J Biochem, 1994. **226**(1): p. 15-22.
20. Hayess, K., et al., *Mammalian protein homologous to VAT-1 of Torpedo californica: isolation from Ehrlich ascites tumor cells, biochemical characterization, and organization of its gene.* J Cell Biochem, 1998. **69**(3): p. 304-15.
21. Heng, W., et al., *Expression of VAT1 in hepatocellular carcinoma and its clinical significance.* Neoplasma, 2021. **68**(2): p. 416-422.
22. Mottaghi-Dastjerdi, N., et al. *Gene expression profiling revealed overexpression of vesicle amine transport protein-1 (VAT-1) as a potential oncogene in gastric cancer*. 2016.
23. Mertsch, S., et al., *Vesicle amine transport protein-1 (VAT-1) is upregulated in glioblastomas and promotes migration.* Neuropathol Appl Neurobiol, 2009. **35**(4): p. 342-52.
24. Shan, X., et al., *High expression of VAT1 is a prognostic biomarker and predicts malignancy in glioblastoma.* Oncol Rep, 2019. **42**(4): p. 1422-1430.
25. Mori, F., et al., *VAT-1 is a novel pathogenic factor of progressive benign prostatic hyperplasia.* Prostate, 2011. **71**(14): p. 1579-86.
26. Eura, Y., et al., *Identification of a novel protein that regulates mitochondrial fusion by modulating mitofusin (Mfn) protein function.* J Cell Sci, 2006. **119**(Pt 23): p. 4913-25.
27. Junker, M. and T.A. Rapoport, *Involvement of VAT-1 in Phosphatidylserine Transfer from the Endoplasmic Reticulum to Mitochondria.* Traffic, 2015. **16**(12): p. 1306-17.
28. Watanabe, Y., et al., *Structural basis for interorganelle phospholipid transport mediated by VAT-1.* J Biol Chem, 2020. **295**(10): p. 3257-3268.
29. Kim, S.Y., et al., *Structural insights into vesicle amine transport-1 (VAT-1) as a member of the NADPH-dependent quinone oxidoreductase family.* Sci Rep, 2021. **11**(1): p. 2120.
30. Wallin, I.E., *Symbionticism and the Origin of Species*. 1927: Рипол Классик.
31. Annesley, S.J. and P.R. Fisher, *Mitochondria in Health and Disease.* Cells, 2019. **8**(7).
32. Chan, D.C., *Mitochondrial Dynamics and Its Involvement in Disease.* Annu Rev Pathol, 2020. **15**: p. 235-259.
33. Zong, W.X., J.D. Rabinowitz, and E. White, *Mitochondria and Cancer.* Mol Cell, 2016. **61**(5): p. 667-676.
34. Warburg, O., *The metabolism of carcinoma cells.* The Journal of Cancer Research, 1925. **9**(1): p. 148-163.
35. Hanahan, D. and R.A. Weinberg, *Hallmarks of cancer: the next generation.* Cell, 2011. **144**(5): p. 646-74.
36. Simons, A.L., et al., *2-Deoxy-D-glucose combined with cisplatin enhances cytotoxicity via metabolic oxidative stress in human head and neck cancer cells.* Cancer Res, 2007. **67**(7): p. 3364-70.

37. Belzacq, A.S., et al., *Adenine nucleotide translocator mediates the mitochondrial membrane permeabilization induced by lonidamine, arsenite and CD437.* Oncogene, 2001. **20**(52): p. 7579-87.
38. Sarin, S.K., et al., *High dose vitamin K3 infusion in advanced hepatocellular carcinoma.* J Gastroenterol Hepatol, 2006. **21**(9): p. 1478-82.
39. Fulda, S., L. Galluzzi, and G. Kroemer, *Targeting mitochondria for cancer therapy.* Nature Reviews Drug Discovery, 2010. **9**(6): p. 447-464.
40. Pustylnikov, S., et al., *Targeting mitochondria in cancer: current concepts and immunotherapy approaches.* Transl Res, 2018. **202**: p. 35-51.
41. Elmore, S., *Apoptosis: a review of programmed cell death.* Toxicol Pathol, 2007. **35**(4): p. 495-516.
42. D'Arcy, M.S., *Cell death: a review of the major forms of apoptosis, necrosis and autophagy.* Cell Biology International, 2019. **43**(6): p. 582-592.
43. Rampal, G., et al., *Role of isothiocyanates as anticancer agents and their contributing molecular and cellular mechanisms.* 2023.
44. Lee, C. and L.B. Chen, *Dynamic behavior of endoplasmic reticulum in living cells.* Cell, 1988. **54**(1): p. 37-46.
45. Schwarz, D.S. and M.D. Blower, *The endoplasmic reticulum: structure, function and response to cellular signaling.* Cell Mol Life Sci, 2016. **73**(1): p. 79-94.
46. Shibata, Y., et al., *Mechanisms Determining the Morphology of the Peripheral ER.* Cell, 2010. **143**(5): p. 774-788.
47. Qi, Z. and L. Chen, *Endoplasmic Reticulum Stress and Autophagy.* Adv Exp Med Biol, 2019. **1206**: p. 167-177.
48. Oslowski, C.M. and F. Urano, *Measuring ER stress and the unfolded protein response using mammalian tissue culture system.* Methods Enzymol, 2011. **490**: p. 71-92.
49. Yamaguchi, H. and H.G. Wang, *CHOP is involved in endoplasmic reticulum stress-induced apoptosis by enhancing DR5 expression in human carcinoma cells.* J Biol Chem, 2004. **279**(44): p. 45495-502.
50. Chen, X. and J.R. Cubillos-Ruiz, *Endoplasmic reticulum stress signals in the tumour and its microenvironment.* Nature Reviews Cancer, 2021. **21**(2): p. 71-88.
51. Hetz, C., K. Zhang, and R.J. Kaufman, *Mechanisms, regulation and functions of the unfolded protein response.* Nat Rev Mol Cell Biol, 2020. **21**(8): p. 421-438.
52. Di Sano, F., P. Bernardoni, and M. Piacentini, *The reticulons: Guardians of the structure and function of the endoplasmic reticulum.* Experimental Cell Research, 2012. **318**(11): p. 1201-1207.
53. Voeltz, G.K., et al., *A Class of Membrane Proteins Shaping the Tubular Endoplasmic Reticulum.* Cell, 2007. **130**.
54. Jozsef, L., et al., *Reticulon 4 Is Necessary for Endoplasmic Reticulum Tubulation, STIM1-Orai1 Coupling, and Store-operated Calcium Entry.* Journal of Biological Chemistry, 2014. **289**(13): p. 9380-9395.
55. Wakana, Y., et al., *Reticulon 3 is involved in membrane trafficking between the endoplasmic reticulum and Golgi.* Biochem Biophys Res Commun, 2005. **334**(4): p. 1198-205.
56. Zhu, L., et al., *Anti-apoptotic activity of Bcl-2 is enhanced by its interaction with RTN3.* Cell Biol Int, 2007. **31**(8): p. 825-30.

57. Caroni, P. and M.E. Schwab, *Two membrane protein fractions from rat central myelin with inhibitory properties for neurite growth and fibroblast spreading.* J Cell Biol, 1988. **106**(4): p. 1281-8.
58. Spillmann, A.A., et al., *Identification and characterization of a bovine neurite growth inhibitor (bNI-220).* J Biol Chem, 1998. **273**(30): p. 19283-93.
59. GrandPré, T., et al., *Identification of the Nogo inhibitor of axon regeneration as a Reticulon protein.* Nature, 2000. **403**(6768): p. 439-444.
60. Mi, S., et al., *LINGO-1 is a component of the Nogo-66 receptor/p75 signaling complex.* Nat Neurosci, 2004. **7**(3): p. 221-8.
61. Mi, S., et al., *LINGO-1 negatively regulates myelination by oligodendrocytes.* Nat Neurosci, 2005. **8**(6): p. 745-51.
62. Kucher, K., et al., *First-in-Man Intrathecal Application of Neurite Growth-Promoting Anti-Nogo-A Antibodies in Acute Spinal Cord Injury.* Neurorehabilitation and Neural Repair, 2018. **32**: p. 154596831877637.
63. Yang, Y.S. and S.M. Strittmatter, *The reticulons: a family of proteins with diverse functions.* Genome Biol, 2007. **8**(12): p. 234.
64. Nicoletti, I., et al., *A rapid and simple method for measuring thymocyte apoptosis by propidium iodide staining and flow cytometry.* J Immunol Methods, 1991. **139**(2): p. 271-9.
65. de Wit, L.E.A. and W. Sluiter, *Chapter 9 Reliable Assay for Measuring Complex I Activity in Human Blood Lymphocytes and Skin Fibroblasts*, in *Methods in Enzymology*. 2009, Academic Press. p. 169-181.
66. Horzum, U., B. Ozdil, and D. Pesen-Okvur, *Step-by-step quantitative analysis of focal adhesions.* MethodsX, 2014. **1**: p. 56-9.
67. Bradford, M.M., *A rapid and sensitive method for the quantitation of microgram quantities of protein utilizing the principle of protein-dye binding.* Anal Biochem, 1976. **72**: p. 248-54.
68. Fleige, S., et al., *Comparison of relative mRNA quantification models and the impact of RNA integrity in quantitative real-time RT-PCR.* Biotechnol Lett, 2006. **28**(19): p. 1601-13.
69. Faugaret, D., et al., *An essential role for phospholipase D in the recruitment of vesicle amine transport protein-1 to membranes in human neutrophils.* Biochem Pharmacol, 2011. **81**(1): p. 144-56.
70. Döbereiner, H.G., et al., *Dynamic phase transitions in cell spreading.* Phys Rev Lett, 2004. **93**(10): p. 108105.
71. Ng, I.C., et al., *Anatomy and Physiology for Biomaterials Research and Development*, in *Encyclopedia of Biomedical Engineering*, R. Narayan, Editor. 2019, Elsevier: Oxford. p. 225-236.
72. Zemel, A., et al., *Cell shape, spreading symmetry and the polarization of stress-fibers in cells.* J Phys Condens Matter, 2010. **22**(19): p. 194110.
73. Kim, D.H. and D. Wirtz, *Focal adhesion size uniquely predicts cell migration.* Faseb j, 2013. **27**(4): p. 1351-61.
74. Sun, H., F. Lagarrigue, and M.H. Ginsberg, *The Connection Between Rap1 and Talin1 in the Activation of Integrins in Blood Cells.* Front Cell Dev Biol, 2022. **10**: p. 908622.
75. Ma, Y., L. Wang, and R. Jia, *The role of mitochondrial dynamics in human cancers.* Am J Cancer Res, 2020. **10**(5): p. 1278-1293.

76. Head, B., et al., *Inducible proteolytic inactivation of OPA1 mediated by the OMA1 protease in mammalian cells.* Journal of Cell Biology, 2009. **187**(7): p. 959-966.
77. Baker, M.J., et al., *Stress-induced OMA1 activation and autocatalytic turnover regulate OPA1-dependent mitochondrial dynamics.* Embo j, 2014. **33**(6): p. 578-93.
78. Hu, C., et al., *OPA1 and MICOS Regulate mitochondrial crista dynamics and formation.* Cell Death & Disease, 2020. **11**(10): p. 940.
79. Haworth, R.A. and D.R. Hunter, *The Ca2+-induced membrane transition in mitochondria. II. Nature of the Ca2+ trigger site.* Arch Biochem Biophys, 1979. **195**(2): p. 460-7.
80. Szabó, I., V. De Pinto, and M. Zoratti, *The mitochondrial permeability transition pore may comprise VDAC molecules. II. The electrophysiological properties of VDAC are compatible with those of the mitochondrial megachannel.* FEBS Lett, 1993. **330**(2): p. 206-10.
81. Patel, P., et al., *Inhibition of the Anti-Apoptotic Bcl-2 Family by BH3 Mimetics Sensitize the Mitochondrial Permeability Transition Pore Through Bax and Bak.* Front Cell Dev Biol, 2021. **9**: p. 765973.
82. Pastorino, J.G., et al., *Protoporphyrin IX, an endogenous ligand of the peripheral benzodiazepine receptor, potentiates induction of the mitochondrial permeability transition and the killing of cultured hepatocytes by rotenone.* J Biol Chem, 1994. **269**(49): p. 31041-6.
83. Halestrap, A.P. and C. Brenner, *The adenine nucleotide translocase: a central component of the mitochondrial permeability transition pore and key player in cell death.* Curr Med Chem, 2003. **10**(16): p. 1507-25.
84. Sharov, V.G., et al., *Cyclosporine A attenuates mitochondrial permeability transition and improves mitochondrial respiratory function in cardiomyocytes isolated from dogs with heart failure.* J Mol Cell Cardiol, 2007. **42**(1): p. 150-8.
85. Jang, S., et al., *Analysis of Mitochondrial Calcium Retention Capacity in Cultured Cells: Permeabilized Cells Versus Isolated Mitochondria.* Frontiers in Physiology, 2021. **12**.
86. Sabharwal, S.S. and P.T. Schumacker, *Mitochondrial ROS in cancer: initiators, amplifiers or an Achilles' heel?* Nat Rev Cancer, 2014. **14**(11): p. 709-21.
87. Jang, S. and S. Javadov, *OPA1 regulates respiratory supercomplexes assembly: The role of mitochondrial swelling.* Mitochondrion, 2020. **51**: p. 30-39.
88. Monteiro, J.P., et al., *Interaction of carbonylcyanide p-trifluoromethoxyphenylhydrazone (FCCP) with lipid membrane systems: a biophysical approach with relevance to mitochondrial uncoupling.* J Bioenerg Biomembr, 2011. **43**(3): p. 287-98.
89. Cadenas, S., *Mitochondrial uncoupling, ROS generation and cardioprotection.* Biochim Biophys Acta Bioenerg, 2018. **1859**(9): p. 940-950.
90. Barker, J.L. and H. Levitan, *Mitochondrial uncoupling agents. Effects on membrane permeability of molluscan neurons.* J Membr Biol, 1975. **25**(3-4): p. 361-80.

91. Wasilewski, M. and L. Scorrano, *The changing shape of mitochondrial apoptosis.* Trends Endocrinol Metab, 2009. **20**(6): p. 287-94.
92. Borradaile, N.M., et al., *Disruption of endoplasmic reticulum structure and integrity in lipotoxic cell death.* J Lipid Res, 2006. **47**(12): p. 2726-37.
93. Wang, X., et al., *Bcl-2 proteins regulate ER membrane permeability to luminal proteins during ER stress-induced apoptosis.* Cell Death & Differentiation, 2011. **18**(1): p. 38-47.
94. Memme, J.M., V.C. Sanfrancesco, and D.A. Hood, *Activating transcription factor 4 regulates mitochondrial content, morphology, and function in differentiating skeletal muscle myotubes.* American Journal of Physiology-Cell Physiology, 2023. **325**(1): p. C224-C242.
95. Hu, H., et al., *The C/EBP Homologous Protein (CHOP) Transcription Factor Functions in Endoplasmic Reticulum Stress-Induced Apoptosis and Microbial Infection.* Frontiers in Immunology, 2019. **9**.
96. Eysert, F., et al., *Molecular Dysfunctions of Mitochondria-Associated Membranes (MAMs) in Alzheimer's Disease.* Int J Mol Sci, 2020. **21**(24).
97. Xie, Y., et al., *Reticulon-1A mediates diabetic kidney disease progression through endoplasmic reticulum-mitochondrial contacts in tubular epithelial cells.* Kidney Int, 2022. **102**(2): p. 293-306.
98. Tagami, S., et al., *A novel protein, RTN-xS, interacts with both Bcl-xL and Bcl-2 on endoplasmic reticulum and reduces their anti-apoptotic activity.* Oncogene, 2000. **19**(50): p. 5736-5746.
99. Carter, R.J., et al., *Novel roles of RTN4 and CLIMP-63 in regulating mitochondrial structure, bioenergetics and apoptosis.* Cell Death & Disease, 2022. **13**(5): p. 436.
100. Shah, P. and A.D. Westwell, *The role of fluorine in medicinal chemistry.* Journal of Enzyme Inhibition and Medicinal Chemistry, 2007. **22**(5): p. 527-540.

APPENDIX

7 Appendix

7.1 Supplementary figures

S1

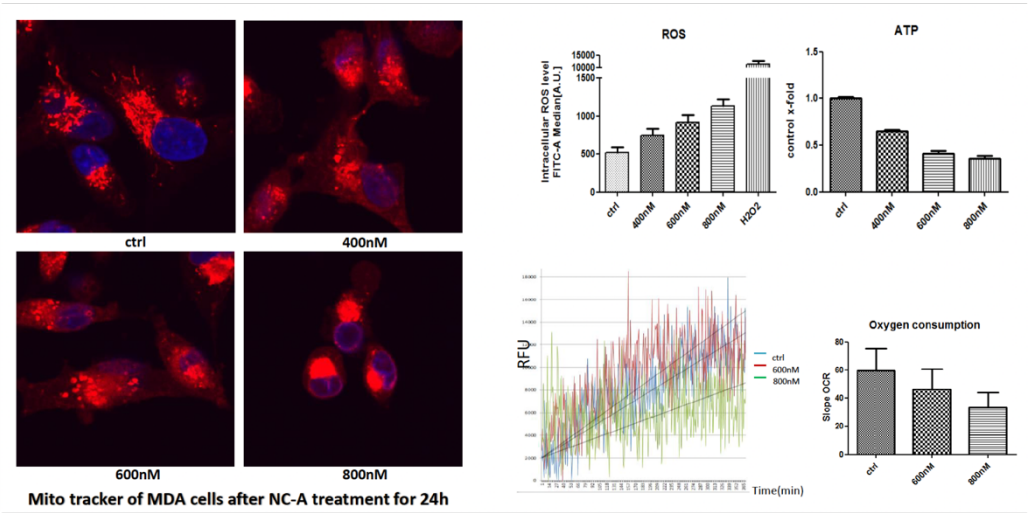

Figure S1 Preliminary mitochondria data.
Experiments conducted by Weiting C. Left panel MitoTracker™ Red staining in HeLa cells treated with NCA as indicated. Right panel ROS, ATP and OCR measurements upon NCA treatment as indicated for 24 h.

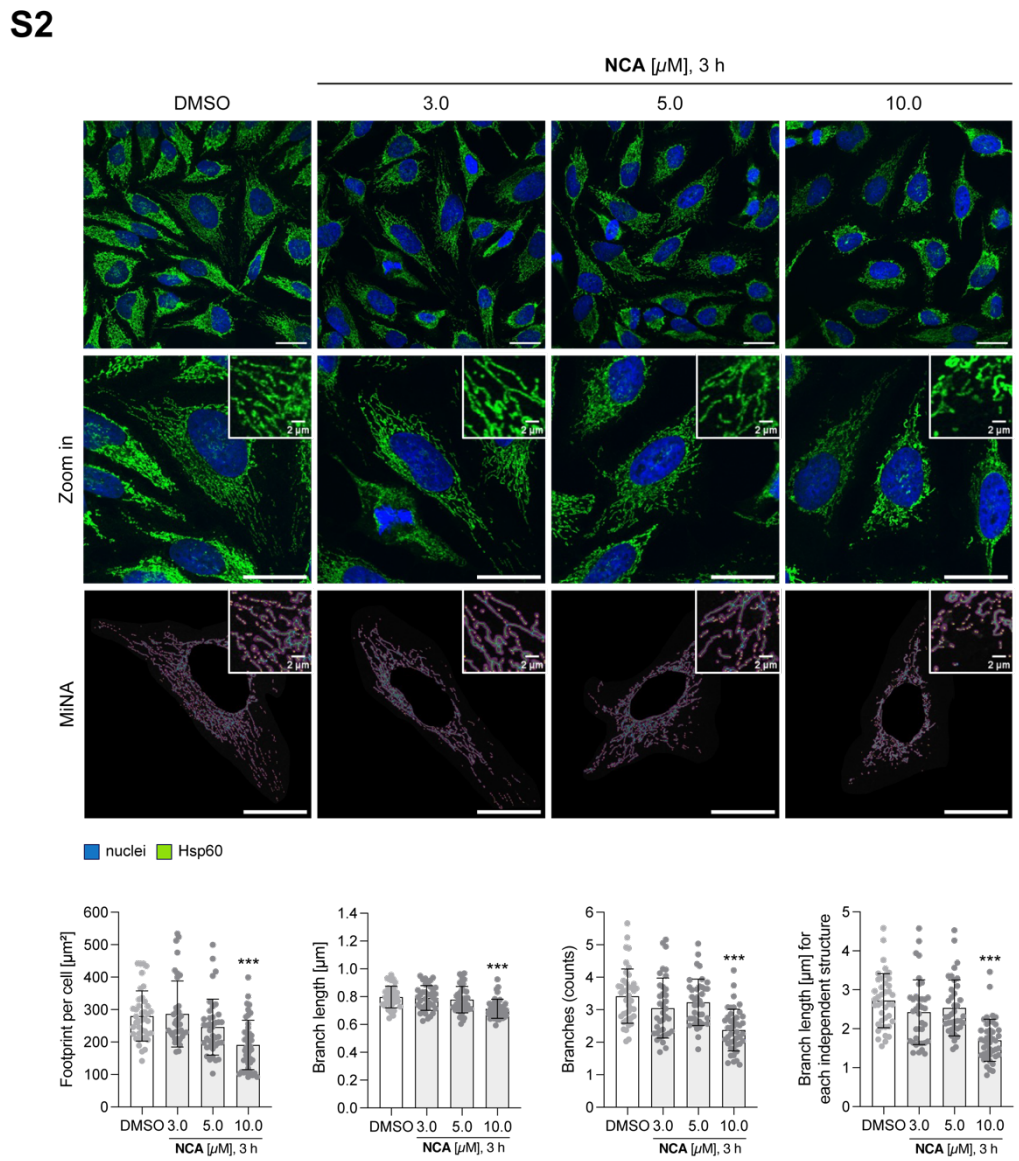

Figure S2 NCA treatment favours mitochondrial network fission and clustering of mitochondria around the nucleus.
Analysis of mitochondrial dynamics in HeLa cells upon NCA treatment at the indicated concentration for 3 h conducted by Elena C.. Representative images of immunofluorescence staining of HeLa wt cells on the top panel, nuclei shown in blue, Hsp60 in green (scale bar 25 μm). Brightness was adjusted to improve visibility. Bottom row shows MiNA analysis, purple area represents mitochondrial footprint, green lines mitochondrial length, blue dots connection sites and yellow dots the end of network structures. Data are presented on the bottom panel in a bar graph as mean ± SD, n=3. Statistical significance was analyzed by one-way ANOVA with Dunnett's posttest (***P<0.001).

S3

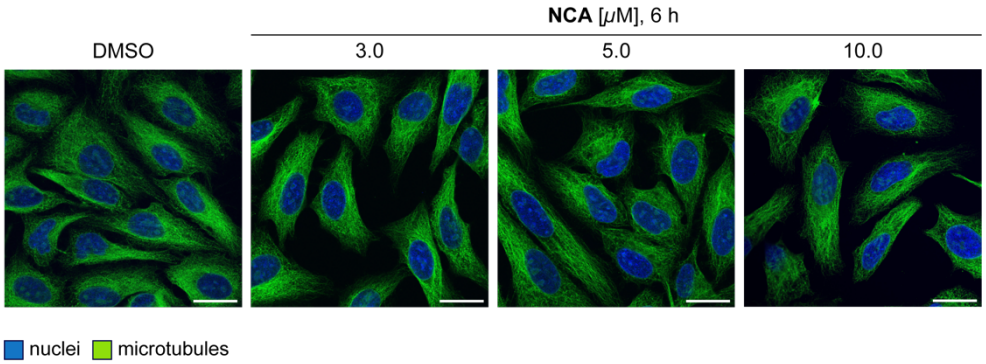

Figure S3 NCA does not affect microtubule network organization in HeLa cells.
Representative images of immunofluorescence staining of HeLa wt cells treated with NCA or DMSO as indicated. Nuclei shown in blue, microtubules in green (scale bar 25 µm), n=2**.**

S4

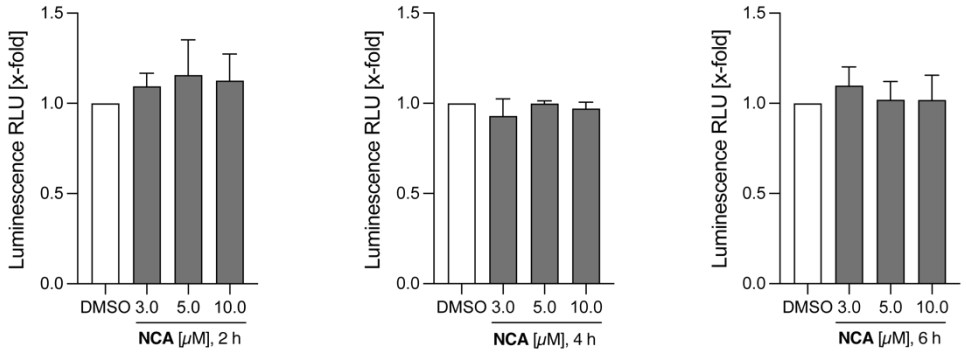

Figure S4 ATP levels in HeLa cells were not altered after NCA treatment.
CellTiter-Glo ATP assay of HeLa cells treated with NCA as indicated for 2, 4 and 6 h. ATP levels were determined by analyzing luminescence intensity. Data are presented in a bar graph as mean ± SD, n=3. Statistical significance was analyzed by one-way ANOVA with Dunnett's posttest.

S5

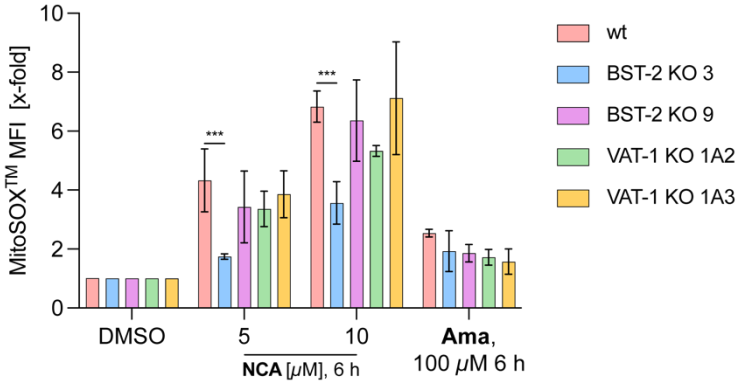

Figure S5 NCA triggers the generation of mitochondrial superoxide in VAT-1 and BST-2 KO cells, too.
Mitochondrial superoxide generation analyzed in HeLa wt, VAT-1 KO 1A2 + 1A3 and BST-2 KO 3 + 9 cells treated with NCA as indicated for 6 h and analyzed by flow cytometry, where antimycin A served as positive control. Data are presented as mean ± SD, n=3. Statistical significance was analyzed by one-way ANOVA with Dunnett's posttest. (***P<0.001).

S6

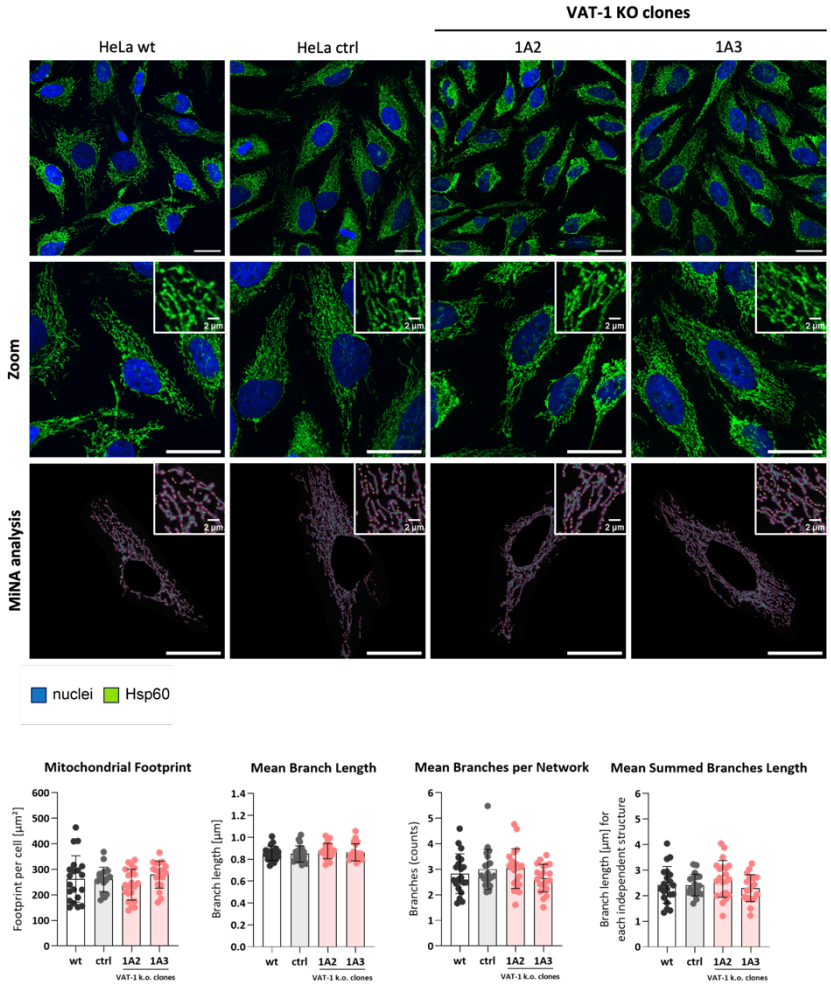

Figure S6 VAT-1 knockout doesn't change mitochondrial network dynamics.
Analysis of mitochondrial dynamics in HeLa wt, CRISPR control and VAT-1 KO 1A2 and 1A3 cells conducted by Elena C.. Representative images of immunofluorescence staining of HeLa wt cells on the top panel, nuclei shown in blue, Hsp60 in green (scale bar 25 μm). Brightness was adjusted to improve visibility. Bottom row shows MiNA analysis, purple area represents mitochondrial footprint, green lines mitochondrial length, blue dots connection sites and yellow dots the end of network structures. Data are presented on the bottom panel in a bar graph as mean ± SD, n=3. Statistical significance was analyzed by one-way ANOVA with Dunnett's posttest (***P<0.001).

S7

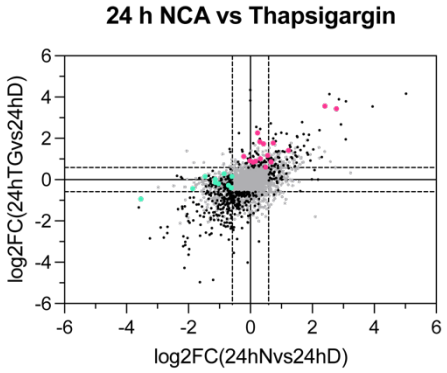

Figure S7 Correlation of whole proteome pathway analysis.
HeLa cells treated with 2.5 μM NCA, 1 μM thapsigargin or DMSO for 24 h. Whole proteome analysis conducted by Josef B. (TU Munich, Germany), IPA pathway analysis performed by Franziska T. (University of Stuttgart). Correlation of whole proteomes shown in a scatter plot. Magenta dots represent proteins from NCA group that are upregulated in the TG group (term ER stress) and green dots represent proteins from the TG group that are downregulated in the NCA group (term OXPHOS). Correlation Pearsons's r =0.7

S8

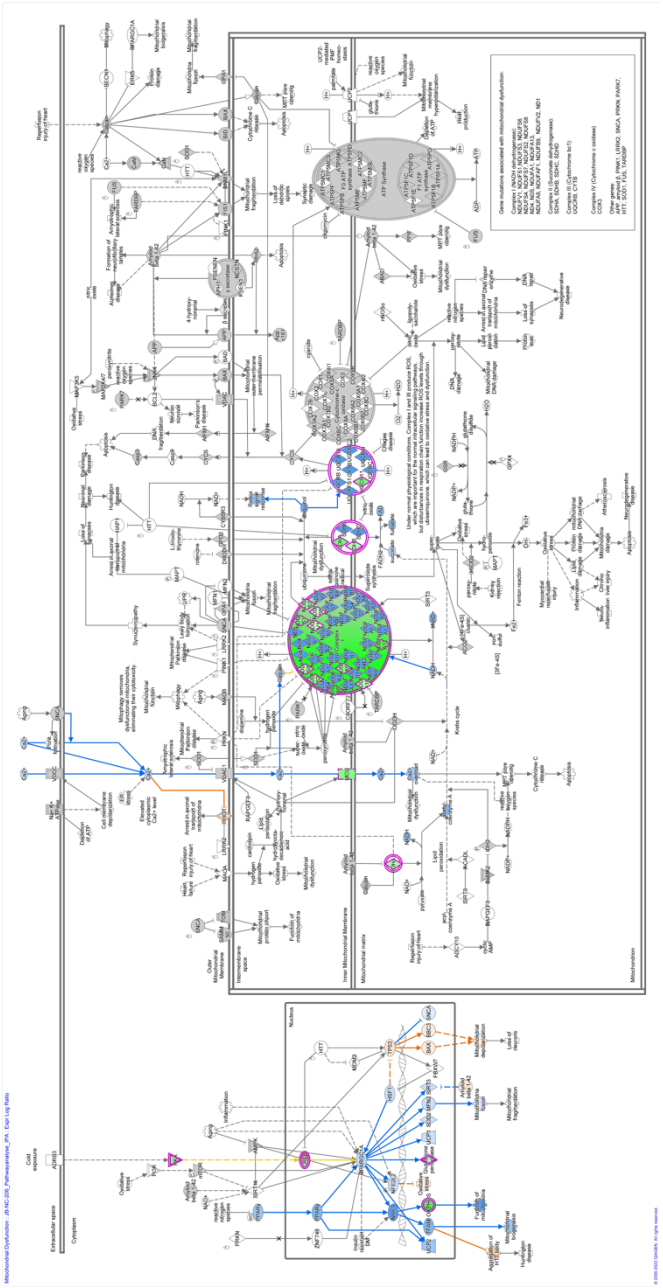

Figure S8 GO term mitochondrial dysfunction (NCA group).
HeLa cells treated with 2.5 μM NCA, 1 μM thapsigargin or DMSO for 24 h. Whole proteome analysis conducted by Josef B. (TU Munich, Germany), IPA pathway analysis performed by Franziska T. (University of Stuttgart). Magenta marked proteins are downregulated, blue marked proteins predicted to be downregulated.

S9

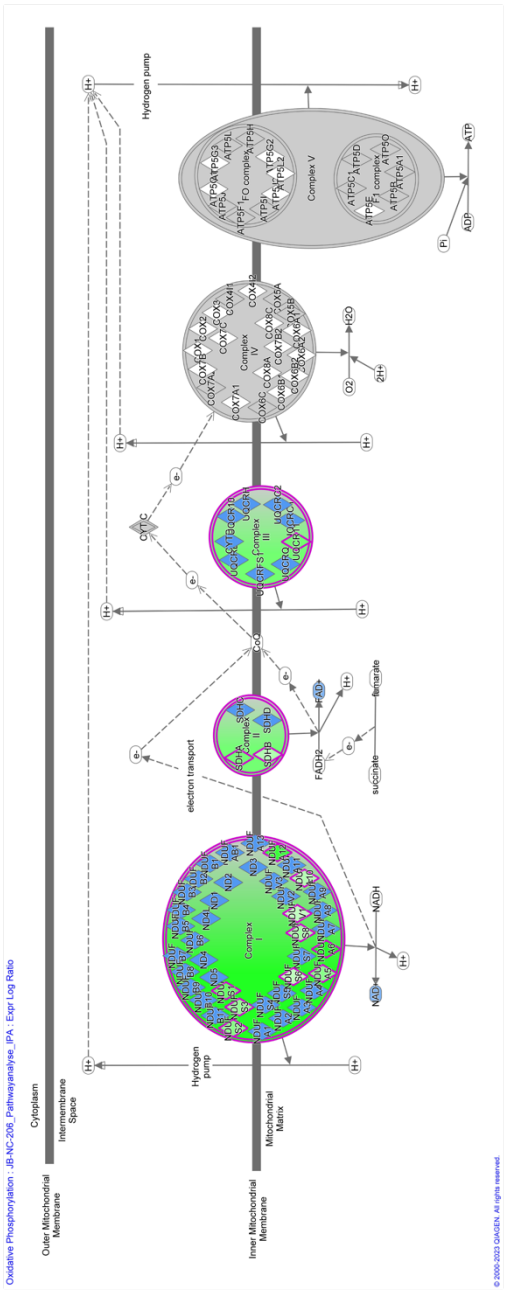

Figure S9 GO term OXPHOS (NCA group).
HeLa cells treated with 2.5 μM NCA, 1 μM thapsigargin or DMSO for 24 h. Whole proteome analysis conducted by Josef B. (TU Munich, Germany), IPA pathway analysis performed by Franziska T. (University of Stuttgart). Magenta marked proteins are downregulated, blue marked proteins predicted to be downregulated.

7.2 Supplementary tables

protein name	gene name	enrichment	p-value	sequence coverage [%]
Heme oxygenase 2	HMOX2	5.45	5.44	46.8
Bone marrow stromal antigen 2	BST2	5.23	3.32	18.3
Vesicle amine transport protein 1 homolog	VAT1	3.93	3.85	48.9
Prostaglandin E synthase	hCG_30600	3.42	1.46	5.6
Reticulon-1	RTN1	3.40	4.47	2.4
GTPase-activating protein and VPS9 domain-containing protein 1	GAPVD1	3.14	1.55	6.6
CD63 antigen	CD63	2.95	1.32	13.5
Cytochrome b5 type B	CYB5B	2.71	4.75	45.2
CD44 antigen	CD44	2.69	1.30	20.9
Amino acid transporter	SLC1A1	2.66	2.95	5.5
cDNA FLJ58568	C16orf58	2.54	3.34	9.5
PRA1 family protein	PRAF2	2.43	1.81	20.8
Coactosin-like protein	COTL1	2.36	1.59	21.9
Endonuclease domain-containing 1 protein	ENDOD1	2.27	2.55	14.2
Pirin (Iron-binding nuclear protein)	PIR	2.15	2.08	15.2
cDNA FLJ46477 fis	MCAM	2.11	1.99	15.1
UPF0729 protein C18orf32	C18orf32	2.02	3.12	13.2
(Reticulon-4	RTN4	1.97	3.59	15.9)

Table S1 ABBP LFQ experiments in HeLa wt cells with 250 nM NC-4 probe (1h) conducted by Josef B. (TU Munich, Germany). Proteins matching criteria (p-value < 0.05, log2 fold-change > 2, except Rtn4 in brackets).

protein name	gene name	enrichment	p-value	sequence coverage [%]
Heme oxygenase 2	HMOX2	-5.62	5.40	46.8

NOC3-like protein	NOC3L	-4.29	2.15	5
Vesicle amine transport protein 1 homolog	VAT1	-3.30	2.71	48.9
Rho GTPase-activating protein 1	ARHGAP1	-3.11	1.56	27.6
Reticulon-1	RTN1	-2.92	3.38	2.4
Niemann-Pick C1 protein	NPC1	-2.89	2.02	5.6
V-type proton ATPase subunit	ATP6V0D1	-2.87	1.48	17.7
cDNA FLJ58568	C16orf58	-2.81	3.34	9.5
GTPase-activating protein and VPS9 domain-containing protein 1	GAPVD1	-2.74	1.58	6.6
Bone marrow stromal antigen 2	BST2	-2.69	3.75	18.3
Prostaglandin E synthase	hCG_30600	-2.66	1.60	5.6
cDNA FLJ77391	EHD4	-2.46	1.42	20.9
Solute carrier family 39 (Zinc transporter)	SLC39A10	-2.35	1.74	6.4
2-Hydroxyacylsphingosine 1-beta-galactosyltransferase	UGT8	-2.32	4.09	9.6
60S ribosomal protein L27	RPL27	-2.27	1.71	15.9
Carboxypeptidase	SCPEP1	-2.25	2.26	4.7
Acyl-CoA (8-3)-desaturase	FADS1	-2.22	1.30	13.5
Transmembrane protein 201	TMEM201	-2.19	2.86	3.8
Phosphoinositide phospholipase C	PLCD3	-2.18	1.70	8.9
Amino acid transporter	SLC1A1	-2.13	2.19	5.5
Isopentenyl-diphosphate Delta-isomerase 1	IDI1	-2.10	1.40	14.1
Prenylcysteine oxidase 1	PCYOX1	-2.10	1.94	20.6
Reticulon-4	RTN4	-2.09	2.14	15.9
Catechol O-methyltransferase	COMT	-2.06	1.55	15.8
Peptidyl-prolyl cis-trans isomerase	PPIL1	-2.05	1.68	29.5
Disco-interacting protein 2	DIP2B	-2.04	2.29	8.8
Carnitine O-palmitoyltransferase	CPT1A	-2.04	1.45	16.4

Table S2 ABBP LFQ competition experiments in HeLa wt cells with 25 μM NCA (1h) and 250 nM NC-4 probe (1h) conducted by Josef B. (TU Munich, Germany). Proteins matching criteria (p-value < 0.05, log2 fold-change <-2).

protein name	gene name	enrichment	p-value	sequence coverage [%]
Heme oxygenase 2	HMOX2	6.56	5.52	46.2
Bone marrow stromal antigen 2	BST2	6.27	5.24	18.3
CD63 antigen	CD63	4.40	3.29	13.5
Reticulon-3	RTN3	3.58	2.15	5.4
CD44 antigen	CD44	3.15	1.62	31.7
Cytochrome b5 type B	CYB5B	2.78	4.77	45.2
Serpin peptidase inhibitor	SERPINE2	2.72	1.33	8.7
cDNA FLJ56823		2.36	2.19	9.4
Tubby-related protein 2	TULP2	2.23	1.60	12.6
Ankyrin repeat and KH domain-containing protein 1	ANKHD1	2.13	1.90	2.2
Dolichol-phosphate mannosyltransferase subunit 1	DPM1	2.10	1.47	8.5
Mitochondrial aldehyde dehydrogenase 2 variant	ALDH2	2.10	3.26	36.8
Reticulon-4	RTN4	2.06	2.49	14.3
MICOS complex subunit	APOOL	2.03	1.69	17.5

Table S3 ABBP LFQ experiments in HeLa VAT-1 KO cells with 250 nM NC-4 probe (1h) conducted by Josef B. (TU Munich, Germany). Proteins matching criteria (p-value < 0.05, log2 fold-change > 2).

7.3 Abbreviations

Abbreviation	Term
ΔΨm	Mitochondrial membrane potential
2-DG	2-deoxy-D-glucose
ABPP	Activity-based protein profiling
ADP	Adenoside 5'-diphosphate
AM	Acetoxymethyl ester
ANOVA	Analysis of variance between groups
APS	Ammonium persulfate
Apaf1	Apoptotic peptidase activating factor 1
ATF4	Activating transcription factor 4
ATF6	Activating transcription factor 6
ATP	Adenoside 5'-triphosphate

Abbreviation	Term
Bak	Bcl-2 homologous antagonist killer
Bax	Bcl-2-associated X protein
Bcl-2	B-cell lymphoma 2
BH-3 only	B-cell lymphoma 2 (Bcl-2) homology 3
BiP	Binding immunoglobulin protein
BSA	Bovine serum albumin
CCCP	Carbonylcyanid-m-chlorphenylhydrazon
cDNA	Complementary DNA
CHOP	C/EBP homologous protein
CO_2	Carbon dioxide
Co. KG	Compagnie Kommanditgesellschaft
CRISPR	Clustered regularly interspaced short palindromic repeats
Da	Dalton
DCIP	2,6-dichlorophenolindophenol
DDIT3	DNA damage induced transcript 3
DMEM	Dulbecco's Modified Eagle Medium
DMSO	Dimethyl sulfoxide
DMSZ	Deutsche Sammlung von Mikroorganismen und Zellkulturen
DNA	Deoxyribonucleic acid
DR5	Death receptor 5
Drp1	Dynamin 1 like
DTT	1,4-dithiothreitol
ECL	Enhanced chemiluminescence
ECM	Extra cellular matrix
EDTA	Ethylenediaminetetraacetic acid
eIF2α	Eukaryotic translation initiation factor 2α
e.g.	Example given
ER	Endoplasmic reticulum
ERAD	ER-associated protein degradation
ETC	Electron transfer chain
FA	Focal adhesion
FACS	Fluorescence activated cell sorting
FCS	Fetal calf serum
FDA	Federal drug agency
FITC	Fluorescein isothiocyanate
FSC	Forwards scatter
FW	Forward
GAPDH	Glyceraldehyde 3-phosphate dehydrogenase
GmbH	Gesellschaft mit beschränkter Haftung
HCC	Hepatocellular carcinoma

Abbreviation	Term
HFS	Hypotonic fluorochrome solution
HHBS	Hanks' buffer with HEPES
H+L	Heavy and light (chain)
HRP	Horseradish peroxide
Hsp60	Heat shock protein 60
IC_{50}	Half maximal inhibitory concentration
ICC/IF	Immunocytochemistry/immunofluorescence
IRE1	Inositol requiring 1
IgG	Immunoglobulin G
JC-1	Tetraethylbenzimidazolylcarbocyanine iodide
Kank2	KN motif and ankyrin repeat domains 2
KD	Knockdown
KGaA	Kommanditgesellschaft auf Aktien
KO	Knockout
LC3	Microtubule-associated protein 1A/1B-light chain 3
LC-MS/MS	Liquid chromatography-mass spectrometry/mass spectrometry
LINGO-1	Like leucine rich repeat and Ig domain containing 1
log	Logarithm to base ten
MFI	Mean fluorescence intensity
Mfn1	Mitofusin 1
MiNA	Mitochondrial network analysis
MOMP	Mitochondrial outer membrane permeabilization
MPTP	Mitochondrial permeability transition pore
mRNA	Messenger RNA
n.a.	Not available
NADH	Nicotinamide adenine dinucleotide hydrogen
NADPH	Nicotinamide adenine dinucleotide phosphate hydrogen
NCA	Neocarzilin A
NCB	Neocarzilin B
NCC	Neocarzilin C
NP-40	Octoxinol 9
ns	Not significant
NT	Non-targeting
OCR	Oxygen Consumption Rate
Opa1	Optic atrophy protein 1
OXPHOS	Oxidative phosphorylation
PAGE	polyacrylamide gel electrophoresis
PBS	Phosphate-buffered saline
PE	Phycoerythrin
PGC1α	Peroxisome proliferator-activated receptor-γ co-activator

Abbreviation	Term
PI	Propidium iodide
PI3K	Phosphoinositid-3-kinase
PMT	Photomultiplier
P	Phosphate
PCR	Polymerase chain reaction
PARP	Poly (ADP-ribose) polymerase
PERK	PKR-like ER kinase
PFA	Paraformaldehyde
PMSF	Phenylmethylsulfonyl fluoride
PVDF	Polyvinylidene difluoride
qPCR	Quantitative real-time PCR
RHD	Reticulon homology domain
ROS	Reactive oxygen species
RNA	Ribonucleic acid
RV	Reverse
SAR	Structure-activity relationships
SDS	Sodium dodecyl sulfate
SD	Standard deviation
siRNA	Small interfering RNA
SSC	Sideward scatter
STR	Short tandem repeat
SUIT	Substrates uncouplers inhibitors titration
TEM	Transmission electron microscopy
TBS-T	Tris-buffered saline + Tween20
TCA	Tricarboxylic acid
TCE	Trichloroethanol
T/E	Trypsin/ethylenediaminetetraacetic acid
TEMED	Tetramethylethylenediamine
TG	Thapsigargin
TLN1	Talin1
Tris	Tris(hydroxymethyl)aminomethane
UPR	Unfolded protein response
USA	United States of America
VAT-1	Vesicle membrane protein 1

Table S4: List of abbreviations

7.4 Symbols and units

Symbol/Unit	Term
%	Percent
% (m/m)	Mass percent
% (v/m)	Volume percent
°C	Degree Celsius
μg	Microgram [10^{-6} g]
μL	Microliter [10^{-6} L]
μm	Micrometer [10^{-6} m]
μM	Micromolar [10^{-6} M]
cm^2	Square centimeter
g	Gravity
h	Hour(s)
kDa	Kilodalton
M	Molar concentration
min	Minute(s)
mL	Milliliter [10^{-3} L]
mm	Millimeter [10^{-3} m]
mM	Millimolar [10^{-3} M]
nm	Nanometer [10^{-9} m]
nM	Nanomolar [10^{-9} M]
nmol	Nanomoles
pmol	Picomoles
V	Volt
®	Registered Trademark
™	Trademark
α	Alpha

Table S5: Symbols and units

List of Figures

List of Tables

7.5 List of publications and conference contributions

7.5.1 Research articles

Neocarzillin inhibits cancer cell proliferation via BST-2 degradation resulting in lipid raft trapped EGFR

Josef Braun[†,#], Yudong Hu[‡,#], Adrian T. Jauch[‡#], Thomas F. Gronauer[†], Julia Mergner[°], Nina Bach[†], Franziska Traube[Ⱡ], Stefan Zahler*[,‡], Stephan A. Sieber*[,†]

under submission

[#] authors contributed equally to this manuscript

7.5.2 Conference contributions

Effects of the natural compound neocarzilin A on mitochondrial dynamics and functions

Oral Presentation: Adrian T. Jauch, Judith Sailer, Elena Czeslik, Judith Nagel, Carola Eberhagen, Hans Zischka, Angelika M. Vollmar, Stefan Zahler

19th World Congress of Basic & Clinical Pharmacology 2023
July 2023, Glasgow, Scotland

7.6 Acknowledgements

Mein erster und größter Dank geht an meine Doktormutter, Frau Prof. Vollmar. Vielen Dank, dass Sie mir die Möglichkeit gegeben haben in Ihrem Arbeitskreis zu promovieren und dabei drei interessante Projekte zu bearbeiten. Vielen Dank für Ihre Betreuung und die vielen wertvollen Ratschläge und Diskussionen. Ihre positive Art, Ihr Optimismus und Talent aus jedem ihrer Doktoranden das beste zu holen, sowie Ihre Begeisterung für die Wissenschaft und Ihre herzliche Art, machen Sie zu einem großen Vorbild für mich. Ich kann mich sehr glücklich schätzen sowohl in den Genuss gekommen zu sein Ihre Vorlesung besuchen als auch meine Promotionen bei Ihnen machen zu dürfen.

Ein besonderer Dank gilt meinen weiteren Prüfern. Vielen Dank, Herr Prof. Zahler, dass Sie meine Arbeit als zweiter Gutachter beurteilt haben. Ich danke außerdem Herrn Prof. Wagner, Herrn Prof. Fürst, Frau Prof. Merkel und Frau Univ.-Prof. Simone Moser. Herzlichen Dank, dass Sie sich Zeit genommen haben meine Arbeit zu bewerten.

Ganz herzlich möchte ich mich auch für die Betreuung der ersten Jahre meiner Promotion bei Simone bedanken. Vielen Dank, dass du das Vertrauen in mich gesetzt hast und in dein Team aufgenommen hast! Ich konnte jederzeit zu dir kommen und über unser Projekt sprechen, deine Tür stand immer für mich offen, das habe ich unglaublich geschätzt! Und so war es auch ein schwerer Einschnitt, als du uns in Richtung Industrie verlassen hast.

Und damit komme ich zu Ihnen Herr Zahler. Ich bin Ihnen sehr dankbar, dass die mich damals nach Simones Abgang in Ihrem Team aufgenommen haben. Zu keinen Zeitpunkt haben Sie einem das Gefühl gegeben, dass das für Sie eine Belastung wäre und Sie haben sich genau so wie bei Ihren eigenen Projekten reingekniet, haben immer wieder tolle Ideen eingebracht und Kontakte zu anderen Gruppen hergestellt, aus denen tolle Kooperationen etnstanden sind.

Bei diesen Kooperationspartnern möchte ich mich auch ganz herzlich bedanken. Da wären zum einen Carolin Gleissner, Josef Braun und Herr Prof. Sieber mit denen ich unser spannendes Neocarzilin/VAT-1 Projekt bearbeitet habe. Lieber Josef, es waren immer sehr nette Meetings und Treffen in Person mit dir (und meisten hast du ja den Weg zu uns auf dich genommen) und es freut mich sehr, dass wir unsere gemeinsamen Paper bald fertistellen werden. Zudem möchte ich mich bei Judith Sailer, Carola Eberhagen und Herrn Prof. Zischka für die tolle Zeit, die ich in eurem Labor im Rahmen des Neocarzilin/Mitochondrien-Projekts verbringen durfte und die zahlreichen Zoom Meetings und Inspirationen für das spannende Projekt bedanken.

Liebe Judith, du hast dir immer so viel Zeit für mich und unser Projekt genommen, dafür bin ich dir sehr dankbar! Es hat mit wahnsinnig Spaß gemacht mit dir zusammen zu arbeiten und ihr habt viele, wertvolle Ergebnisse zu dieser Arbeit beigetragen. Ein großer Dank geht natürlich an den gesamten AK Vollmar. Ich hätte mir keine besseren Kollegen wünschen können und ich bin jeden Tag gerne in die Arbeit gekommen. Die Zeit mit euch war einfach großartig. Ein ganz besonderer Dank geht dabei an Patricia und vor allem Conny, Maibritt und Flo. Vielen Dank, dass ihr immer für mich da wart und mich sowohl fachlich unterstützt habt als auch für die Freunschaft, die sich außerhalb des Labors aufgebaut hat. Die gemeinsamen Mittags- und Kaffee Pausen werden mir immer in Erinnerung bleiben. Danke auch an meine ehemalige Kollegin und Platznachbarin Chrissi, du hast mir in der Anfangszeit sehr geholfen und ich habe mich immer sehr gefreut morgens ins Labor zu kommen und dich dort zu treffen. Bei Rita und Jana möchte ich mich außerdem für die großartige und geduldige Einarbeitung am Anfang und Unterstützung zu jeglicher Zeit der Promotion bedank. Vielen Dank auch an Julia, Frau Schnegg, Bernadette und Elke für die Unterstützung bei meinen Projekten. Ein großer Dank geht an meine Bachelor- und Masterstudentin Elena Czeslik, die das großartige Mitochondrien Projekt mit ins Leben gerufen hat. Ich habe wirklich immer gerne mit dir zusammengearbeitet und du hast echt sehr gute Arbeit geleistet. Es hat mich wahnsinnig beeindruckt deinen Werdegang und deine Entwicklung von der Bachelorarbeit über das Masterforschungspraktikum hin zu der sehr gelungen Masterarbeit zu beobachten und ich freue mich ein Teil davon gewesen zu sein. Dann möchte ich mich auch ganz besonders bei Julia Geyer bedanken, mit der ich das spannende Mitochondrien Pojekt weiterverfolgt hab. Ich hatte wirklich eine sehr nette Zeit mit dir und neben der tollen Arbeit, die du geleistet hast, war es auch immer sehr lustig mit dir im Labor. Und auch bei Mariem und Laura, die ich bei ihrem Master-Forschungspraktikum betreut habe möchte ich mich bedanken. Es hat mir großen Spaß gemacht mit euch zusammenzuarbeiten und ich denke ich habe durch die Betreuung einiges gelernt und wir haben interessante Daten generiert.

Vielen Dank auch an die LMU Shakers, es hat immer sehr viel Spaß gemacht Donnerstags Körber mit euch zu werfen, das war teilweise ganz großer Sport. Und auch die Frisbee Sessions auf der Mückenwiese bleiben unvergesslich!

Zu guter Letzt möchte ich mich noch bei meinen Freunden und meiner Familie bedanken.

Ein großes Dankeschön möchte ich an Stefan richten. Wir haben uns gemeinsam durch das Pharmaziestudium gekämpft und es war, vor allem dank dir, eine unvergessliche Zeit für mich. Wir hatten immer unseren Spaß zusammen, haben aber auch immer ähnlich schwer unter dem permanent ansteigenden Stresspegel gelitten. Ohne dich hätte ich das Studium niemals so erfolgreich abschließen können, dafür bin ich dir sehr dankbar!

Mein wichtigster Dank gilt schließlich meiner Familie. Zunächst meinen Eltern, Gabi und Achim. Vielen Dank für eure grenzenlose Unterstützung während meines gesamten Lebensweges und dass ihr es mir ermöglicht habt diesen so unbeschwert zu gehen. Danke, dass ihr immer hinter mir steht und an mich glaubt. Vielen Dank auch meinen Schwiegereltern, Heike und Bernhard, die immer wieder versucht haben zu verstehen, was ich eigentlich so bei meiner Arbeit mache. Ich hoffe ich finde jetzt mal Zeit und Muße es euch ein bisschen ausführlicher zu erklären. Danke auch an meine Brüder Sascha und Raphael, dass ihr immer für mich da wart. Der größte Dank gilt meiner wunderbaren Frau. Liebe Vivi, ich bin dir unglaublich dankbar für deine unendliche Geduld und für deine großartige Fähigkeit mich immer wieder aufzubauen und den Fokus auf das wichtige im Leben zu richten. Du musstest einiges ertragen in den letzten vier Jahren, warst meistens die erste Person, die meinen Frust abfedern musste. Du hast aber nie aufgehört an mich zu glauben und mich in jeglicher Situation zu unterstützt, ich bin so froh dich in meinem Leben zu haben. Euch allen gilt diese Arbeit!